論文 / 著書情報
Article / Book Information

題目(和文)	強相関局在系としてのTTF系有機電荷移動塩の電気的および磁気的性質
Title(English)	Electrical and magnetic properties of TTF-based organic charge transfer salts in strongly correlated systems
著者(和文)	米山直樹
Author(English)	
出典(和文)	学位:博士(理学), 学位授与機関:東京工業大学, 報告番号:甲第3977号, 授与年月日:1999年3月26日, 学位の種別:課程博士, 審査員:
Citation(English)	Degree:Doctor (Science), Conferring organization: Tokyo Institute of Technology, Report number:甲第3977号, Conferred date:1999/3/26, Degree Type:Course doctor, Examiner:
学位種別(和文)	博士論文
Type(English)	Doctoral Thesis

Thesis

Electrical and magnetic properties of TTF-based organic charge transfer salts in strongly correlated systems

A thesis submitted
to
Tokyo Institute of Technology
for
the Degree of Doctor of Science
(Hakushi(Rigaku))

by
Naoki Yoneyama

Department of Chemistry, Faculty of Science
Tokyo Institute of Technology
March, 1999

Acknowledgements

The present work has been carried out in Enoki's laboratory in Tokyo Institute of Technology. The author wishes to thank Professor Toshiaki Enoki for his considerable guidance, fruitful discussion, and a critical reading of the manuscript. The author were fortunate to have had the assistance of Professor Toshiaki Enoki and Professor Kazuya Suzuki (Yokohama National University) for suggesting this theme and for stimulating interest in it.

The author is sincerely grateful to Professor Gunzi Saito (Kyoto University) for a gift of the BEDT-TTF donor. The author is indebted to Professor Masahiko Iyoda (Tokyo Metropolitan University) for providing the organic donor EDO-TTFBr_2 and several helpful discussion. The author would like to express his thanks to Professor Takehiko Mori (Tokyo Institute of Technology) for a gift of several single crystal samples. The author is grateful to acknowledge the excellent suggestion of Professor Hiroyuki Shiba (Tokyo Institute of Technology) on the transport phenomena. The author whishes to thank Professor Kyuya Yakushi (Institute for Molecular Science) for the fruitful advice on the measurement of the thermoelectric power. The author wishes to thank Professor Yoshitami Ajiro (Kyushu University) for suggesting the low-dimensional magnetism in the ESR measurements. The author is also deeply indebted to Dr. Hidehiro Uegusa (Tokyo institute of Technology) for his considerable assistance with the X-ray diffraction measurement.

The author would like to express his appreciation to Dr. Hirohiko Satō (Professor Enoki's group) for his fruitful discussion and guidance on the measurements. The author is also grateful to Dr. Akira Miyazaki (Professor Enoki's group) for his appropriate suggestion and helpful discussion on the syntheses and the characterization of the samples. Thanks are due to all the member of Professor Enoki's group for their considerable advice and encouragement.

Finally I would like to thank to my parents for their continuous encouragement in proceeding the study and their financial support.

Publication Lists

[1] T. Enoki, Ma. Enomoto, Mi. Enomoto, K. Yamaguchi, N. Yoneyama, J. Yamaura, A. Miyazaki, and G. Saito, "MOLECULAR MAGNETS BASED ON CHARGE TRANSFER COMPLEXES", *Mol. Cryst. Liq. Cryst.*, **285** (1996) 19-26.

[2] M. B. Zaman, Y. Morita, J. Toyoda, H. Yamochi, G. Saito, N. Yoneyama, T. Enoki, and K. Nakasuji, "Charge-Transfer Complex of a New Acceptor Cyananilate with Tetramethyltetrathiafulvalene, $(TMTTF)_2HCNAL$", *Chem. Lett.*, (1997) 729-730.

[3] N. Yoneyama, A. Miyazaki, T. Enoki, and G. Saito, "Magnetic Properties of $(BEDT\text{-}TTF)_2X$ with Localized Spins" *Synth. Met.*, **84** (1997) 2029-2030.

[4] N. Yoneyama, A. Miyazaki, and T. Enoki, "Physical Properties of $(BMDT\text{-}TTF)_3AsF_6$(1,1,2-trichloroethane)", *Synth. Met.*, (1999), in press.

[5] N. Yoneyama, A. Miyazaki, T. Enoki, and G. Saito, "Magnetic Properties of TTF-Type Charge Transfer Salts in the Mott insulator Regime", *Bull. Chem. Soc. Jpn.*, **72** (1999), in press.

Contents

Chapter 1

Introduction

Charge transfer salts show various electronic properties from metal to insulator, where the importance of a Coulomb interaction between the conduction electrons has been pointed out since the early stages of this field. In strongly correlated systems the Coulomb interaction leads to a large number of interesting physical phenomena, for example ferromagnetism of transition metals, heavy fermion, and high-T_{C} superconductor. The extremely large Coulomb interaction in a half-filled band structure compels the electrons to be localized, that is to say the Mott insulator.

We are interested in the electronic states of the charge transfer salts in the strongly correlated system, and thus try to approach this regime from the view of the Mott insulator as an extreme state. To clarify the aim of this work, first we explain the Mott insulator in § 1.1. Second, we guide the outline of magnetism (§ 1.2) and the effect of the low-dimesionality (§ 1.3). Third, the characteristic features of the charge transfer salts are discussed with several topics in § 1.6. Finally, we explain the aim of this work in § 1.7, and afterward the crystal structures of our target salts are introduced.

1.1 Mott insulator

1.1.1 Transfer integrals and Coulomb interactions

Let us arrange the hydrogen atoms one-dimensionally with an electron per atom as shown in Fig. 1.1(a), which corresponds to a half-filled state. We treat this one-dimensional sequence of hydrogen atoms as a model to consider the Mott insulator. A sufficiently small distance between atoms which gives large overlap between the atomic orbitals, will enable the jump of an electron on a site to the adjacent site easily, producing an electron current in the metallic state, where this one electron transfer causes the energy destabilization associated with the on-site Coulomb interaction U (Fig. 1.1(b)). In the metallic state, the Coulomb interaction between electrons running fast on the line of the atoms is well described by the mean-field theory such as the Hartree approximation. When the atoms are gradually separated, where the overlap between atomic orbitals gets small, the electrons tend to localize on each atom.

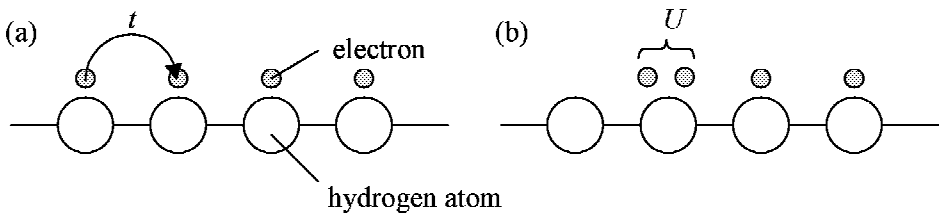

Figure 1.1: Transfer integral t and on-site Coulomb energy U. The large circles are hydrogen atoms arranged one-dimensionally with an electron (small circle) per atom, where the electronic state is characterized by the competition between stabilization by t and destabilization by U.

As a result, the reduction of the transfer integrals brings about the localization of electrons on each atomic site, and finally the electron current with metallic behavior hardly flows becoming an insulating state called the Mott insulator, where the tight-binding approximation will be suitable for the description of the system. The feature of the Mott insulator is therefore the existence of intrinsic magnetic moments localized at atomic sites since the electron has an S=1/2 spin (see in § 1.2.1).

1.1.2 Hubbard model

As mentioned in § 1.1.1, the tight-binding approximation describes the motion of electrons strongly restricted in the atomic orbital, where the on-site Coulomb repulsion acts between two electrons when they are located on the same site simultaneously. For the description of this electronic state, the simplest model is the following Hubbard Hamiltonian:

$$\hat{H} = \sum_{i\sigma} E_0 c_{i\sigma}^{\dagger} c_{i\sigma} + \sum_{i \neq j,\sigma} t_{ij} c_{i\sigma}^{\dagger} c_{j\sigma} + \frac{1}{2} \sum_{i\sigma} U c_{i\sigma}^{\dagger} c_{i\sigma} c_{i-\sigma}^{\dagger} c_{i-\sigma}, \tag{1.1}$$

where i is the lattice site, σ is the spin quantum number, $c^{\dagger}$ and c are the creation/annihilation operators, and t_{ij} is the transfer integral from the j- to i-site, respectively. One electron in the i-site has the energy of E_0, and the coexistence of two electrons in the same site gives the increase of the energy by U. Here, we consider a half-filled state with $t_{ij}(=t)$ much smaller than U working between the nearest neighbor sites (Mott insulator state), where the half-filled state is defined as the same number of electrons with atoms exist. The reduction of the energy based on the second perturbation approximation gives rise to an antiparallel spin arrangement between adjacent spins because of the Pauli principle, which is estimated at,

$$\Delta E_{ij} = -2t^2/U. \tag{1.2}$$

Using the spin on the i-site, $\boldsymbol{S}_i$, we can express Eq. (1.1) in the following form:

$$\hat{H} = -\sum_{\langle i,j \rangle} 2J_{ij} \left[\boldsymbol{S}_i \cdot \boldsymbol{S}_j - \frac{1}{4} \right], \tag{1.3}$$

$$J_{ij} = -|t_{ij}|^2/U. \tag{1.4}$$

Thus, Eqs. (1.3) and (1.4) indicate the correspondence between the Hubbard Hamiltonian under the condition $U \gg t$ and the S=1/2 Heisenberg antiferromagnetic Hamiltonian for a localized spin system.

1.1.3 Effective on-site Coulomb interaction for dimer/trimer systems

We consider two adjacent radical anions with an electron per molecule [1]. When the overlap between the wave functions of molecules is small, the ground state gives unpaired electrons localized on each molecule, and the lowest excited state is a charge transfer state from a molecule to the other molecule. The energy of the excited state must be larger than the ground state by an energy of the on-site Coulomb interaction, U_0. The on-site Coulomb energy is considered to be intrinsic for the molecules, which is known to range about 1–2 eV as depicted in Fig. 1.2.

Next, in the same way, we treat the effective on-site Coulomb interaction for dimerized molecules having an electron per dimer, assuming that the intra-dimer transfer integral t_{intra} is sufficiently larger than the inter-dimer transfer integral t_{inter}. In the ground state, the electrons are localized on each dimer, which can be excited with one electron transfer to the another dimer. For the calculation of the energies of excited states, we use the Hubbard Hamiltonian described as,

$$\hat{H} = t_{\mathrm{intra}} \sum_{\sigma} (c_{1\sigma}^{+} c_{2\sigma} + c_{2\sigma}^{+} c_{1\sigma}) + U_0 \sum_{i=1,2} n_{i\uparrow} n_{i\downarrow}. \tag{1.5}$$

Using four basis of $|\uparrow\downarrow, 0\rangle$, $|\uparrow, \downarrow\rangle$, $|\downarrow, \uparrow\rangle$, and $|\, 0, \uparrow\downarrow\rangle$, Eq. (1.5) gives the lowest excited state with a singlet coupling of two electrons on a dimer. The energy gap between the ground state and the lowest excited state, U_{eff}, is obtained as

$$U_{\mathrm{eff}} = 2|t_{\mathrm{intra}}| + \left[U_0 - \sqrt{U_0^2 + 16 t_{\mathrm{intra}}^2} \right] /2. \tag{1.6}$$

When $U_0 \gg t_{\mathrm{intra}}$, Eq. (1.6) is approximated as

$$U_{\mathrm{eff}} \approx 2|t_{\mathrm{intra}}|. \tag{1.7}$$

The similar calculation for a trimer unit [2] can be carried out, which gives

$$U_{\mathrm{eff}} \approx \sqrt{2}|t_{\mathrm{intra}}|. \tag{1.8}$$

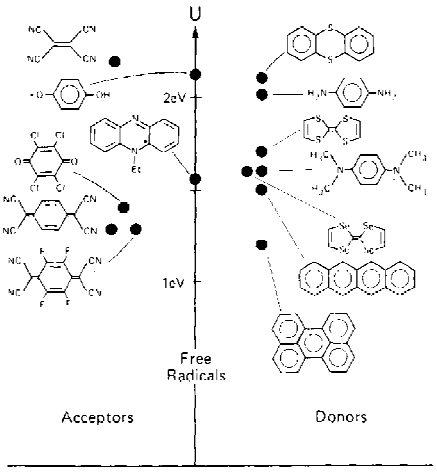

Figure 1.2: On-site Coulomb interactions for several molecules [1].

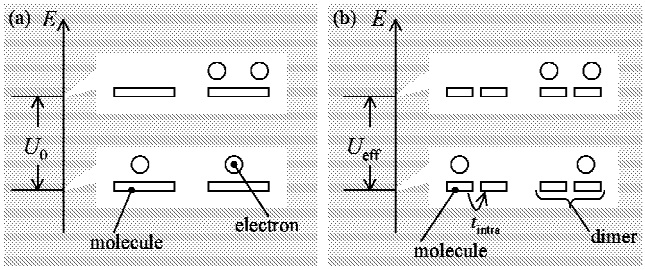

Figure 1.3: Schematic energy level configuration associated with the Hubbard model. (a) The definition of U_0 for a molecule. In the ground state, each electron (circle) is located on each molecule (rectangle). (b) The definition of U_{eff} for a dimer.

1.2 Magnetism

The magnetic moment of an atom originates from the electron giving a paramagnetic contribution and the change in the orbital moment induced by an applied magnetic field giving a diamagnetic contribution. Generally, the magnetic susceptibility of a substance is defined as

$$\chi = \frac{M}{B}, \tag{1.9}$$

where M is the magnetization of the net magnetic moment per mole of the substance and B is the applied magnetic flux density. Substances with a negative magnetic susceptibility are called diamagnetic, and those with a positive magnetic susceptibility are called paramagnetic.

1.2.1 Electron spin

The angular momentum for an electron in the quantum theory is associated with the rotational degree of freedom of an electron as a classical sphere, that is the spin angular momentum of $(1/2)\hbar$ for an electron. The spin angular moment is understood electromagnetically in terms of an induced magnetic moment by a ring current based on the rotation of the electron charge. Taking into account the Dirac's theory, the relationship between the spin angular moment ($\boldsymbol{s}$) and the spin magnetic moment ($\boldsymbol{\mu}_{\mathrm{spin}}$) is described as

$$\boldsymbol{\mu}_{\mathrm{spin}} = -g_{\mathrm{spin}}\mu_{\mathrm{B}}\boldsymbol{s}, \tag{1.10}$$

where g_{spin} is the g-factor and μ_{B} is the magnetic moment of the electron, that is Bohr magneton:

$$\mu_{\mathrm{B}} = eh/2m_e c = 9.27 \times 10^{-21}\mathrm{emu}. \tag{1.11}$$

1.2.2 Diamagnetism of an atom with a closed shell

To specify the state of electrons in an atom, four quantum numbers of n, l, m_l, and m_s are required. The electron configuration in the atom (or ion) with a filled electron shell structure is settled on the basis of the Pauli principle and the Hund's rule as a ground state having L=S=0, which is the total orbital/spin angular momentum where L=$\sum l_j$ and S=$\sum s_j$ (l_j and s_j are an orbital/spin angular momentum of an electron). Therefore, the summation of the whole orbital and spin magnetic moments becomes zero, causing no intrinsic magnetic moment in the closed shell structure. This electronic state with the disappearing magnetic moment is the diamagnetism.

When an external field is applied to an atom (ion) with the closed shell structure, the motion of the electron within the shell is classically explained by the Lenz's rule where an induced current flows to vanish the change of the field, and thus the magnetic moment is

induced toward the opposite direction to the external field. The diamagnetic moment induced by the field $\boldsymbol{H}$ is described as

$$\Delta\boldsymbol{\mu}_{\mathrm{dia}} = -\frac{e^2}{6m_e}\langle r^2\rangle \boldsymbol{H}, \tag{1.12}$$

where $\sqrt{\langle r^2\rangle}$ is the average radius of the distribution for the atom (~ 1 Å). The diamagnetism depends on the electron configuration within the closed shell where the excitation energy of about 10^5 K is needed to change the configuration, and thus the diamagnetic susceptibility does not show any temperature dependence in the temperature range around room temperature. Ordinary organic compounds, whose molecular orbitals have closed shell structures, therefore indicate the temperature-independent diamagnetic properties. The susceptibility of these organic compounds, χ, can be approximately estimated by the summation of the diamagnetic contributions from the atoms composing the molecule (Pascal's additive rule):

$$\chi = \sum \chi_{\mathrm{a}} + \lambda, \tag{1.13}$$

where χ_{a} is the core diamagnetic susceptibility and λ is the correction term dependent on the specific molecular structure such as carbon-carbon double bond. This rule is experimentally well justified, whereas it does not always stand up, for example, in π-conjugated compounds because of the difficulty to estimate the correction terms which come from the π-electrons.

1.2.3 Exchange interaction and magnetic dipole-dipole interaction

Two important interactions, an exchange interaction and a magnetic dipole-dipole interaction, feature a magnetic systems consisting of large number of spins. The exchange interaction energy is described by the quantum mechanics,

$$U_{\mathrm{E}} = -2J_{ij}\boldsymbol{S}_i \cdot \boldsymbol{S}_j, \tag{1.14}$$

where $\boldsymbol{S}_i$ and $\boldsymbol{S}_j$ are the spins in the i- and j-sites, respectively, and J_{ij} is the exchange interaction between $\boldsymbol{S}_i$ and $\boldsymbol{S}_j$. The positive and negative values of the exchange interaction make the the parallel and antiparallel spin configuration stable, respectively.

The magnetic dipole-dipole energy is well understood on the basis of two bar-magnets in the classical mechanics as shown in Fig. 1.4, that is,

$$U_d = \frac{\boldsymbol{\mu}_1 \cdot \boldsymbol{\mu}_2}{r^3} - \frac{3(\boldsymbol{\mu}_1 \cdot \boldsymbol{r})(\boldsymbol{\mu}_2 \cdot \boldsymbol{r})}{r^5}, \tag{1.15}$$

where the two dipole moments $\boldsymbol{\mu}_1$ and $\boldsymbol{\mu}_2$ are separated in the distance of r.

The weakness of the dipole-dipole interaction corresponding with the order of the thermal energy of about 1K at most, which is estimated for the system consisting of 1 μ_{B} dipoles located in a distance of a few Å, does not explain the strong interactions of permanent magnets. The exchange interaction works in short-range and has a hundred to thousand times larger strength than that of the dipole-dipole interaction.

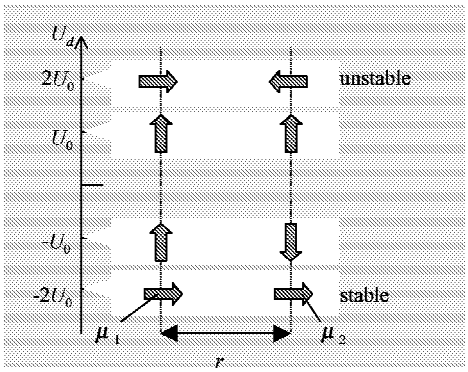

Figure 1.4: Schematic view of the magnetic dipole-dipole interactions. The bold arrows are the magnetic moments.

1.2.4 Molecular-field theory of paramagnetism

Let us first consider the most basic Heisenberg spin system, having no interaction between spins in an applied field along the z-axis, which is described with a Hamiltonian consisting of only the Zeeman energy,

$$\hat{H} = -\sum_i g\mu_{\mathrm{B}} \boldsymbol{S}_i \cdot \boldsymbol{H} \tag{1.16}$$

$$= -g\mu_{\mathrm{B}} H_z \sum_i S_i^z. \tag{1.17}$$

This Hamiltonian gives the Curie law through a statistic treatment based on the Boltzmann distribution of the spins, which describes the paramagnetic susceptibility:

$$\chi = \frac{C}{T}, \tag{1.18}$$

where C is the Curie constant,

$$C = \frac{Ng^2\mu_{\mathrm{B}}^2 S(S+1)}{3k_{\mathrm{B}}}, \tag{1.19}$$

in which, C=0.375 emu/mol K for an S=1/2 system. The effective Bohr magneton p is defined as

$$p = g\sqrt{S(S+1)}, \tag{1.20}$$

indicating that a spin S has a magnetic moment of p μ_{B}. The Curie law well explains the spin system having negligibly small exchange interaction or in the high temperature region.

Next, we consider the exchange interaction in addition to the Zeeman term,

$$\hat{H} = -\sum_{\langle ij \rangle} J_{ij} \boldsymbol{S}_i \cdot \boldsymbol{S}_j - \sum_i g\mu_{\mathrm{B}} S_i^z H_z. \tag{1.21}$$

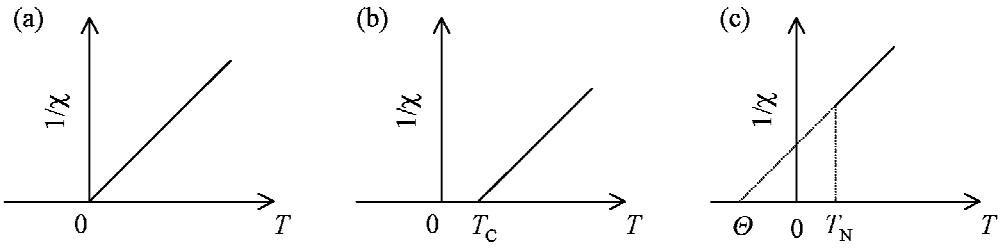

Figure 1.5: Schematic view of the Curie-Weiss law. (a) Θ=0. (b) Θ>0, with a ferromagnetic transition at $T_{\rm C}$=Θ. (c) $\Theta < 0$, with an antiferromagnetic transition at $T_{\rm N}$=$|\Theta|$.

Equation (1.21) has not been solved exactly as a typical many-body problem, because $\langle \boldsymbol{S}_i \cdot \boldsymbol{S}_j \rangle$ is too complicated to treat statistically, where an application of a molecular-field (MF) approximation, $\langle \boldsymbol{S}_i \cdot \boldsymbol{S}_j \rangle = \boldsymbol{S}_i \langle \boldsymbol{S}_j \rangle$, gives the Curie-Weiss law,

$$\chi = \frac{C}{T - \Theta}, \tag{1.22}$$

where Θ is the Weiss constant whose positive or negative value indicates a ferromagnetic or antiferromagnetic interaction, respectively. The Curie law (Eq. (1.18)) obviously corresponds with the Curie-Weiss law with Θ=0, as shown in Fig. 1.5(a).

In the system with a ferromagnetic exchange interaction, the Weiss constant is equivalent to the transition temperature of a ferromagnetic long-range ordering state as shown in Fig. 1.5(b), that is the Curie temperature $T_{\rm C}$,

$$T_{\rm C} = \Theta = \frac{2S(S+1)}{3k_{\rm B}} \sum_j J_j. \tag{1.23}$$

However, the experimental result of the Curie temperature is generally smaller than the estimated value from Eq. (1.23), indicating the inappropriateness of the MF theory (as a mean-field approximation), since the rough approximation $\langle \boldsymbol{S}_i \cdot \boldsymbol{S}_j \rangle = \boldsymbol{S}_i \langle \boldsymbol{S}_j \rangle$ is applied. The correlation function, $\langle \boldsymbol{S}_i \cdot \boldsymbol{S}_j \rangle$, indicating the degree of the correlation between two spins, develops near the phase transition having large spin fluctuation, that is the short-range ordering. Therefore, the MF theory neglecting the feature of the correlation function is justified when the temperature is sufficiently higher than the Weiss constant. Moreover, the inaccuracy in the MF theory gets remarkable with decreasing of the dimensionality from three-dimensional to one- or two-dimensional system, as will be discussed in § 1.3.

1.2.5 Molecular-field theory in ferromagnetic ordering state

The ferromagnetic Heisenberg model obeys the MF theory sufficiently above the Curie temperature ($T_{\rm C}$), as mentioned in § 1.2.4. Here we consider the behavior below $T_{\rm C}$ as schematically depicted in Fig. 1.6(b). All the spins below $T_{\rm C}$ tend to orient toward the same

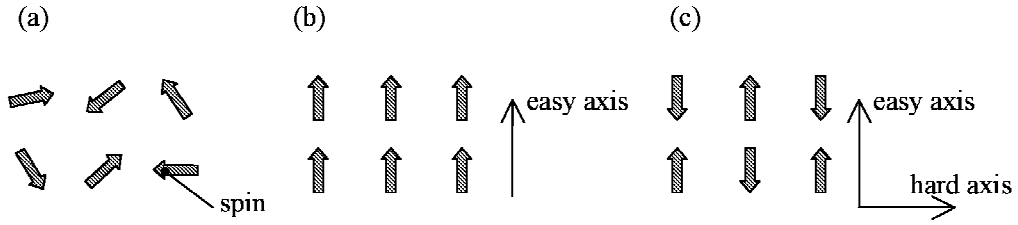

Figure 1.6: Schematic view of the spin configurations for (a) a paramagnetic state, (b) a ferromagnetic ordering state, and (c) an antiferromagnetic ordering state.

direction (the magnetic easy-axis), which will be subjected to the dipole-dipole interaction or the spin-orbit interaction, giving a spontaneous magnetization $\langle S \rangle$. The anisotropy in the susceptibility below $T_{\rm C}$ is characteristic of the ordering state. When the field parallel to the easy-axis is applied , the parallel susceptibility is estimated near $T_{\rm C}$ using power series method for $\langle S^2 \rangle$;

$$\chi_{\parallel} = \frac{C}{2(\Theta - T)}, \tag{1.24}$$

which is not correct in much lower temperatrue region than $T_{\rm C}$, since $\langle S^2 \rangle$ becomes large. Equation (1.24) indicates the susceptibility decreases down to $\sim$ zero at 0 K, where all the spins are frozen toward the easy-axis direction.

On the other hand, the susceptibilities in the field perpendicular to the easy-axis diverge below $T_{\rm C}$, since ferromagnetic Heisenberg systems usually have a small anisotropy giving identical spins in all directions, and thus the spontaneous magnetization along the easy-axis turns toward the field.

1.2.6 Molecular-field theory of antiferromagnetic (AF) ordering state

The magnetic easy-axis of antiferromagnets corresponds with the direction along which the spins are arranged in an antiparallel configuration as displayed in Fig. 1.6(c). The parallel susceptibility in an antiferromagnet is similar to that in ferromagnets which gradually decreases as temperature is lowered. In contrast, the perpendicular susceptibilities to the easy-axis, called as the magnetic hard-axes, are independent of temperature under the MF theory,

$$\chi_{\perp} = \frac{N(g\mu_{\rm B})^2}{4z|J|}. \tag{1.25}$$

The field dependence of the magnetization in the antiferromagnetic (AF) state indicates the spin flop transition reflecting the magnetic anisotropy as shown in Fig. 1.7. This phenomenon is observed at lower temperature than the Néel temperature, where the AF ordering

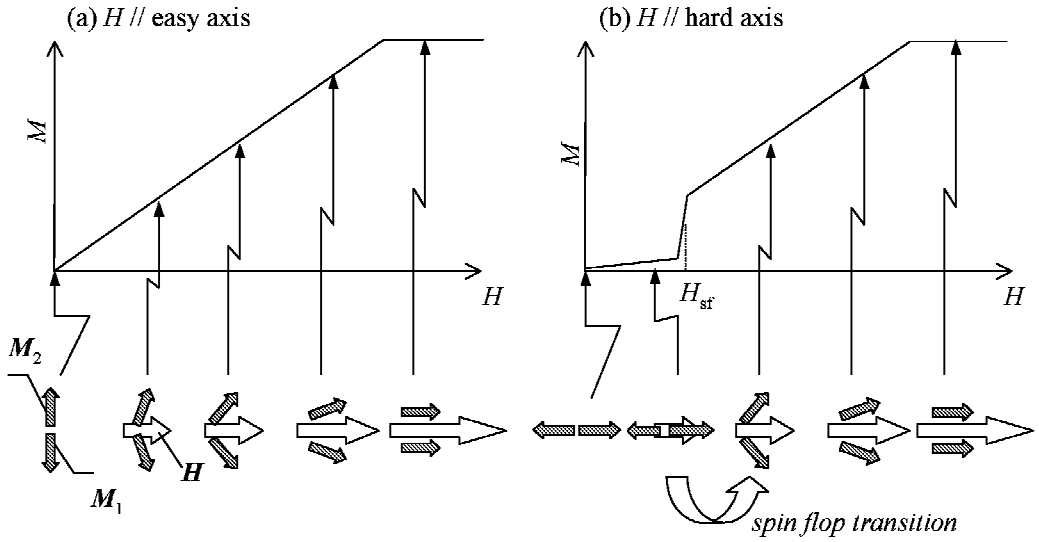

Figure 1.7: Field dependence of the magnetization for Heisenberg antiferromagnets with the field parallel to (a) the hard-axis and (b) the easy-axis with the spin flop transition at the spin flop field of $H_{\rm sf}$.

is sufficiently developed. When the field is applied perpendicular to the easy-axis, as shown in Fig. 1.7(a), the two sublattice magnetizations M_1 and M_2 are gradually canting toward the field direction. The net magnetization saturates to the constant of $|M_1 + M_2|$ in the external field H larger than the AF exchange field,

$$H_{\rm E} = \frac{2z|J|\langle S\rangle}{g\mu_{\rm B}}, \tag{1.26}$$

where z is the number of the nearest neighbor spins and $\langle S\rangle$ is the thermal average of the sublattice spins. Meanwhile, in the field parallel to the easy-axis (Fig. 1.7(b)), when the field is smaller than a critical field ($H_{\rm sf}$), the magnetization is hardly induced, which is exactly zero at absolute zero temperature. When the field gets larger than $H_{\rm sf}$, the sublattice magnetizations suddenly rotate to stabilize the magnetic energy, that is the spin flop transition. The spin flop field $H_{\rm sf}$ is described as

$$H_{\rm sf} = \sqrt{2H_{\rm A}H_{\rm E}/(1-\chi_{\parallel}/\chi_{\perp})}, \tag{1.27}$$

where $H_{\rm A}$ is the anisotropy field.

1.3 Low-dimensional magnetism

The neglect of the spin-spin correlation is not a serious problem in paramagnetic states of ordinary three-dimensonal magnets, because the short-range ordering region exists only just above the phase transition to long-range ordering state as discussed in § 1.2.4. However, when the dimensionality is reduced, the short-range order is extended to a wide temperature region, which makes the molecular-field (MF) theory useless.

Figure 1.8 shows the schematic view of low-dimensional magnets. The (bark) crystal of a low-dimensional magnet has the three-dimensional packing structure, and thus the three-dimensional magnetic dipole-dipole interaction always exists, which is featured by the weak and long-range contribution as described in Eq. (1.15). Meanwhile, the strong and short-range force, the exchange interaction, gives the low-dimensional network for the system. The difference between the low-dimensional and three-dimensional magnets is experimentally reflected in the specific heat or the susceptibility around the long-range ordering transition, since the reduction of the dimensionality gives the increase of the spin fluctuation. In this section, we discuss the behavior of the susceptibilities based on several low-dimensional magnet models.

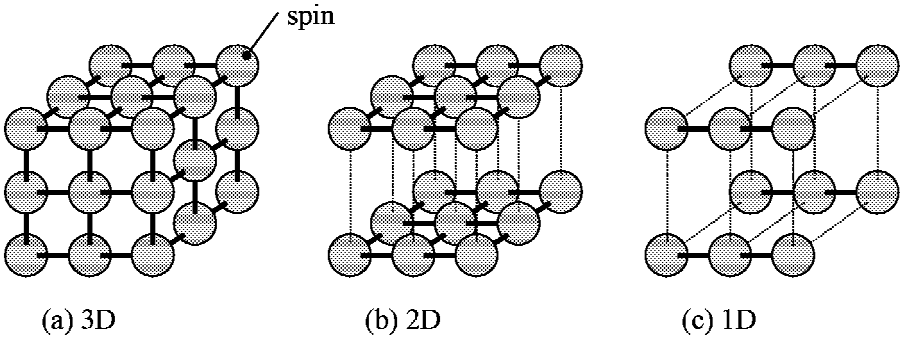

Figure 1.8: Schematic view of low-dimensional magnetic structures concerned with a simple cubic system. A sphere represents the spin connected by the exchange interaction (bold lines). (a) Three-dimensional (3D), (b) two-dimensional (2D), and (c) one-dimensional (1D) structures are represented.

1.3.1 One-dimensional Heisenberg antiferromagnet model

J. C. Bonner and M. E. Fisher [3] studied a linear chain of S=1/2 spins by exact calculations for N=2 to 11 with antiferromagnetic coupling. The Hamiltonian is

$$\hat{H} = -2J \sum_{i=1}^{N} [\boldsymbol{S}_i \cdot \boldsymbol{S}_j] - g\mu_{\mathrm{B}} \sum_{i=1}^{N} \boldsymbol{H} \cdot \boldsymbol{S}_i. \tag{1.28}$$

Figure 1.9 shows the result of the calculations, where the behavior of the susceptibility of an infinite chain at low temperatures is estimated by extrapolation. The intra-chain exchange interaction is approximately estimated at

$$J \approx k_{\mathrm{B}} T_{\mathrm{max}} / 1.282, \tag{1.29}$$

where T_{max} is the temperature at which the susceptibility shows a broad maximum.

To utilize the result for the infinite chain conveniently, a numerical fitting [4] has been carried out;

$$\chi = \frac{N g^2 \mu_{\mathrm{B}}^2}{k_{\mathrm{B}} T} \frac{A + BX + CX^2}{1.0 + DX + EX^2 + FX^3}, \tag{1.30}$$

where $X = |J| / k_{\mathrm{B}} T$, and the constant coefficients A=0.25, B=0.14995, C=0.30094, D=1.9862, E=0.68854, and F=6.0626.

1.3.2 Two-dimensional Heisenberg antiferromagnet model

The spin Hamiltonian for a two-dimensional square-lattice Heisenberg antiferromagnetic model [5] is described as

$$\hat{H} = -2J \sum_{\langle ij \rangle} \boldsymbol{S}_i \cdot \boldsymbol{S}_j - g \mu_{\mathrm{B}} \sum_i \boldsymbol{H} \cdot \boldsymbol{S}_i, \tag{1.31}$$

where the summation is carried out for all the nearest neighbors through the same exchange interaction J. The high temperature power series expansion method for the calculation of the sum over states gives the temperature dependence of the inverse susceptibility,

$$\frac{N g^2 \mu_{\mathrm{B}}^2}{2 \chi J} = 3\theta + \sum_{n=1}^{\infty} \frac{C_n}{\theta^{n-1}}, \tag{1.32}$$

where $\theta = k_{\mathrm{B}} T / 2JS(S+1)$ and coefficients C_n is calculated from the general formalism of the cumulant expansion displayed for S=1/2 in Table 1.1. Figure 1.10 shows the temperature dependence of the reciprocal susceptibility for several different spin values. The intra-layer exchange interaction is approximately estimated at

$$J = k_{\mathrm{B}} T_{\mathrm{max}} / 2(1.12S(S+1) + 0.10). \tag{1.33}$$

1.3.3 Spin-dimer model (Singlet-triplet model)

We consider N spins, where two S=1/2 spins coupled by the exchange interaction form a spin-dimer and there is no inter-dimer interactions. This is called the dimer model, or the singlet-triplet model in other words, because the ground and excited states of a dimer are singlet and triplet, respectively.

The Hamiltonian of this model is reduced to a simple summation of two-spins Hamiltonian,

$$\hat{H} = \frac{N}{2}[-2J\boldsymbol{S}_1 \cdot \boldsymbol{S}_2 - g\mu_{\mathrm{B}}(S_{1z} + S_{2z})H], \tag{1.34}$$

where the field is applied along the z-axis, $\boldsymbol{S}_1$ and $\boldsymbol{S}_2$ are each spin operators. This Hamiltonian is strictly solved through a statistical treatment, and gives the susceptibility for N spins:

$$\chi = \frac{Ng^2\mu_{\mathrm{B}}^2}{k_{\mathrm{B}}T} \frac{\exp(-2|J|/k_{\mathrm{B}})}{1 + 3\exp(-2|J|/k_{\mathrm{B}}T)}. \tag{1.35}$$

This model can be applied to substances having negligible inter-dimer interactions.

1.3.4 Alternating chain Heisenberg antiferromagnet model

An adoption of the inter-dimer interaction for the spin-dimer model is the alternating chain model which consists of one-dimensional sequence of $N/2$ dimers as shown in Fig. 1.11. The absence of the inter-dimer interaction, J', gives the correspondence with the dimer model, and conversely, J'=J gives the one-dimensional model (Bonner-Fisher model). The result of a numerical calculation [6] for α=J'/J=0 to 1 was fitted [7] as

$$\chi = \frac{Ng^2\mu_{\mathrm{B}}}{k_{\mathrm{B}}T} \frac{A + BX + CX^2}{1.0 + DX + EX2 + FX^3} \quad \text{and} \tag{1.36}$$

$$X = |J|/k_{\mathrm{B}}T, \tag{1.37}$$

where, when $0 \leq \alpha \leq 0.4$,

$$\begin{aligned}
A &= 0.25, \\
B &= -0.12587 + 0.22752\alpha, \\
C &= 0.019111 - 0.13307\alpha + 0.50967\alpha^2 - 1.3167\alpha^3 + 1.0081\alpha^4, \\
D &= 0.10772 + 1.4192\alpha, \\
E &= -0.0028521 - 0.42346\alpha + 2.1953\alpha^2 - 0.82412\alpha^3, \\
F &= 0.37754 - 0.067022\alpha + 6.9805\alpha^2 - 21.678\alpha^3 + 15.838\alpha^4,
\end{aligned}$$

and when $0.4 \leq \alpha \leq 1$,

$$\begin{aligned}
A &= 0.25, \\
B &= -0.13695 + 0.26387\alpha, \\
C &= 0.017025 - 0.12668\alpha + 0.49113\alpha^2 - 1.1977\alpha^3 + 0.87257\alpha^4, \\
D &= 0.070509 + 1.3042\alpha, \\
E &= -0.0035767 - 0.40837\alpha + 3.4862\alpha^2 - 0.73888\alpha^3, \\
F &= 0.36184 - 0.065528\alpha + 6.65875\alpha^2 - 20.945\alpha^3 + 15.425\alpha^4.
\end{aligned}$$

1.3.5 Three-dimensional interaction in low-dimensional magnets

There are three-dimensional interactions even in low-dimensional magnets, which give a magnetic long-range ordering transition whereas ideal low-dimensional magnets have no long-range order at a finite temperature except two-dimensional Ising spin systems. Therefore, the long-range ordering state in the low-dimensional Heisenberg magnets originates from the three-dimensional interactions. Oguchi [8] discussed the contribution of the three-dimensional interactions in low-dimensional magnets by means of a Green function, which is a general method to describe correlation functions. Figure 1.12(a) shows a one-dimensional chain system through the intra-chain interaction (J) along the z-direction with four nearest inter-chain interactions (J') along the x- and y-directions. The expression for the Néel temperature, $T_{\rm N}$, is obtained as follows:

$$\frac{k_{\rm B}T_{\rm N}}{|J|} = \frac{4S(S+1)/3}{I(\eta)}, \tag{1.38}$$

where

$$I(\eta) = \frac{1}{\pi^3}\iiint_0^\pi \frac{dq_x dq_y dq_z}{\eta(1-\cos q_x)+\eta(1-\cos q_y)+(1-\cos q_z)}, \tag{1.39}$$

$$\eta = J'/J, \tag{1.40}$$

where q_x, q_y, and q_z are the components of a wave number vector $\boldsymbol{q}$, and the extreme conditions η=0 and η=1 reduce this model to one-dimensional chains and a simple cubic-lattice structure, respectively. Equation (1.39) was numerically calculated giving the results for various η shown in Table 1.2.

For the quasi two-dimensional square-lattice model in the xy-layer with inter-layer interaction (J') along the z-direction as shown in Fig. 1.12 the similar expression with Eq. (1.39) is obtained in the following equation,

$$I(\eta) = \frac{1}{\pi^3}\iiint_0^\pi \frac{dq_x dq_y dq_z}{(1-\cos q_x)+(1-\cos q_y)+\eta(1-\cos q_z)}. \tag{1.41}$$

1.3.6 Spin reduction in low-dimensional magnets

The expected value of S_z for an S=1/2 spin in the ground state based on the simple MF theory is 1/2, however the improvement of the MF theory results in the reduction of the expectation value. The spin reduction is usually observed for quantum spin systems having small S, experimentally reflected in the perpendicular susceptibility at 0 K. The MF theory gives the perpendicular susceptibility,

$$\chi_\perp^0 = \frac{Ng^2\mu_{\rm B}^2}{4zJ}, \tag{1.42}$$

where z is the number of the nearest neighbor spins. The spin-wave theory [9] gives a extended result of Eq. (1.42) reflecting the spin reduction,

$$\chi_{\perp}(0) = \frac{\chi_{\perp}^{0}}{1+\alpha/2}\left[1 - \frac{\Delta S(\alpha)}{S} - \frac{e(\alpha)}{(2+\alpha)zS}\right], \tag{1.43}$$

where α represents the degree of the anisotropy: $\alpha = H_{\mathrm{A}}/H_{\mathrm{E}}$ using the anisotropy field (H_{A}) and the exchange field (H_{E}). The second term of the Eq. (1.43), $\Delta S(0)/S$, is the spin reduction for the sublattice magnetization, and the third term $e(\alpha)/(2+\alpha)zS$ is the correction for the real ground state spin energy. When the anisotropy field is smaller than the exchange field, that is $\alpha = H_{\mathrm{A}}/H_{\mathrm{E}} \ll 1$, Eq. (1.43) is reduced to

$$\chi_{\perp}(0) \approx \chi_{\perp}^{0}\left[1 - \frac{\Delta S}{S} - \frac{e(0)}{2zS}\right]. \tag{1.44}$$

Table 1.3 shows the value of $e(0)$ dependent on the lattice network and the number of the nearest neighbors, and Table 1.4 shows the spin reduction term by several methods.

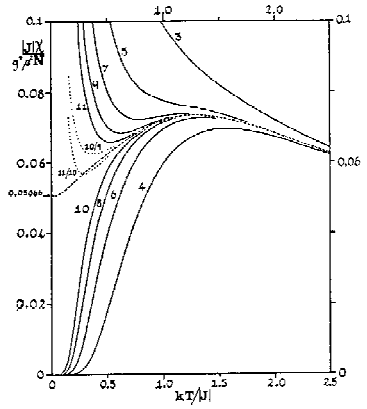

Figure 1.9: The temperature dependence of the antiferromagnetic susceptibility for S=1/2 finite Heisenberg chains (solid and dotted curves) and the estimated limit for infinite chains (dashed curve) [3].

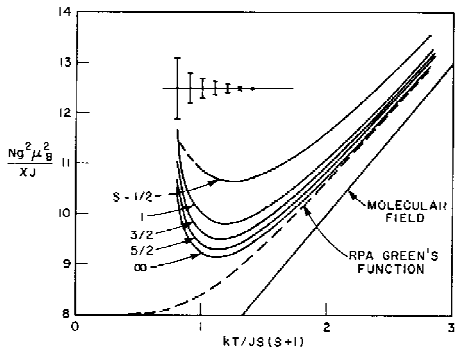

Figure 1.10: The temperature dependence of the reciprocal susceptibility for a two-dimensional square-lattice Heisenberg antiferromagnet model. Typical errors resulting from the extrapolation procedure are indicated on the figure and increase with decreasing temperature. The molecular field and random phase approximation (RPA) Green function susceptibility curves are also plotted [5].

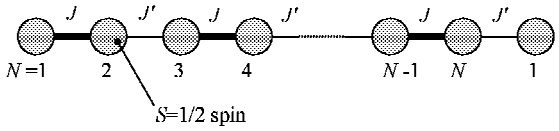

Figure 1.11: Schematic view of a one-dimensional alternating chain model. S=1/2 spins (circles) are connected through the exchange interactions J and J' alternately ($J \gg J'$).

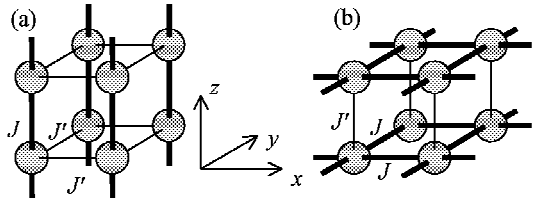

Figure 1.12: Low-dimensional magnetic structures based on a simple cubic lattice. (a) A quasi one-dimensional structure along the z-direction with inter-chain interactions in the x- and y-directions. (b) A quasi two-dimensional structure in the xy-layer with the inter-layer interaction along the z-direction.

Table 1.1: Coefficients C_n of series in Eq. (1.32) for S=1/2 [5].

n	1	2	3	4	5	6
C_n	4	2.667	1.185	0.149	–0.191	0.001

Table 1.2: The results of calculation $I(\eta)$ in Eq. (1.39) [8].

η	$I(\eta)$ (1D)	$I(\eta)$ (2D)
1	0.505	0.505
0.1	1.963	0.963
0.01	6.405	1.477
0.001	20.323	2.051
0.0001	-	2.608

Table 1.3: The values of $e(0)$ [9].

	z	spin wave	Fisher-Oguchi	Davis
linear chain	2	0.726	0.692	0.736
quadratic layer	4	0.632	0.572	0.656
simple cubic	6	0.582	0.548	0.599

Table 1.4: The values of spin reduction [9].

	spin wave	Fisher-Oguchi	Davis
linear chain	$-\frac{1}{2S}[1+\frac{1}{\pi}\ln 2\alpha]$	0.350	0.5185
quadratic layer	$0.197S^{-1}$	0.146	0.2363
simple cubic	$0.078S^{-1}$	0.090	0.1275

1.4 ESR

1.4.1 Fundamental principle of ESR

Electron spin resonance (ESR) is a favorable technique to investigate the environment of magnetic moments, which gives a large amount of information. An S=1/2 spin in an applied field $\boldsymbol{H}_0$ along the z-direction is described using the following equation of motion,

$$\hbar\frac{d\boldsymbol{s}}{dt} = \boldsymbol{\mu} \times \boldsymbol{H}_0. \tag{1.45}$$

The magnetic moment,

$$\boldsymbol{\mu} = (A\cos(\omega_0 t + \alpha), A\sin(\omega_0 t + \alpha), \text{const.}), \tag{1.46}$$

indicates that $\boldsymbol{\mu}$ is rotating around the z-direction with an angular velocity ω_0=$-\gamma H_0$ (Larmor precession) where γ is the gyromagnetic ratio.

The application of a field H_0 results in the Zeeman split between the states having opposite spins,

$$\Delta U = g\mu_{\mathrm{B}} H_0 = \frac{|\gamma|}{\hbar} H_0 = \hbar\omega_0. \tag{1.47}$$

Therefore, when an incident electromagnetic wave of the same energy with $\hbar\omega_0(=h\nu_0)$ is introduced, the spin in the lower state can absorb the electromagnetic wave with the transition to the higher state.

One of the important information from ESR is the g-value of the spin,

$$g = h\nu_0/\mu_{\mathrm{B}} H_0, \tag{1.48}$$

which is 2.0023 for a free electron spin, whereas generally the g-value in solid state substrates deviates from this value.

1.4.2 ESR line width and relaxation process

The ESR line width is an important factor to characterize the electronic structures. The line width is governed by the ESR relaxation process of the excited electrons to the higher state of the Zeeman split. Generally there are two kinds of the relaxation processes: between electrons and the lattice system (spin-lattice relaxation, T_1) and among spins (spin-spin relaxation, T_2). The spin-lattice relaxation process contributes to the line with of the metallic state having delocalized electrons, while the spin-spin relaxation governs the localized spin systems by the magnetic dipole-dipole interaction and the exchange interaction.

We compare with the electronic states between metal and magnetic insulator on the basis of the contribution to the ESR line width. Regardless of the electronic states, the magnetic dipole-dipole interaction exists as a spin-spin relaxation process. However, the line width

of the metallic state is contributed by the spin-lattice relaxation related to the relaxation time of the conductive carriers. The rapid motion of the carriers makes the line width by the dipole-dipole relaxation completely disappear due to the motional-narrowing process. In a similar way, the line width in the localized spin system is associated with the exchange interaction J which corresponds with the relaxation time of $J/\hbar$ giving the steep relaxation process (the exchange narrowing).

The quantum mechanical treatment for ESR, the Kubo-Tomita theory, gives a description of the ESR line width. We explain the useful expression of the line width on the basis of the second moment method, although we do not discuss the complicated theoretical process in detail here. We consider a system having the exchange interaction and the dipole-dipole interaction between spins, where the ESR signal is known to have a Lorentzian-type line shape. This line shape is described in a scale of the angular momentum, ω, as follows:

$$I(\omega) = \frac{\omega_d^2/\omega_e}{\pi}\left[\frac{1}{(\omega-\omega_0)^2+(\omega_d^2/\omega_e)^2}\right], \tag{1.49}$$

where ω_d^2 is the second moment of the dipole-dipole interaction, and ω_e is the angular momentum corresponding to the strength of the exchange field. From Eq. (1.49) the line width $\Delta\omega$ is roughly estimated at

$$\Delta\omega \sim \frac{\omega_d^2}{\omega_e}, \tag{1.50}$$

where a constant prefactor dependent on the spin configurations is actually added, such as $10/3$ for the simple cubic structure.

The estimate of ω_d is numerically carried out, which makes a qualitative discussion for the origin of the line width possible, nevertheless the calculation of ω_e is difficult. The description[1] of ω_d is expressed as

$$\omega_d^2 = \frac{3S(S+1)}{4}\frac{g^4\mu_{\mathrm{B}}^4}{\hbar^2}\sum_k \frac{(3\cos^2\theta_{jk}-1)^2}{r_{jk}^6}, \tag{1.51}$$

where the r_{jk} is the distance between the j-spin located in the origin and the k-spin, θ_{jk} is the angle between the direction to the k-spin from the origin and an applied field. The summation is carried out for 100–1000 spins.

1.4.3 ESR of low-dimensional magnets

The ESR spectra of low-dimensional magnets behave characteristically because of the strong influence for the relaxation process of the excited spins by the resonance. Here, temperature dependence of the line width and the g-value shift are introduced featuring the low-dimensional spin system.

[1]It is worth noting that the calculation in Eq. (1.51) must be carried out on the basis of the CGS system of units.

The temperature dependence of the ESR line width for three-dimensional antiferromagnets are obtained as

$$\Delta H(T) = \Delta H(\infty)\frac{C}{\chi T}\zeta^{\frac{3}{2}}, \tag{1.52}$$

where χ is the spin susceptibility, $\Delta H(\infty)$ is the line width as $T \to 0$, C is the Curie constant, and ζ is a function dependent on temperature. For three-dimensional magnets, ζ is approximated to $\sim$1 in the high temperature region, and thus the temperature dependence of the line width is proportional to $(\chi T)^{-1}$, however ζ is not so simple for low-dimensional magnets. Figure 1.13 shows the temperature dependence of ζ based on the theory for three-dimensional antiferromagnets, the experimental results of two-dimensional Heisenberg antiferromagnet ($CuF_2{\cdot}2H_2O$), and one-dimensional magnet ($KCuF_3$), indicating that the difference in the temperature-dependent behavior becomes conspicuous as the dimensionality is lowered. This behavior of ζ is caused from the low-dimensional relaxation effect, which finally gives the line width proportional to χT [10]. This approximation is experimentally known to be applied in the high temperature region above the temperature at which the thermal energy becomes comparable to the exchange interaction. Figure 1.14 shows the ESR line width of $CuCl_2{\cdot}2NC_5H_5$ [10] which is a typical one-dimensional Heisenberg antiferromagnet with the exchange interaction of 13.4 K and a three-dimensional antiferromagnetic ordering temperature T_N=1.135 K. The solid curve of the normalized χT indicates a good agreement with the experimental result.

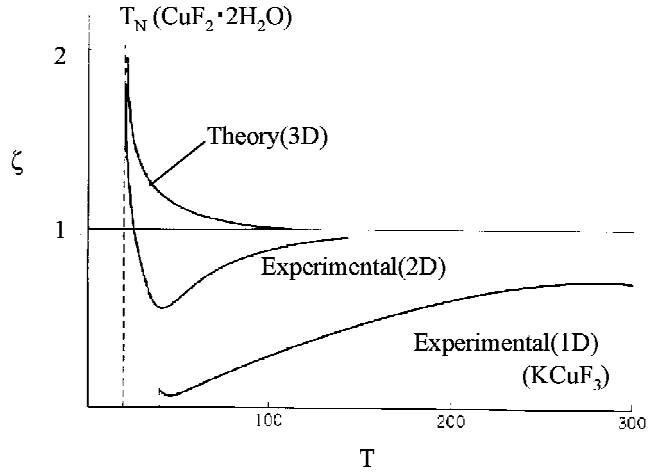

Figure 1.13: Temperature dependence of the factor ζ in Eq. 1.52. The theoretical curve for the three-dimensional system becomes constant in much higher temperature region than the Néel temperature, whereas the experimental results for low-dimensional magnets indicate a large deviation from the theoretical curve.

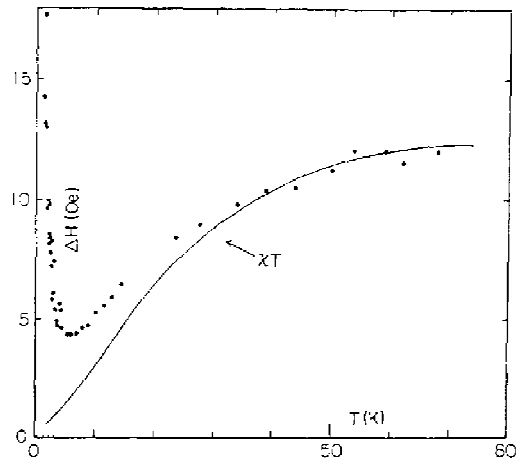

Figure 1.14: Temperature dependence of the ESR line width for $CuCl_2{\cdot}2NC_5H_5$. The solid curve is the normalized χT at 77 K [10].

1.5 Thermoelectric power

The thermoelectric power is one of the transport phenomena which appear in electrical conductors and is a sensitive probe of carriers [11]. The thermoelectric power is describes as the entropy per carrier.

The temperature dependent behavior of the thermoelectric power depends on the electronic state of the system, metal or semiconductor. In a metal as a degenerated electron gas at temperatures much lower than the Fermi temperature, the thermoelectric power is described as

$$S \approx \frac{k_{\mathrm{B}}}{q}\frac{k_{\mathrm{B}}T}{E_{\mathrm{F}}}, \tag{1.53}$$

where E_{F} is the Fermi energy and q equals $-|e|$ or $|e|$ for the electron or hole carrier, respectively. Thus, the characteristic thermoelectric power of metals decreases with the decrease of temperature and is smaller than $k_{\mathrm{B}}/|e| \approx 87\mu\mathrm{V/K}$. Contrarily, in semiconductors, the electron carriers excited to the conduction band having the energy gap of E_g contributes to the thermoelectric power,

$$S \approx -\frac{k_{\mathrm{B}}}{q}\frac{E_g}{2k_{\mathrm{B}}T}, \tag{1.54}$$

indicating the characteristic contrast with that of metals, especially in the temperature dependence. Considering the roles of electron and hole carriers, Eq. (1.54) is extended to as follows:

$$S = \frac{k_{\mathrm{B}}}{e}\left[\frac{b-1}{b+1}\frac{E_g}{k_{\mathrm{B}}T} + \frac{3}{4}\ln\frac{m_e}{m_h}\right],\ b = \mu_e/\mu_h, \tag{1.55}$$

where μ_e, μ_h and m_e, m_h are the mobilities and effective masses of the electrons and holes, respectively. Regardless of the electronic state which is metal or insulator, the thermoelectric power provides two information: the sign of the charge of the carriers and the characteristic energy associated with the carriers, that is, the Fermi energy for a metal and the energy gap for a semiconductor.

1.5.1 Thermoelectric power in strongly correlated systems

The simplest model in a strongly correlated system is the Hubbard model as described in § 1.1.2. The high-temperature limit for the thermoelectric power of a system of strongly correlated localized electrons is governed by the entropy change when an electron is added to the system. That is to say,

$$S = -\frac{1}{e}\left(\frac{d\sigma}{dN}\right)_{E,V}, \tag{1.56}$$

where σ is the entropy of the system, N is the number of electrons, and E and V are the internal energy and volume, respectively. The entropy can be calculated in the high

temperature region by $\sigma=k_{\rm B}\ln g$, where g is the degeneracy of the states. Therefore, the thermoelectric power is estimated at

$$S=-\frac{k_{\rm B}}{e}\frac{d\ln g}{dN}. \tag{1.57}$$

This relation indicates that the thermoelectric power reflects the entropy per carrier. In the regime of the electronic state governed by the on-site Coulomb repulsion, the degeneracy of the states is

$$g=\frac{N_A!}{N!(N_A-N)!}2!, \tag{1.58}$$

where N_A and N are the number of the sites and the electrons, respectively. Equation (1.58) leads to the thermoelectric power [12],

$$S=-\frac{k_{\rm B}}{|e|}\ln\frac{2(1-\varrho)}{\varrho}, \tag{1.59}$$

where ϱ is the number of electrons per site, and indicates temperature-independent behavior.

Figure 1.15 shows the thermoelectric power of quinolinium$(TCNQ)_2$ [13,14] as an example for application of this relation, which is almost temperature independent in the high temperature region. In this compound, the number of electrons per TCNQ is considered to be 1/2, giving S=−60 μV/K from Eq. (1.59), which shows good agreement with the experimental result.

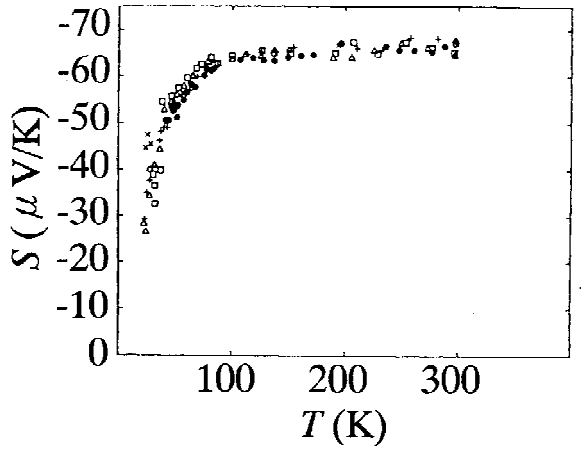

Figure 1.15: Thermoelectric power of quinolinium$(TCNQ)_2$ [13] explained as a strongly correlated system [14].

1.6 Charge transfer salts

We explain a few topics on charge transfer (CT) salts: the charge transfer interaction stabilizing the CT salts, historical background of the CT salts, and a useful band calculation method to describe the electronic states of the CT salts.

1.6.1 Charge transfer interaction

A charge transfer (CT) salt consists of a donor and an acceptor, where the donor gives electron(s) to the acceptor. The CT interaction explained by Mulliken gives the ground state Ψ stabilized by the charge transfer as a quantum resonant state between the initial state without the charge transfer (Ψ_{DA}) and the final state in which one electron charge transfer was completed ($\Psi_{\mathrm{D^+A^-}}$),

$$\Psi = a\Psi_{\mathrm{DA}} + b\Psi_{\mathrm{D^+A^-}}. \tag{1.60}$$

When the system has a small CT interaction with the normalizing coefficient $a \gg b$, the energy of Ψ is obtained using a second perturbation method,

$$E = E_{\mathrm{DA}} - \frac{(H - SE_{\mathrm{DA}})^2}{E_{\mathrm{D^+A^-}} - E_{\mathrm{DA}}}, \tag{1.61}$$

where E_{DA} and $E_{\mathrm{D^+A^-}}$ are the eigen values of Ψ_{DA} and $\Psi_{\mathrm{D^+A^-}}$, respectively, and the resonance integral H and the overlap integral S are as follows:

$$H = \int \Psi_{\mathrm{DA}} \hat{H} \Psi_{\mathrm{D^+A^-}} d\tau, \tag{1.62}$$

$$S = \int \Psi_{\mathrm{DA}} \Psi_{\mathrm{D^+A^-}} d\tau. \tag{1.63}$$

The second term of Eq. (1.61) must be non-zero for the energy stabilization by the CT interaction, and additionally, the larger value gives the stronger stabilization for the resonant state. Thus, a small denominator ($E_{\mathrm{DA}} - E_{\mathrm{D^+A^-}}$) and a large numerator ($H - SE_{\mathrm{DA}}$) are favorable for the stabilization in the CT salts. The former condition needs the small energy for the charge transfer from the donor to the acceptor, corresponding to the small ionization energy of the donor and the large electron affinity of the acceptor. The latter one requires a large overlap between Ψ_{DA} and $\Psi_{\mathrm{D^+A^-}}$, that is, the large overlap integral between the donor and acceptor molecular orbitals.

1.6.2 Outline of organic conductors

Figure 1.16 shows structures of several donor molecules and the ellipses of the molecules. The syntheses and physical characterization of a large number of organic materials with unusual electrical and magnetic properties have been started in the 1960's. An important organic conductor, TTF·TCNQ [15] shown in Fig. 1.17, consisting of two kinds of molecules

TCNQ (7,7,8,8,-tetracyano-p-quinodimethane) and TTF (tetrathiafulvalene) was synthesized in 1970, where the the metallic conductivity above 60 K [16] became a center of attraction. After the appearance of TTF·TCNQ, an innovative step was the discovery of the superconductivity below 1 K under pressure of about 5–12 kbar in $TMTSF_2X$ (X=monovalent anions) [17] called as "Bechgarrd salts". The crystallographic feature of the Bechgarrd salts is the one-dimensional stacking structure of donor molecules as shown in Fig. 1.18, which gives the physical properties of one-dimensional electronic systems, such as an spin-density wave (SDW) ground state. Afterward, an epock-making molecule BEDT-TTF (or ET; bis(ethylenedithio)tetrathiafulvalene), which has additional four outer sulfur atoms on the outside of the TTF skeleton prepared in 1972, has given the superconductivity under ambient pressure. Typical BEDT-TTF salts have quasi two-dimensional electronic states, which contrast with the Bechgarrd salts. The critical temperature of the superconductivity in the CT salts was raised to 10.4 K of κ-$(BEDT\text{-}TTF)_2Cu(NCS)_2$ synthesized in 1987 [18]. Furthermore, κ-$(BEDT\text{-}TTF)_2Cu[N(CN)_2]Cl$ was raised to 12.8 K under pressure of 0.3 kbar.

The structural feature of these salts is the donor molecules based on the TTF skeleton, therefore these salts can be named as "TTF-based charge transfer salts".

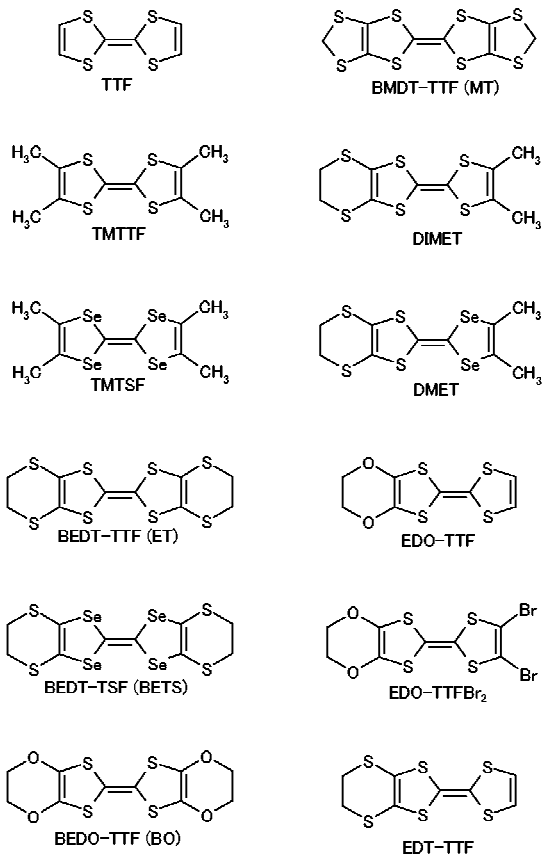

Figure 1.16: Structures of important donor molecules.

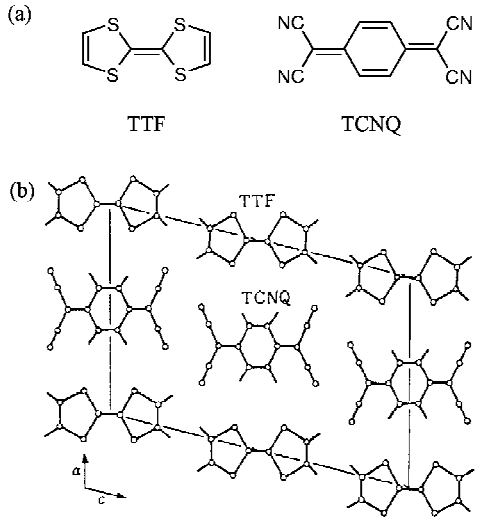

Figure 1.17: (a) Molecular structures of TTF and TCNQ. (b) Crystal structure of TTF·TCNQ [16].

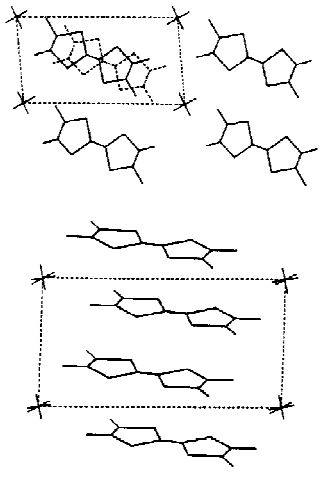

Figure 1.18: Crystal structure of $TMTSF_2X$ (X=PF_6, AsF_6, SbF_6) [17].

1.6.3 Band calculation

TTF-based organic charge transfer salts give a large variety of low dimensional electronic states consisting of π-electrons, from metallic states to insulating states. A band calculation [19] based on the tight-binding approximation is a powerful method to describe the metallic states.

The molecular orbitals of the donor are represented by the extended Hückel method as a linear combination of the atomic Slater orbitals, since the size of the donor molecules is large. The inter-molecular overlap S of the HOMO is calculated, and the transfer integrals t are estimated using the relation $t = ES$, where E is a constant of the order of energy of the HOMO. The value of -10 eV for E is ordinarily used [19], because it has given realistic values of the transfer integrals for a number of CT salts. Using a standard tight-binding method through the one-electron approximation, the band structure of the conduction band and the shape fo the Fermi surface are obtained.

Here, we introduce two examples of the band calculations: $(TMTSF)_2AsF_6$ [20] and β'-$(BEDT\text{-}TTF)_2AuCl_2$ [21] . Figure 1.18 shows the stacking structure of the TMTSF salt having strong one-dimensional overlap along the a-axis, and actually the estimated band structure shown in Fig. 1.19 has a one-dimensional Fermi surface consistent with the metallic conductivity. In contrast, the band structure of β'-$(BEDT\text{-}TTF)_2AuCl_2$ also indicates a one-dimensional Fermi surface as shown in Fig. 1.20, whereas the band structure is inconsistent with the semiconductive behavior implying the Mott insulating state. (The detail of the crystal structure and resistivity for the β'-type salt is discussed in § 1.8.) This inconsistency between the calculation and the experiment is considered to come from the strong on-site Coulomb interaction ignored on the basis of the one-electron approximation.

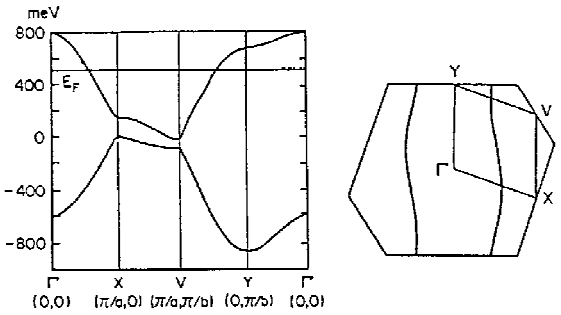

Figure 1.19: Band structure and the Fermi surface of $TMTSF_2AsF_6$ based on the crystal structure shown in Fig. 1.18 [20].

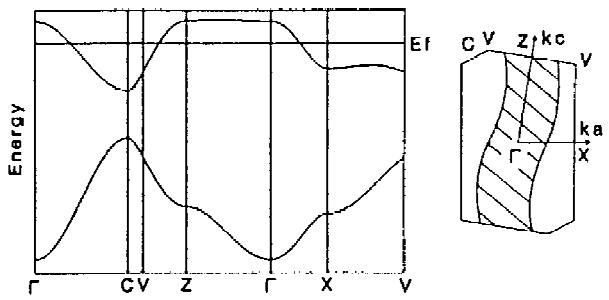

Figure 1.20: Band structure and the Fermi surface of β'-(BEDT-TTF)$_2$AuCl$_2$ [21].

1.6.4 Mott insulator and dimerization in 2:1 salts

The band calculation based on the one-electron approximation as discussed in § 1.6.3 cannot be employed to CT salts in the Mott insulating state. We discuss a suitable model to describe the electronic state of the Mott insulators. A structural feature of the CT salts in the Mott insulator regime is the strong dimerization of the donor molecules,[2] and thus we here treat the strongly dimerized system with 2:1 ratio of the donor to anion.

The dimerization of the donors through the intra-dimer transfer integral, $t_{\rm intra}$, gives an energy gap of $2t_{\rm intra}$ between the lower and upper orbitals as shown in Fig. 1.21(b). Here, we have two extreme approaches to treat the transfer integrals between dimers $t_{\rm inter}$ ($\ll t_{\rm intra}$): a free electron approximation and a tight-binding approximation. The former condition corresponds to the negligible on-site Coulomb interaction U_0, where a free electron band model can be applied giving two bands produced from the lower and upper orbitals, respectively, and the Fermi surface (Fig. 1.21(c)). However, when the contribution of U_0 is large, we should consider the tight-binding approximation shown in Fig. 1.21(d), where a sequence of the upper orbitals of dimers are depicted. If there is an electron transfer from an orbital to the adjacent orbital, the energy of the electron configuration gets larger than that of the ground state by $U_{\rm eff}$. From the two configurations, moreover, $t_{\rm inter}$ produces the two band structures having the band width W (Fig. 1.21(e)). These two bands are called the Hubbard sub-bands, which is different from ordinary band structures because of the band gap E_g is originated from the electron-electron repulsion, and the each atom has an electron in both upper and lower bands as depicted in Fig. 1.21(d). As a result, the energy gap of the Mott insulator is considered to be

$$E_g = U_{\rm eff} - W. \tag{1.64}$$

[2]However, the dimerized donor doesn't always generate the Mott insulating state, such as (BMDT-TTF)$_2$Au(CN)$_2$, whose donor molecules are strongly dimerized, while the conductive behavior is metallic.

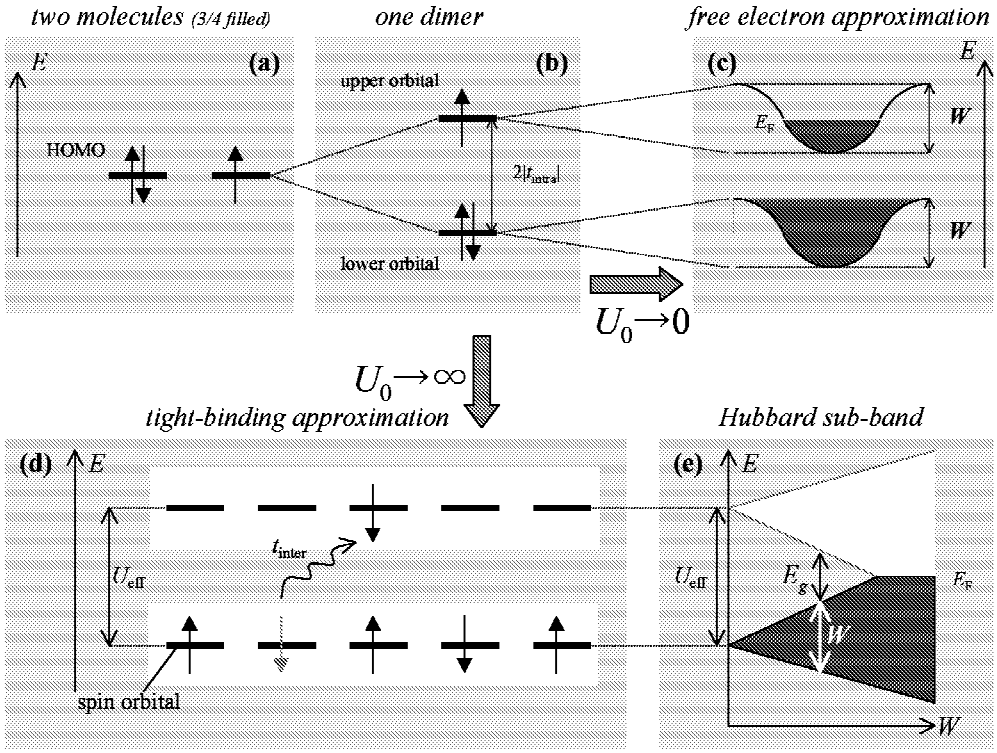

Figure 1.21: Several energy configurations based on the dimer structure of 2:1 salts with 3/4-filling orbitals. (a) Isolated two HOMO energies. (b) An intra-dimer transfer integral (t_{intra}) gives two energy states splitted by the energy of $2|t_{\mathrm{intra}}|$. (c) A free electron approximation leads to the two bands when the inter-dimer interaction (t_{inter}) is much smaller than t_{intra}. The band width W is associated with t_{inter}. (d) A sequence of spin orbitals of the upper orbitals in the strongly correlated localized system where the on-cite Coulomb interaction $U_{\mathrm{eff}} \gg t_{\mathrm{inter}}$. (e) The Hubbard sub-band structure. The band width is considered to come from t_{inter}. When $U_{\mathrm{eff}} < W$, the system becomes a metallic state.

1.7 Aim of research

The variety of electronic states in the charge transfer (CT) salts is caused by the competition between the transfer integral and the Coulomb interaction, that is, a metallic state appears when the transfer integral is superior to the Coulomb interaction, whereas the Coulomb interaction superior to the transfer integral leads to an insulating state as a Mott insulator where the π-electrons are localized on the donor molecules. This insulating state, where the one-electron band picture on the electronic state fails (§ 1.6.3), results in the appearance of localized magnetic moments on the molecules, which is the most characteristic feature of these compounds as a localized spin system. Consequently, the localized magnetic moments of the π-electrons aligned on the low dimensional lattice of the molecules provide a low-dimensional magnetic system.

In Fig. 1.22, the correlation between the resistivities and the susceptibilities at room temperature is mapped for various charge transfer salts to see how Mott insulators are featured. Here, we classify the CT salts into Mott insulators, metals, and band insulators based on the temperature dependence of the resistivity and the behavior of the susceptibilities. Namely, the insulators are defined as the materials whose conductivity is explained in terms of the activation process, while the conductivity shows an increasing trend with lowering of the temperature in the metals. The Mott insulator is characterized with the presence of localized magnetic moments whose values are expected for S=1/2, whereas no localized spins are present in the band insulator. As explained consistently with the definitions, the Mott insulators occupy a specific region (shaded area) having large resistivities and susceptibilities, most of which are isolated from the metallic compounds (circles) and the band insulators (diamond). It is worth noting that the application of pressure, which works to reduce the resistivities, makes Mott insulators changed to metals through a critical region.

Here, we have a group of molecular-based Mott insulators which have a specific structural feature, that is, dimerization or trimerization of donor molecules in their crystals. In these materials, the strength of the on-site Coulomb interaction is roughly represented by that of the intra-dimer/trimer transfer integral (t_{intra}) as discussed in § 1.1.3, which is in the same order of magnitude to the inter-dimer/trimer transfer integral(t_{inter}). Therefore, the ratio between t_{intra} and t_{inter}, which depends on the degree of dimerization/trimerization and thus can be controlled by changing temperature and/or pressure, is varied to make a systematic investigation with a large variety of Mott insulators including those located just around the metal-insulator border.

The purpose of this work, therefore, is to investigate systematically the magnetic and electrical properties of dimer/trimer-based Mott insulators by means of the magnetic susceptibilities, ESR spectra, resistivities, and thermoelectric powers. We aim at seven CT salts covering the whole Mott-type insulator region shown in Fig. 1.22 (closed squares), where the well investigated κ-type salts (marked by l, m, and n) exist at the bottom and left-side parts

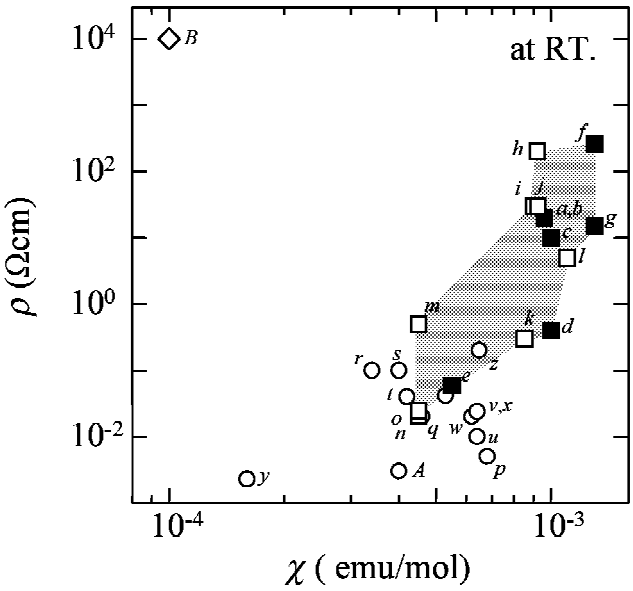

Figure 1.22: The diagram of the resistivities vs susceptibilities at room temperature for various TTF-based charge transfer salts: Mott insulators (square), metallic compounds (circle), and band insulators (diamond). The relation between marks and the compounds are summarized in Table 1.5. Closed squares are the target salts in this work.

of the region. The structure and physical properties are overviewed in § 1.8.5. The seven CT salts containing two newly-synthesized compounds are as follows:

1. β'-(BEDT-TTF)$_2$ICl$_2$ (the β'-ICl$_2$ salt)
2. β'-(BEDT-TTF)$_2$AuCl$_2$ (the β'-AuCl$_2$ salt)
3. (BEDT-TTF)$_2$GaCl$_4$ (the GaCl$_4$-salt)
4. α'-(BEDT-TTF)$_2$IBr$_2$ (the α'-IBr$_2$ salt)
5. (EDO-TTFBr$_2$)$_2$AsF$_6$
6. (BMDT-TTF)$_3$ClO$_4$(1,2-dichloroethane) (the ClO$_4$ salt)
7. (BMDT-TTF)$_3$AsF$_6$(1,1,2-trichloroethane) (the AsF$_6$ salt)

which will be referred to as the each anion's name, if any confusion. The No. 5 and 7 are the new salts whose crystal structures are summarized in § 3.4.1 and 3.6.1. The other crystal structures are explained in § 1.8 with the reported results of several physical properties.

Table 1.5: The resistivities and susceptibilities at room temperature for several charge transfer salts.

		ρ (- cm)	χ (10^{-3} emu/mol)
a	β'-(BEDT-TTF)$_2$ICl$_2$	20	0.96
b	β'-(BEDT-TTF)$_2$AuCl$_2$	20	0.96
c	(BEDT-TTF)$_2$GaCl$_4$	10	1.0
d	α'-(BEDT-TTF)$_2$IBr$_2$	0.4	1.0
e	(EDO-TTFBr$_2$)$_2$AsF$_6$	0.06	0.5
f	(BMDT-TTF)$_3$ClO$_4$DCE [a]	260	1.3
g	(BMDT-TTF)$_3$AsF$_6$TCE [b]	15	1.3
h	α'-(BEDT-TTF)$_2$AuBr$_2$ [22]	200	0.92
i	α'-(BEDT-TTF)$_2$CuCl$_2$ [22]	30	0.90
j	α'-(BEDT-TTF)$_2$Ag(CN)$_2$ [22]	30	0.93
k	α'-(BEDT-TTF)$_2$Au(CN)$_2$	0.3	0.85
l	(C1TET-TTF)$_2$Br$_2$ [23]	5	1.1
m	κ-(BEDT-TTF)$_2$Cu[N(CN)$_2$]Cl [24]	0.5	0.45
n	κ-(BEDT-TTF)$_2$Cu[N(CN)$_2$]Br [25]	0.021	0.45
o	κ-(BEDT-TTF)$_2$CuS(CN)$_2$ [18]	0.025	0.45
p	α-(BEDT-TTF)$_2$I$_3$ [26]	0.005	0.68
q	β-(BEDT-TTF)$_2$I$_3$ [26]	0.02	0.46
r	β-(BEDT-TTF)$_2$AuI$_2$ [27]	0.10	0.34
s	(TTF)$_2$CuCl$_2$ [28]	0.4	0.1
t	(BEDT-TTF)$_2$ClO$_4$TCE$_{0.5}$ [29]	0.04	0.42
u	(BEDT-TTF)$_2$BF$_4$TCE$_{0.5}$ [30]	0.01	0.64
v	(BEDT-TTF)$_2$BF$_4$DBE$_{0.5}$ [c] [30]	0.024	0.64
w	(BEDT-TTF)$_2$BF$_4$DCE$_{0.5}$ [30]	0.04	0.53
x	(BEDT-TTF)$_3$(ClO$_4$)$_2$ [29]	0.02	0.62
y	(TMTSF)$_2$AsF$_6$ [21]	0.002	0.16
z	(TMTTF)$_2$AsF$_6$	0.2	0.65
A	(BMDT-TTF)$_2$Au(CN)$_2$ [32]	0.003	0.40
B	(BEDT-TTF)HgBr$_3$	10000	0.10

[a]DCE; 1,2-dichloroethane.
[b]TCE; 1,1,2-trichloroethane.
[c]DBE; 1,2-dibromoethane.

1.8 Crystal structures and reported physical properties

We here introduce the crystal structures and the reported results of the physical properties of the charge transfer salts targeted in the present work, and in addition, the κ-type salts which are considered to be in the Mott insulating state. See § 3.4.1 and 3.6.1 for the crystal structure of (EDO-TTFBr$_2$)$_2$AsF$_6$ and (BMDT-TTF)$_3$AsF$_6$(1,1,2-trichloroethane), respectively.

1.8.1 β'-(BEDT-TTF)$_2$X (X=ICl$_2$, AuCl$_2$)

β'-(BEDT-TTF)$_2$X (X=ICl$_2$, AuCl$_2$) [21, 33–35], which are located with marks a and b around the top of the shaded region in Fig. 1.22, have the same structure as shown in Fig. 1.23, where the b-axis is the stacking direction of dimerized molecules and the c-axis corresponds with the side-by-side direction. The transfer integrals between donor molecules are indicated in Fig. 1.23(c). Since the largest transfer integral $t_{\rm b1}$ is more than 2 times larger than the other transfer integrals, BEDT-TTF molecules are strongly dimerized by face-to-face contact $t_{\rm b1}$ in the bc-plane.

Figure 1.24 shows several reported results of the physical properties. The temperature dependence of the resistivity [36] is shown in Fig. 1.24(a) with the room temperature conductivity about 0.03 S/cm and an activation energy of 0.12 eV. The temperature dependence of the susceptibility [36] is shown in Fig. 1.24(b) where there is no comment on the analysis. Taking account of the ESR intensity and the line width shown in Fig. 1.24(c) and (d) [37], respectively, the behavior of the susceptibility in the low temperature region implies the antiferromagnetic ordering below $\sim$ 20 K, however, the susceptibility is very small as a localized spin system. Thus, we consider that much detailed studies of the magnetic properties are needed to discuss the electronic states of Mott insulators systematically. The antiferromagnetic resonance [38] has been studied as shown in Fig. 1.25 indicating the antiferromagnetic transition in the low temperature region.

1.8.2 (BEDT-TTF)$_2$GaCl$_4$

(BEDT-TTF)$_2$GaCl$_4$ [39] marked by c is located near the β'-salts in Fig. 1.22. Figures 1.26 and 1.27 show the crystal structures for (BEDT-TTF)$_2$GaCl$_4$. The crystal structure consists of four crystallographically independent BEDT-TTF molecules (molecules A, B, C and D), where the packing structure along the stacking direction shown in Fig. 1.26 indicates the strong dimerization between A–B molecules and C–D molecules. Figure 1.27 shows the stacking along the b-axis forming the dimerized A–B and C–D pairs through the intra-dimer transfer integrals $t_{\rm intra}$=$t_{\rm b3}$ and $t_{\rm b1}$, respectively. The strength of the dimerization is evidenced by the considerably large intra- to inter-dimer transfer integral ratio $t_{\rm b3}/t_{\rm p3}$=5.3, $t_{\rm b1}/t_{\rm p1}$=2.8.

The temperature dependence of the resistivity [39] is shown in Fig. 1.28(a) with the room temperature conductivity of about 0.1 S/cm and an activation energy of 0.21 eV. The temperature dependence of the susceptibility [39] is shown in Fig. 1.28(b) which was measured on randomly oriented crystals using a Faraday balance below 0.9 T. The room temperature susceptibility is $\sim 8 \times 10^{-4}$ emu/mol and the temperature dependence indicates an rise below 20 K. Figure 1.29 shows the result of the ESR measurement [39]. They insist the antiferromagnetic transition at low temperatures.

1.8.3 α'-(BEDT-TTF)$_2$IBr$_2$

α'-(BEDT-TTF)$_2$IBr$_2$ [40,41] is located at the lower right place (d) in the Mott insulator region (Fig. 1.22). The structure of this salt shown in Fig. 1.30 contains two independent BEDT-TTF molecules (molecules A and B) coupled weakly through the largest transfer integral (t_{b2}), which are arranged on the ab-plane. The each A and B molecules forms stacking structures along the a-axis as shown in Fig. 1.30, however the strongest transfer integral t_{b2} is not the necessarily featured by face-to-face inter-molecular contacts.

The temperature dependence of the resistivity [36] is shown in Fig. 1.31(a) with the room temperature conductivity of 3 S/cm, an activation energy about 0.16 eV around room temperature, and in addition, a large anomalous change at about 200 K. The temperature dependence of the susceptibility [36] is shown in Fig 1.31(b) indicating a maximum around 60 K, which is consistent with the temperature dependence of the ESR intensity shown in Fig. 1.32. They suggest an structural phase transition at 60 K.

1.8.4 (BMDT-TTF)$_3$ClO$_4$(1,2-dichloroethane)

The crystal structure of (BMDT-TTF)$_3$ClO$_4$(1,2-dichloroethane) [42,43] as a weak trimer system is shown in Fig. 1.33 having two independent BMDT-TTF molecules, A and B. The bond lengths of the donor molecules summarized in Table 1.6 imply the charge separation between A and B molecules. The donor molecules form a two-dimensional sheet in the ac-plane, and the anion and solvent molecules are sandwiched in every gallery of donor sheets separate the molecular stacking layer along the b-axis. Figure 1.34 shows the packing of the donor molecules in the ac-plane, where the largest transfer integral t_{c3} along the diagonal side-by-side direction gives leaning trimer units. The ClO_4 salt is located at the right-side edge of the Mott insulator region.

No physical property has been reported on this salt except the room temperature conductivity of ca. 1 S/cm.

1.8.5 κ-(BEDT-TTF)$_2$Cu(SCN)$_2$

The κ-type salts are well investigated since they give the highest T_C to the superconducting state. The electronic state around room temperature is understood to be a Mott insulating

state, and thus we introduce the physical properties of the κ-(BEDT-TTF)$_2$Cu(SCN)$_2$ for the comparison with this work.

The crystal structure [46] of κ-(BEDT-TTF)$_2$Cu(SCN)$_2$ viewed along the molecular long axis is shown in Fig. 1.35. The κ-type salts have a crystallographic feature of the strongly dimerized donors arranged two-dimensionally, which is contrast with the standard face-to-face stacking structure shown in a large number of CT salts. The band structure [46] is shown in Fig. 1.36. The strongly dimerization makes the band structure to be an effective half-filled state, and the Fermi surface indicates the quasi two-dimensionality of this salt.

The temperature dependence of the resistivity along the b-axis [18,44] is shown in Fig. 1.37(b) with the room temperature conductivity of about 14 S/cm. The resistivity is metallic down to around 250 K with an upturn around 90 K, and after passing through the maximum at 90 K, the resistivity decreases rapidly. The superconductivity is observed with T_C=10.4 K defined as the midpoint of the resistive transition. The temperature dependence of the susceptibility [18] is shown in Fig. 1.37(a) having almost the temperature-independent value of $\sim 4.5 \times 10^{-4}$ emu/mol above the superconducting transition temperature. Figure 1.38 shows the result of the ESR measurement [18,45], where the ESR line width is about 60 G with an increasing trend as temperature is lowered.

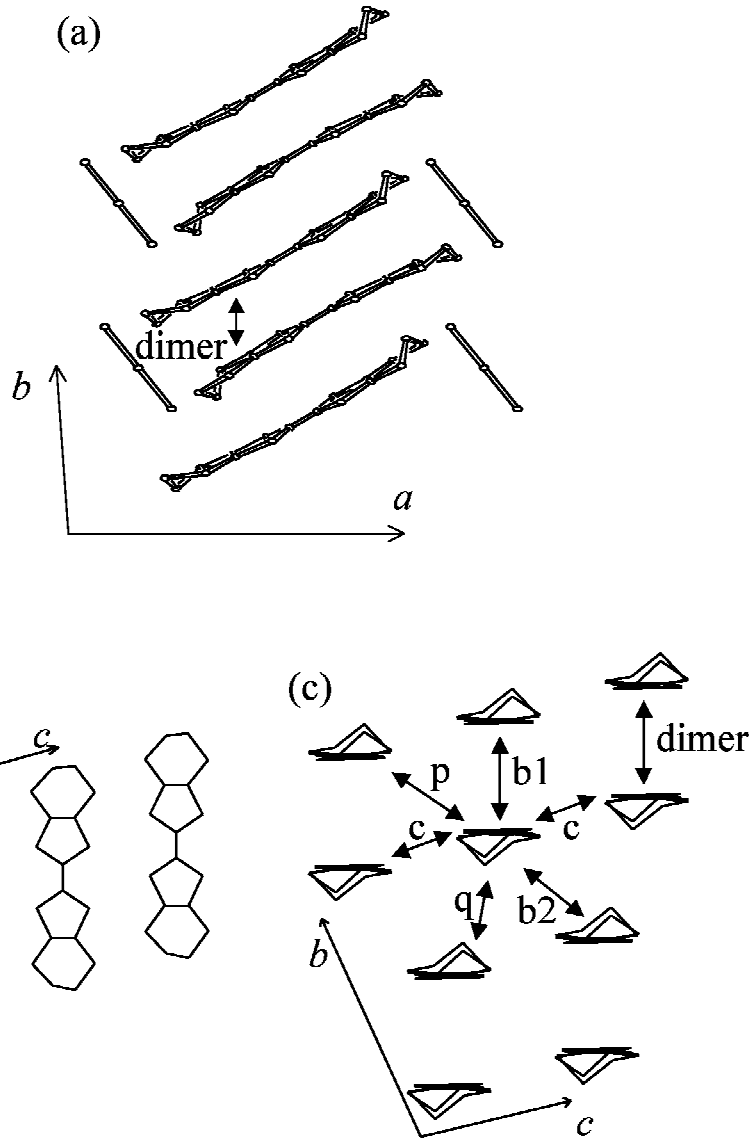

Figure 1.23: Crystal structure of β'-(BEDT-TTF)$_2$X (X=ICl_2, $AuCl_2$). (a) View along the c-axis. (b) View along the direction perpendicular the molecular layer. (c) View along the molecular longest axis indicating the transfer integrals: t_{b1}=27.2 (26.4), t_{b2}=10.0 (10.0), t_p=6.6 (6.5), t_q=–1.6 (–2.0) and t_c=1.6 (2.3)$\times 10^{-2}$ eV for the ICl_2 ($AuCl_2$) salt.

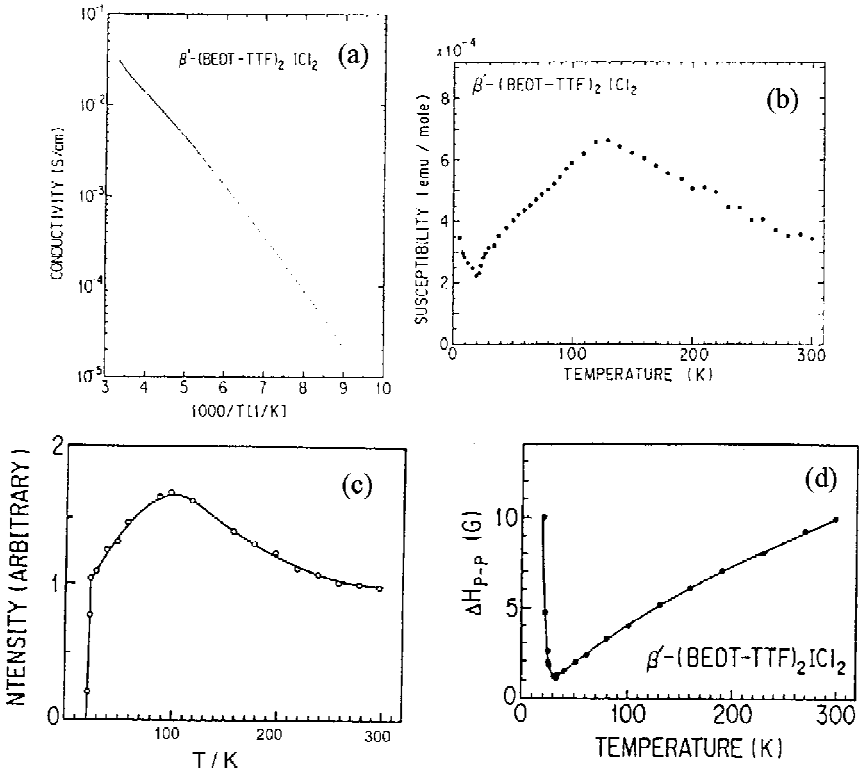

Figure 1.24: Several physical properties of β'-(BEDT-TTF)$_2$ICl$_2$. (a) Temperature dependence of the resistivity [36], (b) the susceptibility [36], (c) the ESR intensity [37], and (d) the ESR line width [37].

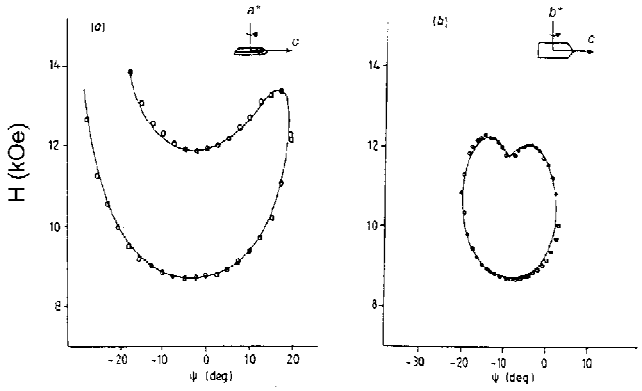

Figure 1.25: Angular dependence of the antiferromagnetic resonance for β'-(BEDT-TTF)$_2$-ICl$_2$around (a) the a*-axis and (b) the b*-axis, respectively [38].

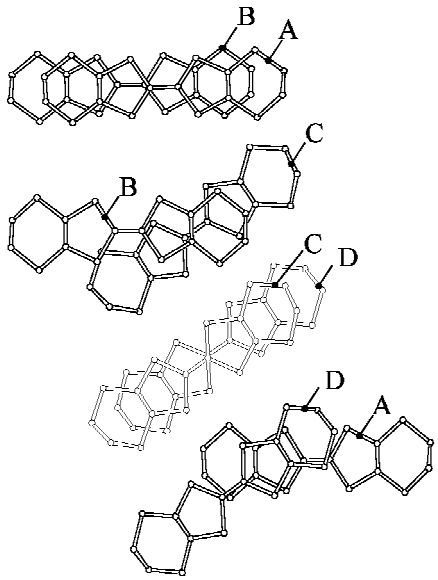

Figure 1.26: View of (BEDT-TTF)$_2$GaCl$_4$ along the molecular stacking direction for (a) A and B molecules, (b) B and C molecules, (c) C and D molecules, and (d) D and A molecules.

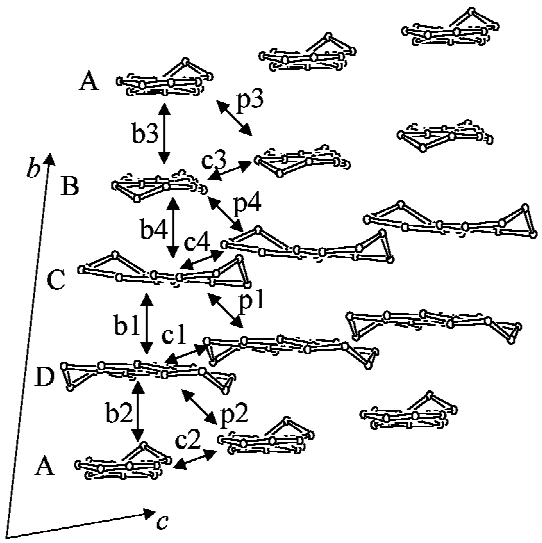

Figure 1.27: Crystal structure of (BEDT-TTF)$_2$GaCl$_4$ from the view along the a-axis. There are four crystallographically independent molecules A, B, C, and D. The transfer integrals are t_{b1}=22.4, t_{b2}=3.69, t_{b3}=26.9, t_{b4}=3.55, t_{c1}=–0.80, t_{c2}=2.86, t_{c3}=2.63, t_{c4}=–4.20, t_{p1}=8.02, t_{p2}=1.96, t_{p3}=5.04, and $t_{p4} = 4.71 \times 10^{-2}$ eV.

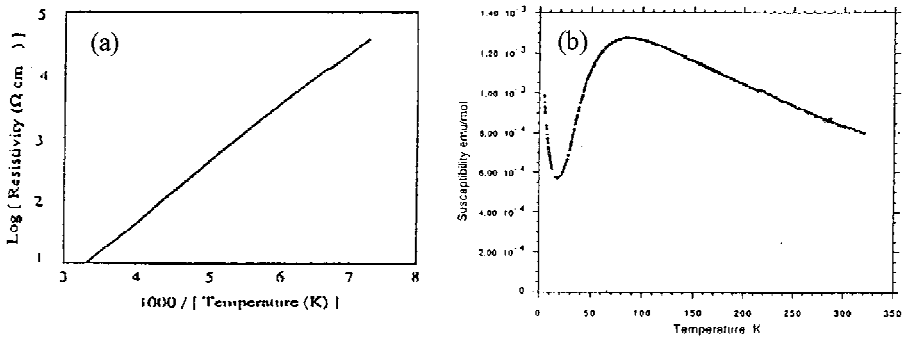

Figure 1.28: (a) Temperature dependence of the resistivity and (b) temperature dependence of the susceptibility for (BEDT-TTF)$_2$GaCl$_4$ [39].

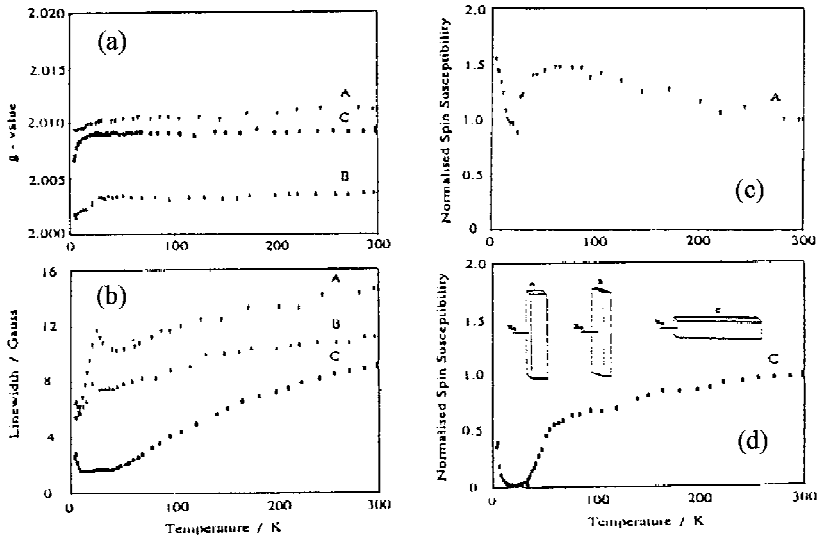

Figure 1.29: The results of the ESR measurement for (BEDT-TTF)$_2$GaCl$_4$ [39]. (a) Temperature dependence of the g-values. (b) Temperature dependence of the ESR line width. (c) and (d) The temperature dependence of the ESR intensity in the field parallel to the A-direction (c) and the B- and C-directions (d).

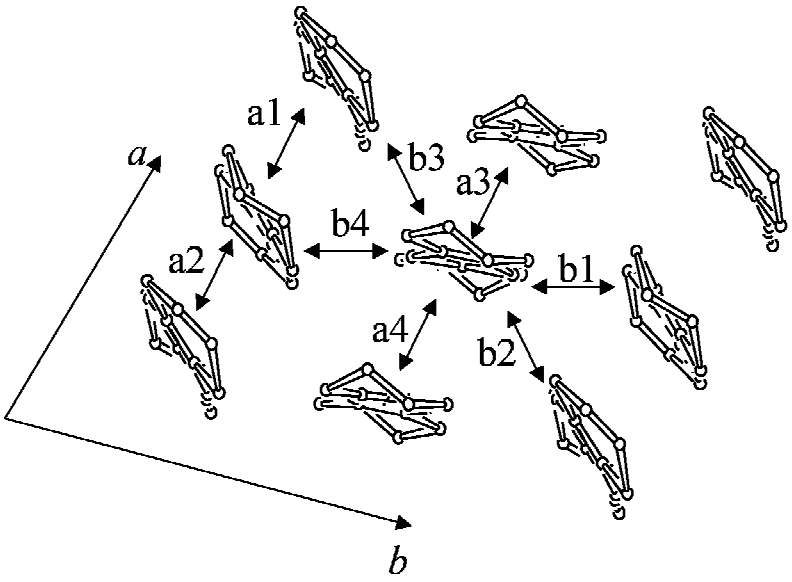

Figure 1.30: Crystal structure of α'-(BEDT-TTF)$_2$IBr$_2$ along the molecular longest axis. The transfer integrals are t_{a1}=4.02, t_{a2}=0.78, t_{a3}=2.30, t_{a4}=1.11, t_{b1}=–7.72, t_{b2}=9.04, t_{b3}=7.16, and t_{b4}=–5.79×10^{-2} eV [41].

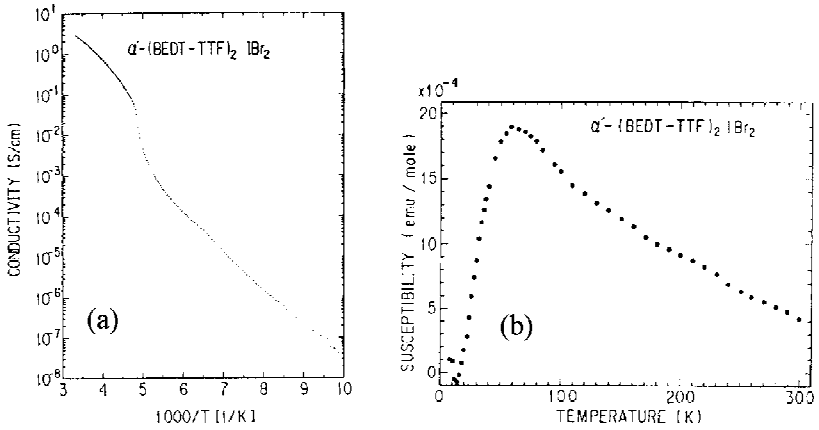

Figure 1.31: (a) Temperature dependence of the resistivity and (b) temperature dependence of the susceptibility for α'-(BEDT-TTF)$_2$IBr$_2$ [36].

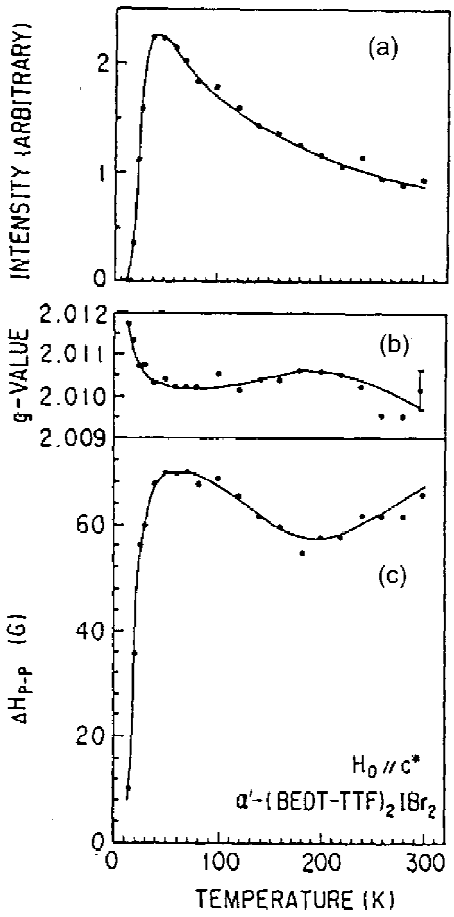

Figure 1.32: Temperature dependence of (a) the ESR intensity, (b) the g-value, and (c) the ESR line width for α'-(BEDT-TTF)$_2$IBr$_2$ [37].

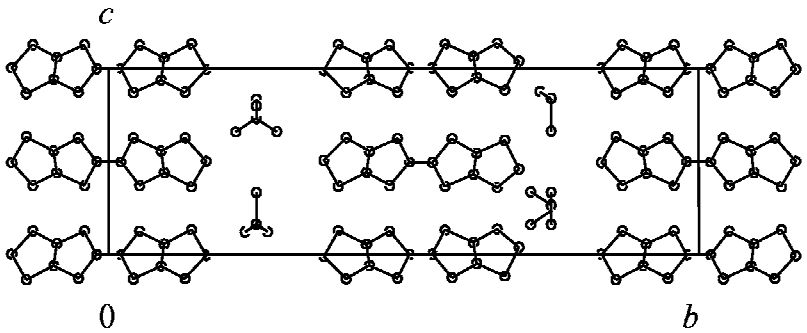

Figure 1.33: Crystal structure of (BMDT-TTF)$_3$ClO$_4$(1,2-dichloroethane) along the donor stacking direction.

Table 1.6: Bond lengths (Å) of the C=C double bond and the C-S single bond in the A and B molecules for (BMDT-TTF)$_3$ClO$_4$(1,2-dichloroethane) [43].

	A(+1)	B(0)
a	1.41	1.35
b	1.73	1.76
c	1.73	1.74
d	1.36	1.32

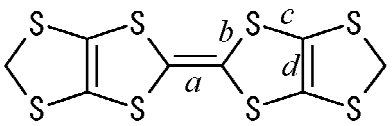

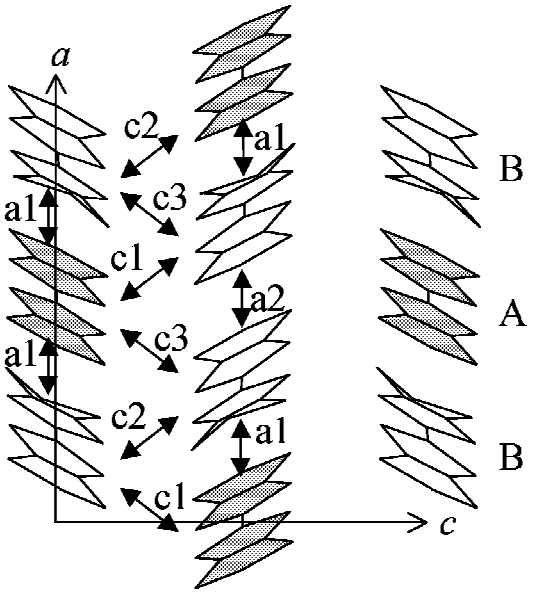

Figure 1.34: Crystal structure of (BMDT-TTF)$_3$ClO$_4$(1,2-dichloroethane) along the *b*-axis having two crystallographically independent molecules A and B. The transfer integrals [43] are $t_{\rm a}1$=–6.22, $t_{\rm a2}$=–5.52, $t_{\rm c1}$=–11.2, $t_{\rm c2}$=11.6, and $t_{\rm c3}$=14.1×10^{-2} eV.

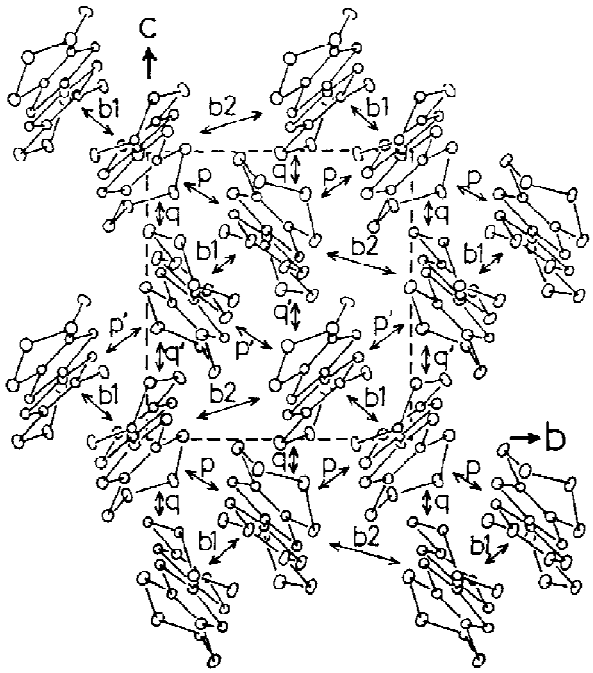

Figure 1.35: Crystal structure of κ-(BEDT-TTF)$_2$Cu(SCN)$_2$ [18]. The values of the transfer integrals are t_{b1}=25.7, t_{b2}=10.5, t_{p}=11.4, $t_{\mathrm{p'}}$=10.0, t_{q}=–1.7, and $t_{\mathrm{q'}}$=–2.9 $\times 10^{-2}$ eV.

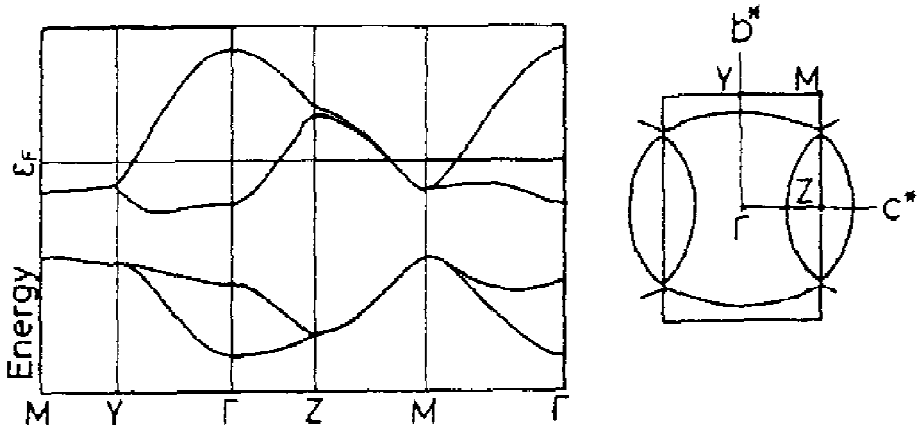

Figure 1.36: Band structure and Fermi surface of κ-(BEDT-TTF)$_2$Cu(SCN)$_2$ [46]. The band width is estimated at $W \sim 0.56$ eV.

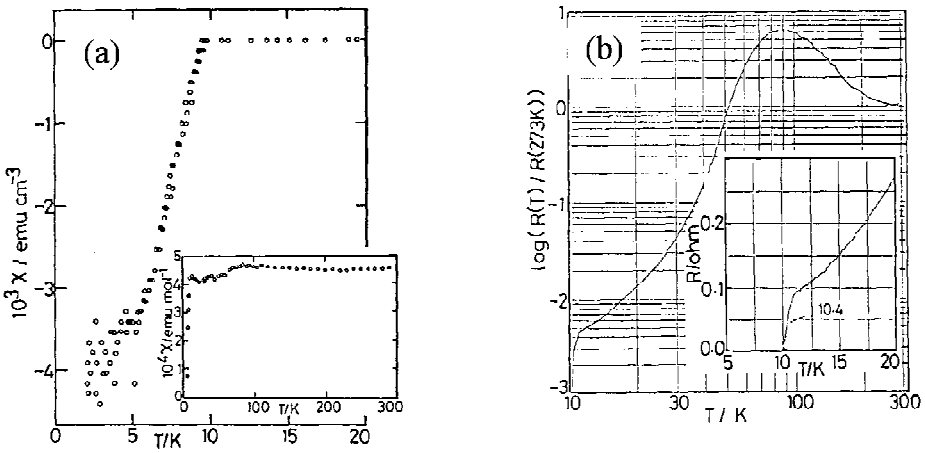

Figure 1.37: (a) Temperature dependence of the susceptibility and (b) temperature dependence of the resistivity for κ-(BEDT-TTF)$_2$Cu(SCN)$_2$ [18].

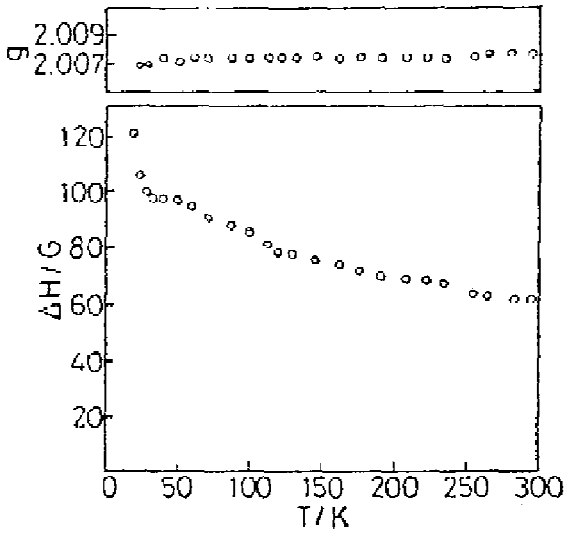

Figure 1.38: The temperature dependence of the g-value and the ESR line width for κ-(BEDT-TTF)$_2$Cu(SCN)$_2$ [18].

Chapter 2

Experimental

2.1 Syntheses and characterization

To investigate the physical properties, single crystals having high quality and sufficiently large size are needed. Several methods [47] for the growth of single crystals proposed: for example, a slow cooling method, an diffusion method, and an evaporation method. We applied an electrochemical method in organic solvent for the syntheses of charge transfer salts. Figure 2.1 shows the apparatus for the electrochemical crystallization, where donor (D; a few mg) and electrolyte (A; a few times larger than donor, ∼10 mg) put in each leg of the apparatus are dissolved in organic solvent (∼15 mg). A small constant current (a few μA) through two platinum electrodes induces the oxidation reaction; $D \rightarrow D^+ + e$. Usually several nucleus of the crystals are formed in a few days, and afterward crystals suitable for experiments are grown in a few weeks.

2.1.1 Preparation of donor and electrolyte

Neutral BEDT-TTF and EDO-TTFBr_2 for syntheses of the single crystal were provided by Saito Laboratory in Kyoto University and by Iyoda Laboratory in Tokyo Metropolitan University, respectively. Neutral BMDT-TTF was purchased from Tokyo Chemical Industry Co., (B1218).

An electrolyte working as an anion is required to have large solubility in organic solvents. Therefore, we used the complex salt consisting of the anion and a cation of $(n\text{-}C_4H_9)_4N^+$ (tetra(buthyl)ammonium cation; TBA^+) which has four good oleophilic groups, giving good solubility.

TBA·ICl_2 was stoichimetrically synthesized [48] from TBA·Cl (white powder) and ICl (brown liquid) in acetic acid solvent at ice-cold temperature. The yellow colored powder after recrystallization was obtained (yield 46 %, m.p. 63–65 ℃). TBA·IBr_2 was synthesized in the same way using TBA·Br and IBr (yield 63 %).

For the synthesis of TBA·$AuCl_2$, TBA·$AuCl_4$ solved in absolute ethanol was reduced by phenylhydrazinium chloride (PhNH·NH_2,HCl) at 40–50 ℃, and after 1 hour the initially

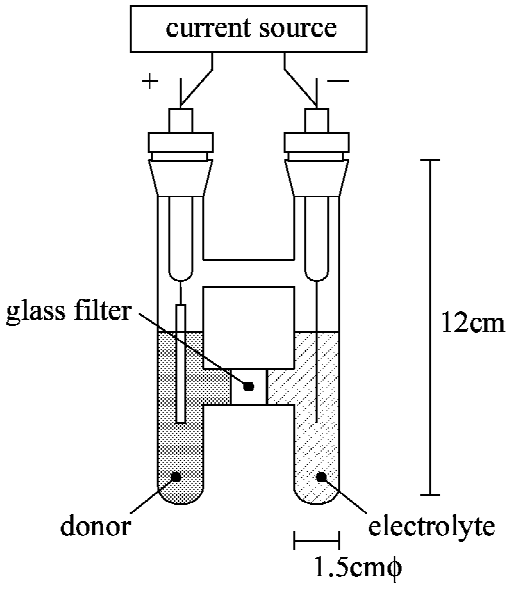

Figure 2.1: Schematic view of the apparatus for an electrochemical method.

yellow solution had become slightly orange. With placed in refrigerator for 10 hours, white crystal was obtained (yield 68 %, m.p. 79–81 ℃).

TBA·AsF_6 (white crystal) was obtained from the reaction between TBA·Br and $KAsF_6$ in distilled water. The recrystallization was carried out using absolute methanol (yield 67 %, m.p. 240–241 ℃).

2.1.2 Electrocrystallization

All the single crystals of our target salts were prepared electrochemically in the conditions summarized in Table 2.1 and the typical sample sizes and the corresponding crystal axes were summarized in Table 2.2.

2.1.3 Crystal structure and band calculation

The cell constants were checked by X-ray diffraction using a Rigaku AFC-7 automated four-circle diffractometer with Mo-Ka radiation for all the compounds which were summarized in Table 2.3. The crystal structures analyses of the structure were carried out for (EDO-$TTFBr_2$)$_2AsF_6$ and (BMDT-TTF)$_3AsF_6$(1,1,2-trichloroethane) by direct methods (SHELXS-86) and least-squares method (SHELXL-93).

The band structures were calculated using a tight-binding approximation with single molecular orbitals (HOMO), which is estimated on the basis of an extended Hückel method (see § 1.6.3).

Table 2.1: Synthetic conditions for the charge transfer salts of our target.

	solvent	donor (mg)	electrolyte (mg)	current (μA)	voltage (V)	days
β'-(BEDT-TTF)$_2$ICl$_2$[a]	THF	9	158	0.5	0.5	14
β'-(BEDT-TTF)$_2$AuCl$_2$[b]	THF	6	33	1	6	4
(BEDT-TTF)$_2$GaCl$_4$[c]	DCE	12	41	1	1	6
α'-(BEDT-TTF)$_2$IBr$_2$[d]	THF	9	110	0.3	0.2	8
(EDO-TTFBr$_2$)$_2$AsF$_6$	TCE	4	32	1.5	6	4
MT$_3$ClO$_4$DCE[e]	DCE	2	100	0.25	0.3	4
MT$_3$AsF$_6$TCE	TCE	3.6	40	0.5	1.5	5

[a]Ref. [34].
[b]Refs. [21, 35].
[c]Ref. [39].
[d]Ref. [49].
[e]Ref. [42].

Table 2.2: Typical size of the crystals and the corresponding directions.

	size (mm^3)	corresponding axes
β'-(BEDT-TTF)$_2$ICl$_2$	1.2×0.4×0.1	c, b*, a*
β'-(BEDT-TTF)$_2$AuCl$_2$	0.8×0.2×0.1	c, b*, a*
(BEDT-TTF)$_2$GaCl$_4$	0.8×0.1×0.05	c, b*, a*
α'-(BEDT-TTF)$_2$IBr$_2$	1×0.8×0.01	a, b, c*
(EDO-TTFBr$_2$)$_2$AsF$_6$	3×0.4×0.1	c, b*, a*
MT$_3$ClO$_4$DCE	1×1(× ∼0.005)	a, c, (b)very thin
MT$_3$AsF$_6$TCE	1×1(× ∼0.005)	a, c, (b)very thin

Table 2.3: Cell constants. The space group is $P\bar{1}$ for all the 2:1 salts, and $Pnma$ for the 3:1 salts, respectively.

	a (Å)	b (Å)	c (Å)	α (°)	β (°)	γ(°)	V (Å^3)	Z
β'-(BEDT-TTF)$_2$ICl$_2$[a]	12.937	9.778	6.636	98.59	100.98	87.19	814.6	1
β'-(BEDT-TTF)$_2$AuCl$_2$[b]	12.766	9.763	6.640	99.47	100.58	86.4	801.2	1
(BEDT-TTF)$_2$GaCl$_4$[c]	31.911	16.580	6.645	98.15	85.60	90.55	3470	4
α'-(BEDT-TTF)$_2$IBr$_2$[d]	8.905	12.031	16.403	85.16	88.66	70.86	1652	2
(EDO-TTFBr$_2$)$_2$AsF$_6$	7.099	14.844	7.019	93.16	106.07	79.81	699.9	2
MT$_3$ClO$_4$DCE[e]	12.728	33.302	10.204	90	90	90	4325	4
MT$_3$AsF$_6$TCE	12.65	35.35	10.310	90	90	90	4609	4

[a]Ref. [33].
[b]Ref. [21].
[c]Ref. [39].
[d]Ref. [40].
[e]Ref. [42].

2.2 Measurements

2.2.1 Susceptibility and magnetization

The susceptibilities were measured using a SQUID magnetometer (Quantum Design, MPMS-5) with the maximum magnetic field of 5.5 Tesla in the temperature ranging 1.7–400 K. About 10 to 20 single crystals (several mg) were arranged in the same directions using Apiezon N grease. An observed susceptibility is generally considered to be the summation of several contributions,

$$\chi_0 = \chi_{\rm spin} + \chi_{\rm dia} + \chi_{\rm impurity}, \tag{2.1}$$

where χ_0 is the net susceptibility obtained from the ratio of the magnetization and the applied field, $\chi_{\rm spin}$ is the spin susceptibility, $\chi_{\rm dia}$ is the core diamagnetic contribution, and $\chi_{\rm impurity}$ is a fractional Curie-tail at low temperature coming from magnetic impurities. Thus, the spin susceptibilities were obtained after the subtraction of the Pascal's diamagnetic core contribution ($\chi_{\rm dia}$), and if any, an S=1/2 Curie term associated with a trace of magnetic impurities ($\chi_{\rm impurity}$) as summarized in Table 2.4.

2.2.2 ESR measurement

ESR measurements were carried out with a single crystal, using an X-band ESR spectrometer (JEOL JES-TE200 having a microwave power of 0.1 μW–200 mW and the maximum electromagnetic field of ∼1300 mT) with a He cryostat (Oxford ESR910) in the temperature range 4.2–300 K.

2.2.3 Resistivity

The resistivity measurements were carried out using a standard four terminal method. Four gold wires of 25 $\mu\phi$ were attached to a crystal as the electrical terminals with carbon paste (DOTITE XC-12, Fujikura Kasei Inc.) or gold paste (Tokuriki Kagaku Inc.). For

Table 2.4: Core diamagnetic susceptibilities and Curie contribution of impurities. The β'-salts contained no detectable amount of magnetic impurities.

	$\chi_{\rm dia}$ ($\times 10^{-4}$ emu/mol)	$\chi_{\rm impurity}$ (%)
β'-(BEDT-TTF)$_2$ICl$_2$	–4.99	–
β'-(BEDT-TTF)$_2$AuCl$_2$	–5.06	–
(BEDT-TTF)$_2$GaCl$_4$	–5.26	1.1
α'-(BEDT-TTF)$_2$IBr$_2$	–5.25	0.54
(EDO-TTFBr$_2$)$_2$AsF$_6$	–4.99	0.4
MT$_3$ClO$_4$DCE	–6.34	2.0
MT$_3$AsF$_6$TCE	–7.17	1.6

β'-(BEDT-TTF)$_2$ICl$_2$, we measured the anisotropy of the resistivity on the *bc*-plane by the Montgomery method [50] to investigate the electric dimensionality of the β'-salts.

2.2.4 Thermoelectric power

We briefly explain the experimental side of the thermoelectric power. Heating at one end of a sample, the temperature difference (ΔT) between the hot and cold ends generates the voltage difference (ΔV). The thermoelectric power S is defined as the ratio between ΔV and ΔT,

$$S = \frac{\Delta V}{\Delta T}. \tag{2.2}$$

Figure 2.2 shows a measurement technique for the thermoelectric power, where the edge of a sample is connected to two thermocouples consisting of two metals A and B with the thermoelectric powers S_{A} and S_{B}, respectively. Here, the voltages V_{A} and V_{B} shown in Fig. 2.2 are described as

$$V_{\mathrm{A}} = -S_{\mathrm{A}}\Delta T + S\Delta T \quad \text{and} \tag{2.3}$$

$$V_{\mathrm{B}} = -S_{\mathrm{B}}\Delta T + S\Delta T. \tag{2.4}$$

Equations (2.2), (2.3), and (2.4) give the thermoelectric power of the sample:

$$S = -\frac{S_{\mathrm{A}} - S_{\mathrm{B}}}{V_{\mathrm{A}} - V_{\mathrm{B}}}V_{\mathrm{B}} + S_{\mathrm{B}}, \tag{2.5}$$

which indicates that thermoelectric power of the sample is obtained from the measurements of the two voltages.

Figure 2.3 shows the setup designed for the measurement of the thermoelectric power using a sample with a size of below ~1 mm. Two pairs of 0.076 ϕmm chromel-constantan thermocouples were used to detect the temperature and voltage difference, and a strain gauge or 0.05 ϕmm manganin line (20–30 -) was utilized as a heater to make a temperature gradient. The sample was connected to the two terminals of the thermocouples using carbon paste. Figure 2.4 shows a typical heating curve for one measurement of the thermoelectric power of a standard sample lead at a temperature, where there is a small offset voltage of about 0.5 μV. When the two-terminal resistivity of the sample is higher than ~10 k- , this offset voltage got too large to measure the thermoelectric power. Ordinary semiconductive samples have large thermoelectric power, while the resistivity increases as temperature is lowered, and thus the measurement of the thermoelectric power is difficult in the low temperature region.

2.2.5 Transport measurements under pressure

The resistivities under pressure were measured using a clamp-type cell made of CuBe alloy, which was designed for the maximum pressure of ~10–15 kbar. Figure 2.5 shows the

schematic cross section of the clamp-type cell and the apparatus for the resistivity measurement with the four-terminal method. For the setting of the measurement, a pressure medium of Daphne 7243 oil was filled in the Teflon jacket ($5\phi \times 30$ mm) located in the center of the cell, where a hydrostatic pressure was applied. The pressure was detected from the resistivity of a manganin line ($\sim$ 100-), which was set simultaneously and clamped at room temperature. The pressure dependence of the resistivities was measured at room temperature and then the temperature was changed under the several pressures of 1 bar (ambient pressure), 7.5 and 12 kbar for β'-(BEDT-TTF)$_2$ICl$_2$, of 1 bar and 8.4 kbar for α'-(BEDT-TTF)$_2$IBr$_2$, of 1 bar and 9.0 kbar for (EDO-TTFBr$_2$)$_2$AsF$_6$, and of 1 bar, 3.5, 6.6, 9.6 and 11.4 kbar for (BMDT-TTF)$_3$AsF$_6$(1,1,2-trichloroethane), respectively.

The measurement of the thermoelectric power under pressure is not so popular compared with that of resistivity, because of the experimental difficulty to measure the temperature difference between the two-terminal of a sample under pressure accurately. The pressure dependence of the thermocouples or temperature dependence under pressure has not been known yet. However, if the pressure dependence of the thermocouple is sufficiently smaller than that of the sample, the sufficiently quantitative experiments is possible. Fortunately, our semiconductive target compounds are expected to have a large thermoelectric power, and moreover the organic molecular compounds are highly sensitive compared with the thermocouples made of inorganic metals. We confirmed the reliability of the experimental data by means of measuring the thermoelectric power of lead under pressure since lead is generally utilized for the calibration of thermocouples. The detected difference in the thermoelectric power between under helium gas atmosphere of 20 Torr and pressure medium of 8 kbar was only below $\sim$1 μV/K. Therefore, we could measure the thermoelectric power under pressure when the absolute value of the thermoelectric power was sufficiently larger than 1 μV/K. We measured the pressure dependence of the thermoelectric power at room temperature, and afterward carried out the measurement of the temperature dependence for β'-(BEDT-TTF)$_2$ICl$_2$ at 4 kbar and (BMDT-TTF)$_3$AsF$_6$(1,1,2-trichloroethane) at 9 kbar.

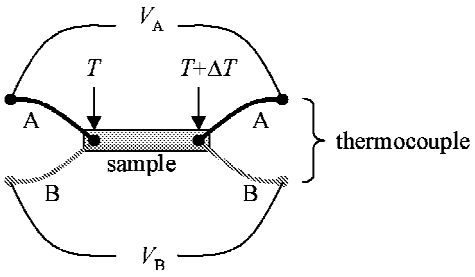

Figure 2.2: A setup for the thermoelectric power measurement. Two pairs of lines A and B are the thermocouples.

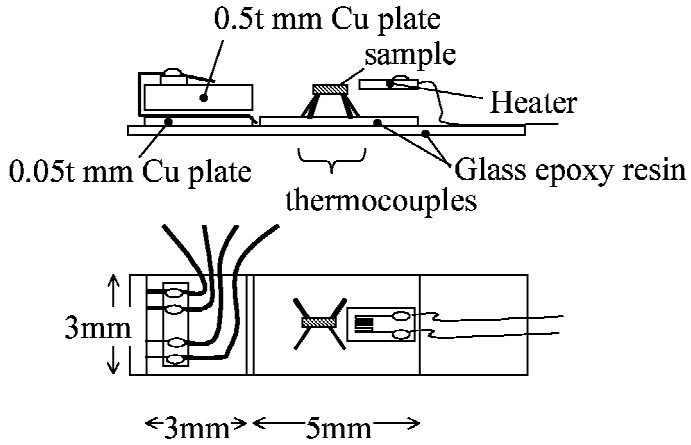

Figure 2.3: Apparatus for the thermoelectric power. The thermocouples settled in the center of the sample stage go through the space between the two Cu plates working as thermal anchor. The sample is attached to the two terminals of the thermocouples using carbon paste.

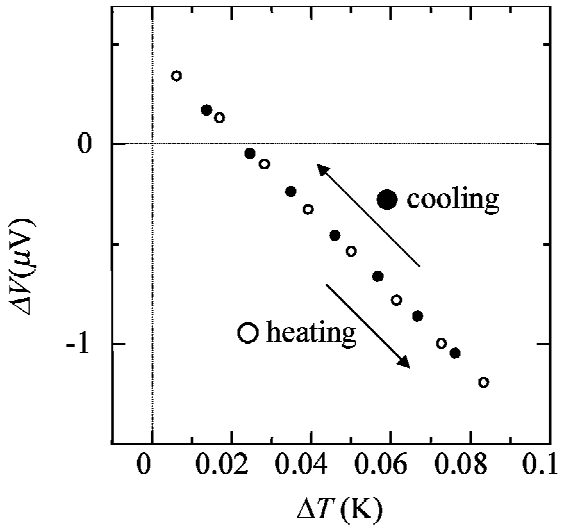

Figure 2.4: Typical heating-cooling curve for the thermoelectric power of lead (standard sample) at 292 K under helium atmosphere of 20 Torr. ΔV is the voltage between two terminals of thermocouples through the sample.

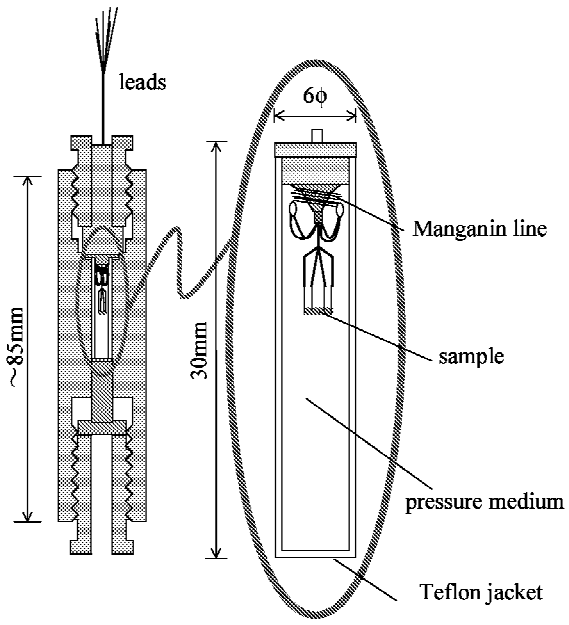

Figure 2.5: Cross section of the clamp-type cell for measurement under pressure made of CuBe alloy (left side) and the detail of the apparatus for the resistivity measurement (right side).

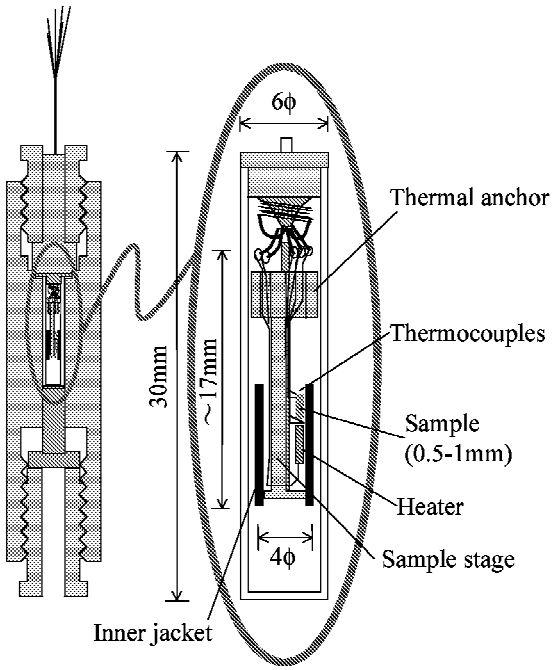

Figure 2.6: Schematic view of the apparatus for the thermoelectric power measurement under pressure (right side).

Chapter 3

Results

We here explain the results of the band calculation, magnetic susceptibility, ESR, resistivity, and thermoelectric power for each salt. The band calculation of $(BMDT\text{-}TTF)_3ClO_4$(1,2-dichloroethane) is not carried out since this salt indicates the charge disproportionation.

3.1 β'-(BEDT-TTF)$_2$X (X=ICl_2, $AuCl_2$)

3.1.1 Band calculation

We carried out a band calculation for β'-$(BEDT\text{-}TTF)_2ICl_2$ to check the reported result [33]. The band structure is shown in Fig. 3.1. Our result is the same with the reported one [33] and that of β'-$(BEDT\text{-}TTF)_2AuCl_2$ [21] shown in Fig. 1.20. Strong dimerization of these salts gives the band split in the electronic structure, and the band width of the upper band having the Fermi surface is about 0.28 eV. The Fermi surface indicates the one-dimensional electronic state along the b*-axis.

3.1.2 Susceptibility

The temperature dependence of the susceptibilities [52, 53] is shown in Figs. 3.2 and 3.3 for the ICl_2 and $AuCl_2$ salts, respectively. The susceptibilities, whose room temperature values are 0.96×10^{-3} emu/mol, have a broad maximum at $T_{\max} \approx 100$ K for both salts, which are characteristic of short-range order of a low-dimensional antiferromagnet. There is no observable difference in the data above $T_{\max}$ between the two salts, and the fitting to the Curie-Weiss law above 250 K gives a Weiss constant of Θ=–140±20 K and a Curie constant of C=0.42±0.02 emu/mol K corresponding to the Bohr magneton of p=1.83±0.05 per formula unit for both salts, while p=1.737–1.740 is expected for an S=1/2 spin with the observed g-value g=2.006–2.009 (see § 3.1.3). The present results of the susceptibility for the ICl_2 salt are qualitatively consistent with the previous reports [34,36], although the absolute values are not in good quantitative agreement with each other. The data of Ref. [34] are supposed to contain a large error in the absolute value because of the estimation carried out

using ESR measurement, while those of Ref. [36] are not treated with the correction of the core diamagnetic susceptibility.

The susceptibilities show discontinuous changes at Néel temperature T_N=22 K and 28 K for the ICl_2 and $AuCl_2$ salts, respectively, indicating the onsets of three-dimensional long-range orderings. From the appearance of anisotropy in the susceptibilities below T_N, we obtain information on the spin easy-axis in the antiferromagnetic ordered state. The susceptibility in the field parallel to the c-axis approaches zero as the temperature decreases, suggesting that the easy-axis is oriented to the c-axis. The magnetizations of the two salts at 2 K are shown in Fig. 3.4. In the magnetization curves, spin flop transitions are observed at H_{sf}=11 kOe for both salts when the external field is applied parallel to the c-axis, in good agreement with the anisotropy in the susceptibilities.

3.1.3 ESR

The ESR line shape is a Lorentzian-type for the ICl_2 salt. The g-values at room temperature are estimated at 2.009, 2.007, and 2.006 in the field parallel to the a*-, b*-, and c-axes, respectively. The temperature dependence of the line width shown in Fig.3.5 for the ICl_2 salt is consistent with the previous reports [34, 37]. The line width becomes narrow as the temperature decreases accompanied with an upturn below 30 K which becomes divergent as the temperature approaches T_N=22 K. The g-value is shifted in the critical temperature region between T_N and ∼30 K as shown in Fig. 3.6, which is consistent with the anisotropy of the susceptibility below T_N, that is, the field parallel or perpendicular to the easy-axis gives the reduction or increases of the g-value, respectively. We suggest that this g-shift reflects the short-range ordering effect in low-dimensional antiferromagnetic systems.

3.1.4 Resistivity

The temperature dependence of the resistivity for the ICl_2 salt is shown in Fig. 3.7. The resistivity, whose room temperature value is ∼20 - cm, increases exponentially as temperature decreases, which is well explained as a semiconductor having an activation energy of 0.10±0.01 eV. In this salt, the crystal growth direction does not correspond with the direction of the strongest inter-molecular interaction expected from the crystal structure. Thus, for characterizing the dimensionality of this salt, the ratio of the resistivity along the b*-axis to that along the c-axis (longest crystal-growing direction) is measured using the Montgomery method [45], which is estimated at $\rho_{b*}/\rho_c \approx 0.8$ independent of temperature. This small anisotropy between the b*- and c-axes indicates the two-dimensionality in the inter-molecular network on the bc-plane.

The pressure dependence of the resistivity at room temperature up to 12 kbar is shown in Fig. 3.8, where the resistivity monotonously decreases down to ∼5 - cm at 12 kbar with a pressure increase. The temperature dependence of the resistivities measured at pressures of

7.5 and 12 kbar is shown in Fig. 3.7. It suggests semiconductivity even at 12 kbar with an activation energy $E_a \approx 0.07$ eV (above 100 K).

3.1.5 Thermoelectric power

The temperature dependence of the thermoelectric power for the ICl_2 salt at ambient pressure (1 bar) is shown in Fig. 3.9(a). The large positive thermoelectric power with the room temperature value of $\sim$+400 μV/K reflects the dominant role of hole-type carriers in the semiconducting state. The thermoelectric power below $\sim$250 K could not be measured experimentally because of the high resistance $\sim$10 k- between the two-terminals of the sample. The $1/T$ behavior shown in Fig. 3.9(a) is considered to reflect semiconductivity. Figure 3.9(b) shows the pressure dependence of the thermoelectric power at room temperature, which reveals a decrease down to $\sim$300 μV/K as the pressure is elevated up to 6 kbar. In the temperature dependence under a pressure of 4 kbar, there is no large difference form the data at 1 bar.

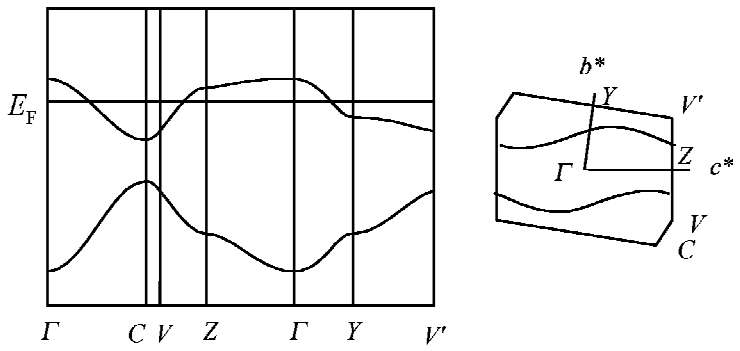

Figure 3.1: The band structure and the Fermi surface for β'-(BEDT-TTF)$_2$ICl$_2$. The strong dimerization makes the band split into two sub-bands resulting the effective half-filled electronic state. The band width of the upper band having the Fermi surface is about 0.28 eV.

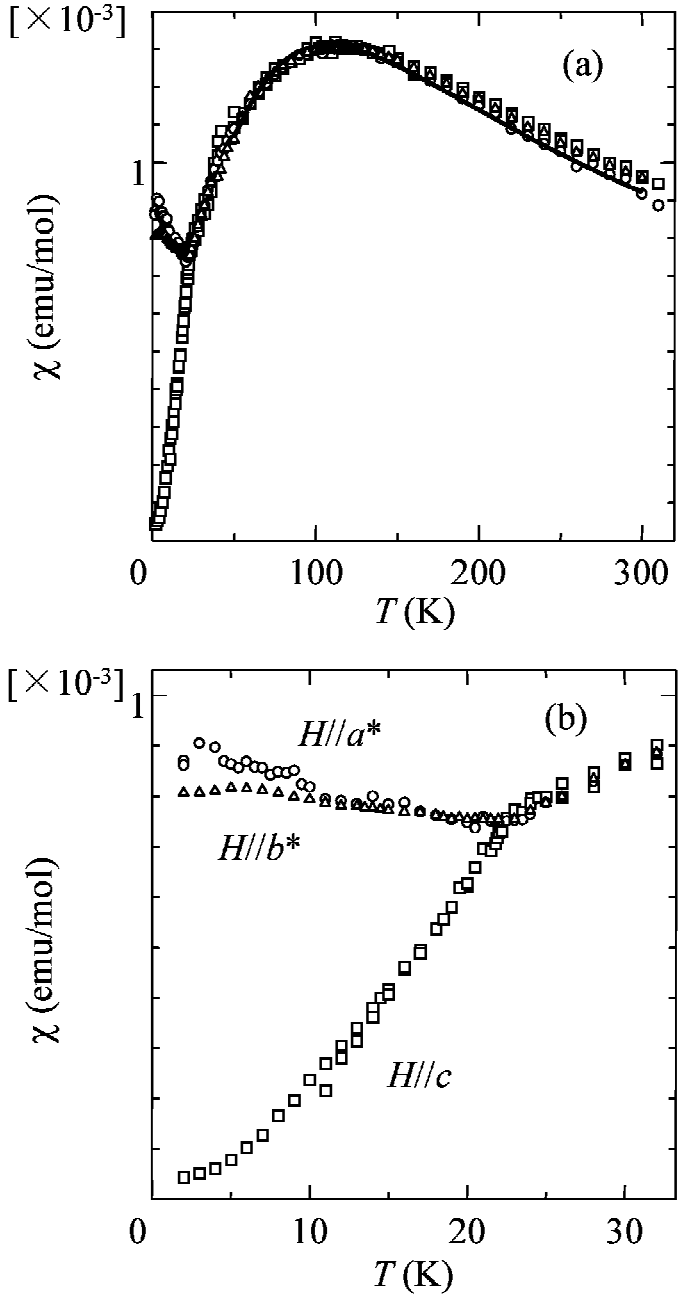

Figure 3.2: Temperature dependence of the susceptibility for β'-(BEDT-TTF)$_2$ICl$_2$. (a)The solid curve denotes the fitting to the S=1/2 two-dimensional square-lattice Heisenberg antiferromagnet model with J=–59 K. (b)Details at low temperatures with the Néel temperature of 22 K.

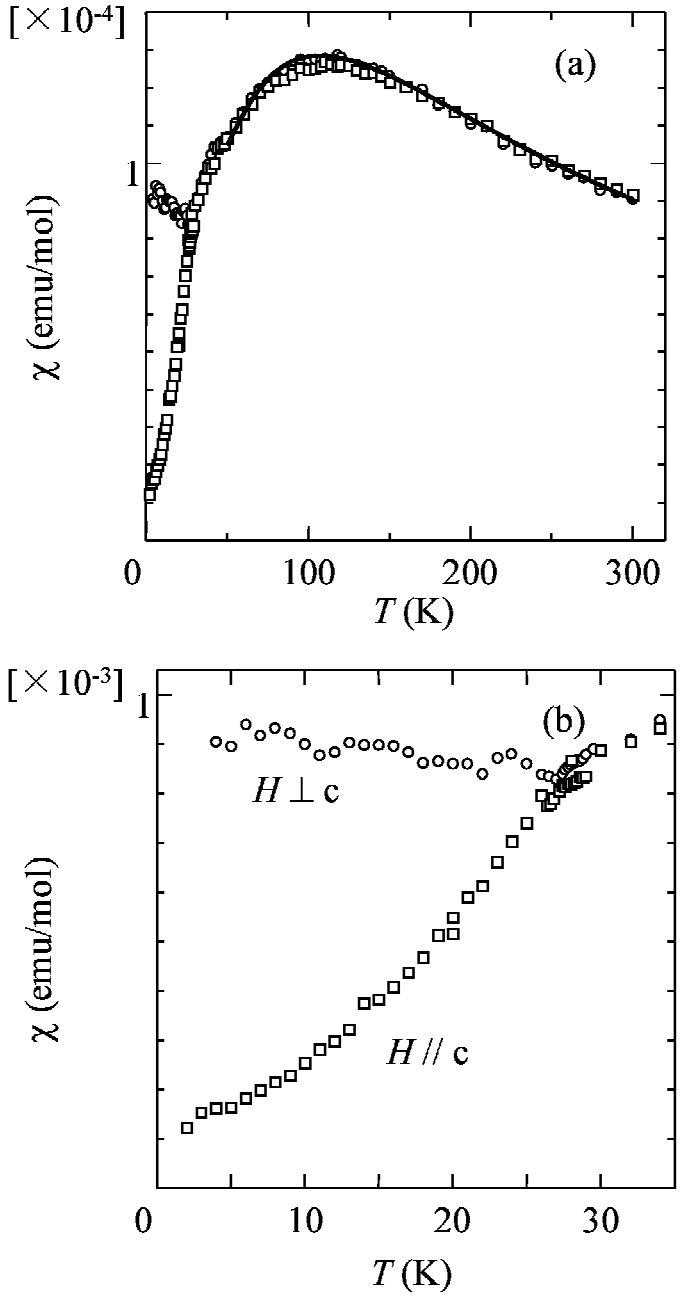

Figure 3.3: Temperature dependence of the susceptibility for β'-(BEDT-TTF)$_2$AuCl$_2$. (a)The solid curve denotes the fitting to the S=1/2 two-dimensional square-lattice Heisenberg antiferromagnet model with J=–59 K. (b)Details at low temperatures with the Néel temperature of 28 K.

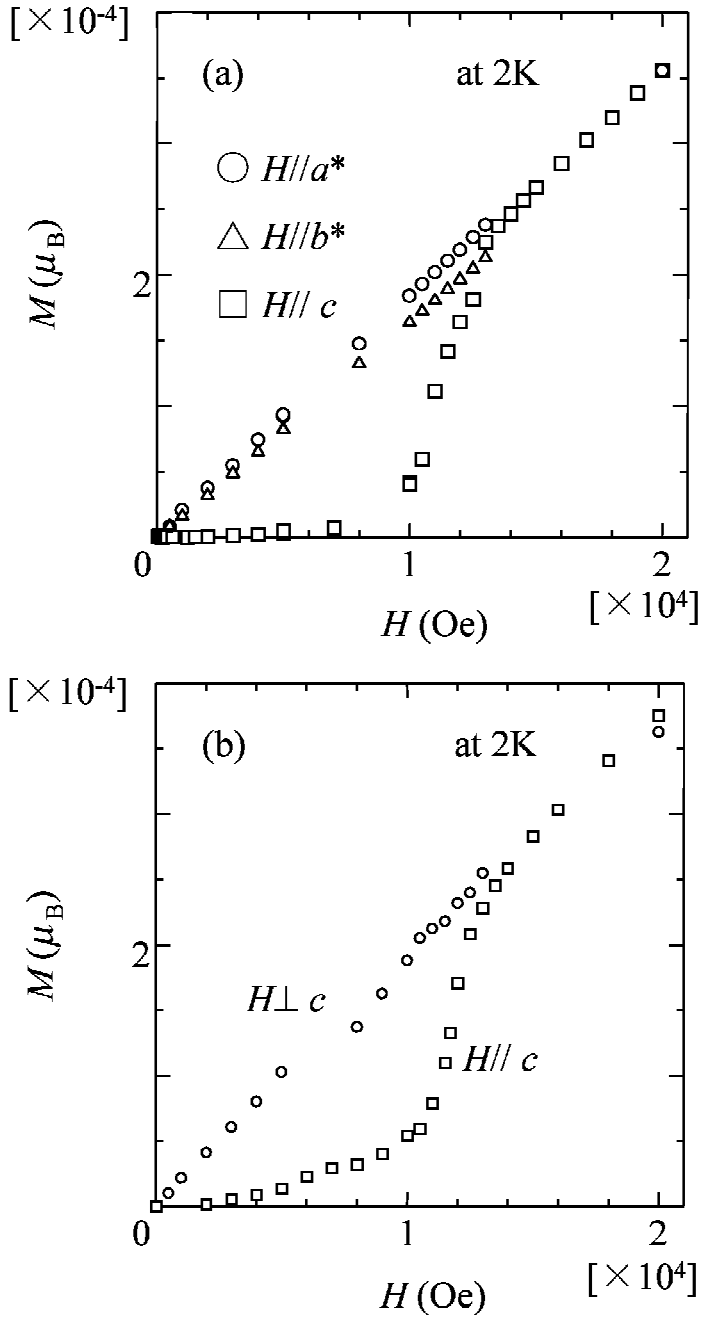

Figure 3.4: Magnetization curves at 2 K of the β'-(BEDT-TTF)$_2$X where (a) X=ICl_2 and (b) X=$AuCl_2$.

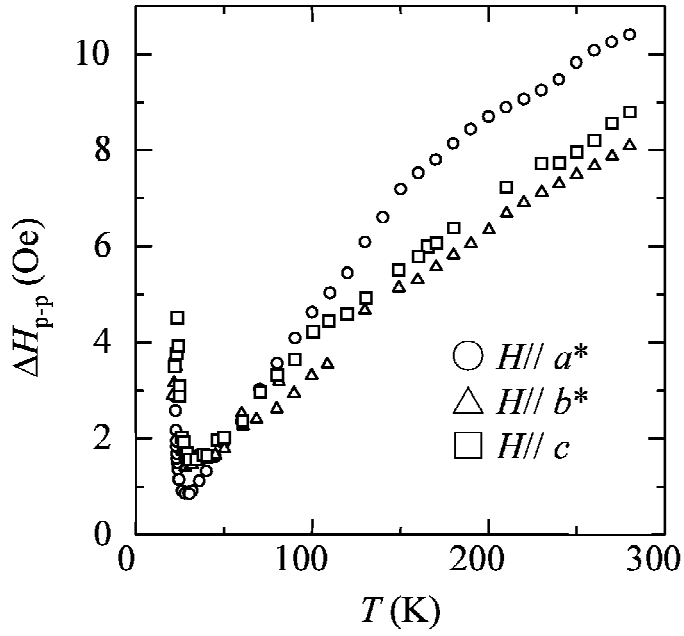

Figure 3.5: Temperature dependence of the ESR line width for β'-(BEDT-TTF)$_2$ICl$_2$.

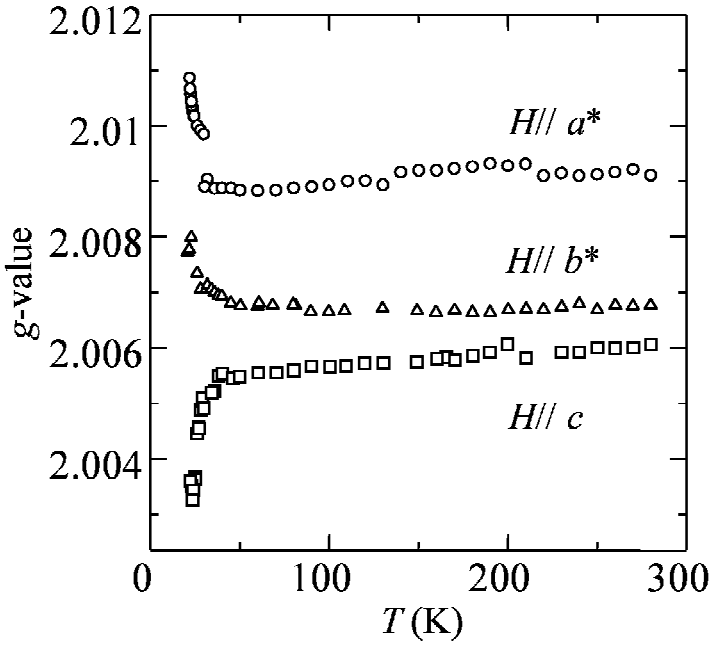

Figure 3.6: Temperature dependence of the g-values for β'-(BEDT-TTF)$_2$ICl$_2$.

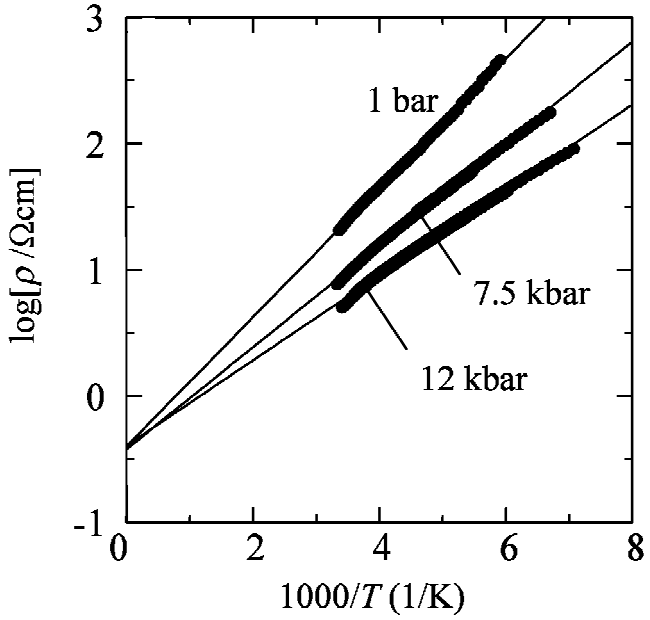

Figure 3.7: Temperature dependence of the resistivities for β'-(BEDT-TTF)$_2$ICl$_2$ under pressure with Arrhenius fitting (solid lines) of the activation energy E_a=0.10 eV (1 bar), 0.08 eV (7.5 kbar), and 0.07 eV (12 kbar).

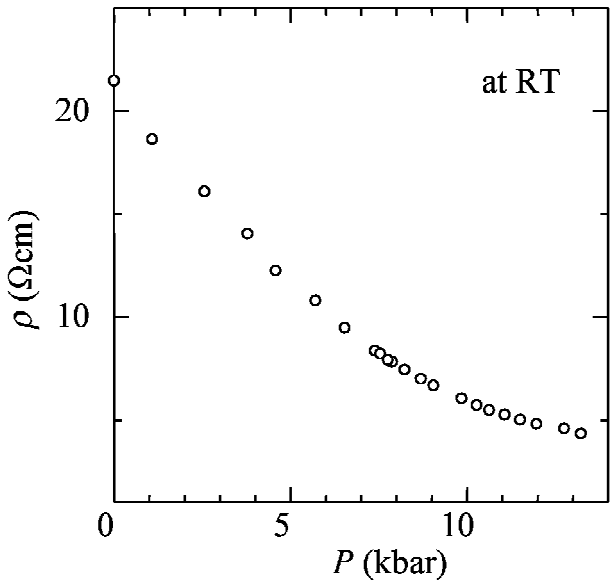

Figure 3.8: Pressure dependence of the resistivities for β'-(BEDT-TTF)$_2$ICl$_2$ at room temperature.

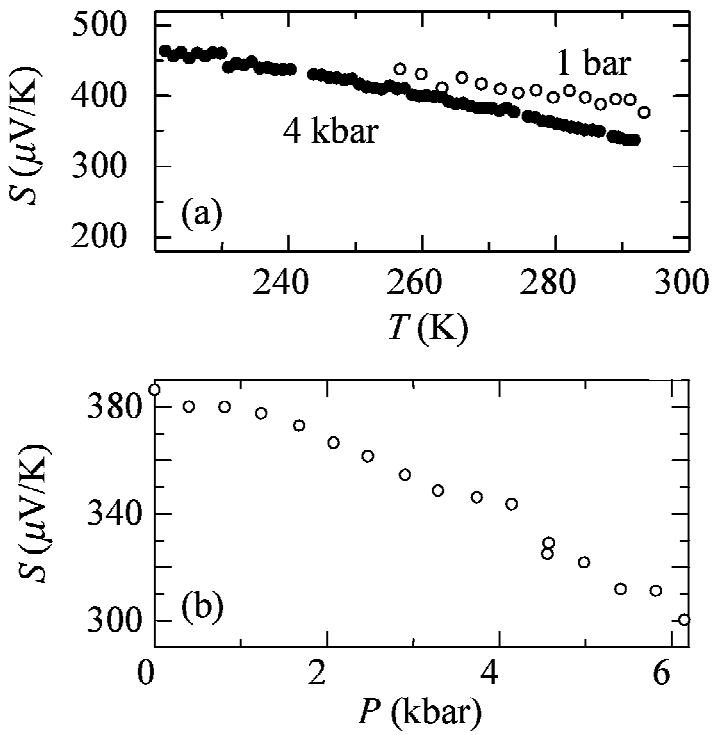

Figure 3.9: (a)Temperature dependence of the thermoelectric power for β'-(BEDT-TTF)$_2$-ICl$_2$ at 1 bar in He gas atmosphere (open circle) and 4 kbar in the pressure medium (closed circles). (b)Pressure dependence of the thermoelectric power for β'-(BEDT-TTF)$_2$ICl$_2$ at room temperature.

3.2 (BEDT-TTF)$_2$GaCl$_4$

3.2.1 Band calculation

The band structure and the Fermi surface is shown in Fig. 3.10. There are four bands corresponding to the four donor molecules in a unit cell. The donor molecules strongly dimerized make the band structure to be the effective half-filled electronic state. The band width of the upper band is about 0.30 eV. The Fermi surface shows a two-dimensional feature in the *bc*-plane.

3.2.2 Susceptibility

The susceptibility in the field parallel to the *c*-axis is shown in Fig. 3.11. The fitting to the Curie-Weiss law gives a Weiss constant of Θ=–110 K±20 K and a Curie constant of C=0.40±0.02 emu/mol K (corresponding to the magnetic moment of 1.79±0.05 μ_B per formula unit) above 200 K. The susceptibility shows a broad maximum around 90 K, and then below about 60 K, it approaches zero as $T \rightarrow 0$, which is contradictory to the reported result [39] where it is extrapolated to a finite value ($\sim 4\times10^{-4}$ emu/mol) at 0 K. The presence of magnetic impurities might be considered to mislead to the wrong result in the previous report. No spin flop transition is observed in the magnetization at 2 K up to 55 kOe. Thus, the magnetic system is suggested to be stabilized in a spin-singlet state at T=0 K.

3.2.3 Resistivity and thermoelectric power

The temperature dependence of the resistivity shown in Fig. 3.12 is semiconductive with the resistivity at room temperature of ∼10 - cm. The activation energy is 0.19±0.01 eV, which is consistent with the reported result (0.2 eV) [39]. Figure 3.13 shows the pressure dependence of the resistivity at room temperature. The resistivity decreases down to 3 - cm at 10 kbar as pressure is elevated. Figure 3.14(a) shows the temperature dependence of the thermoelectric power. The room temperature value of about 100 μV/K, which is in the similar order to β'-(BEDT-TTF)$_2$ICl$_2$, increases as the temperature decreases.

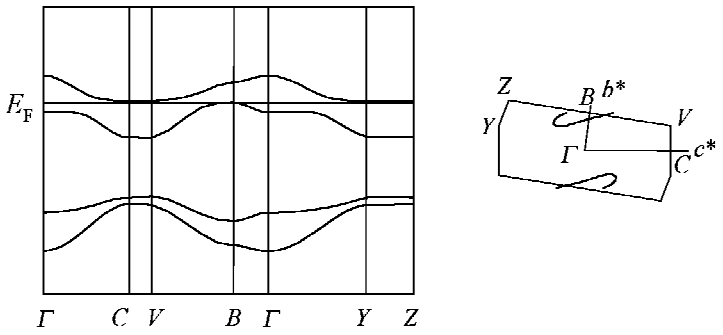

Figure 3.10: The band structure and the Fermi surface for (BEDT-TTF)$_2$GaCl$_4$. There are four bands corresponding the four donor moelcules in a unit cell, which are strongly dimerized. This dimerization makes the band structure to be split (effective half-filled electronic state). The band width of the upper band is about 0.30 eV.

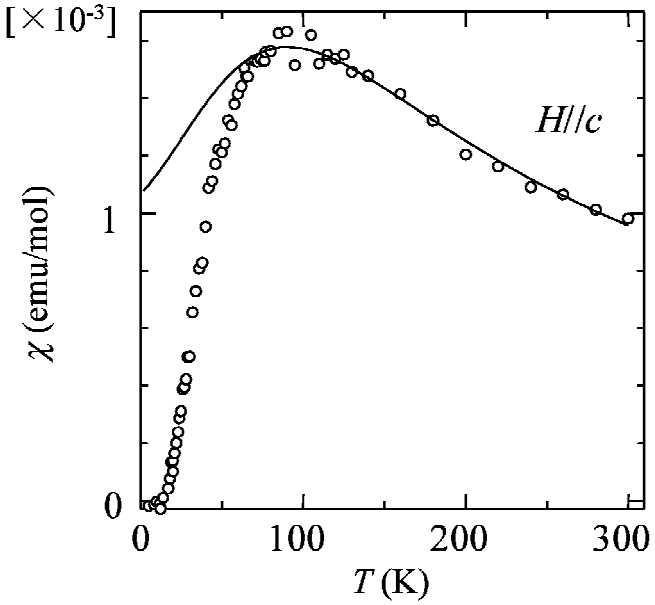

Figure 3.11: Temperature dependence of the susceptibility for (BEDT-TTF)$_2$GaCl$_4$. The solid curve denotes the fitting to the S=1/2 one-dimensional Heisenberg antiferromagnet model with J=–70 K.

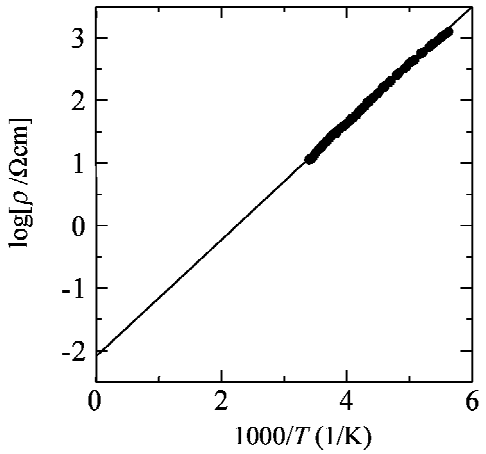

Figure 3.12: Temperature dependence of the resistivity for (BEDT-TTF)$_2$GaCl$_4$. Solid line is the Arrhenius plot with an activation energy of 0.19 eV.

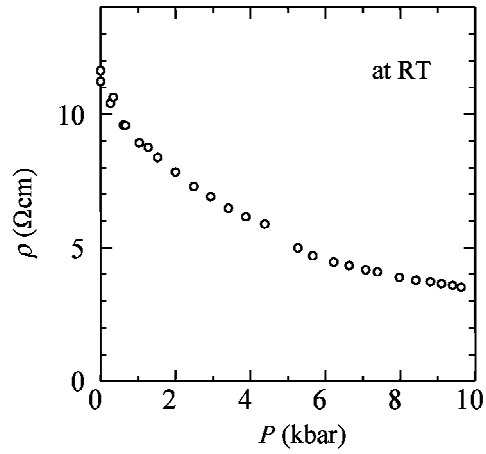

Figure 3.13: Pressure dependence of the resistivity for (BEDT-TTF)$_2$GaCl$_4$ at room temperature.

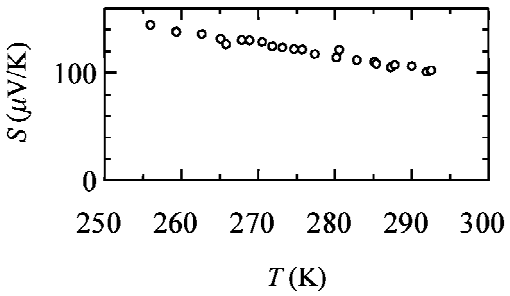

Figure 3.14: Temperature dependence of the thermoelectric power for (BEDT-TTF)$_2$GaCl$_4$.

3.3 α'-(BEDT-TTF)$_2$IBr$_2$

3.3.1 Band calculation

The band structure calculated using the data of the reported crystal structure [51] is shown in Fig. 3.15. The band structure is the 3/4-filled state reflecting the weak dimerization of this salt. In contrast with β'-(BEDT-TTF)$_2$ICl$_2$ and (BEDT-TTF)$_2$GaCl$_4$, this band structure is featured without the splitting between the upper and lower bands, giving a large band width of about 0.6 eV. The semimetallic Fermi surfaces show the existence of two kinds of carriers.

3.3.2 Susceptibility

Figure 3.16 shows the temperature dependence of the susceptibility in the field perpendicular to the c*-axis. The fitting of the susceptibility to the Curie-Weiss law above 150 K shown in the inset of Fig. 3.16 gives a Weiss constant of Θ=–40±15 K and a Curie constant of C=0.32±0.02 emu/mol K corresponding to 1.60±0.05 μ_B per formula unit. It has a broad maximum around 60 K and goes to zero independent of the field direction ($H//c$* or $H \perp c$*). Inconsistency in the absolute value of the susceptibility compared with the previous report [36] comes from the same reason for the β'-salt. The magnetization at 2 K does not show any spin flop transition up to 55 kOe. Thus, the magnetic ground state is suggested to be a singlet state.

3.3.3 Resistivity

The resistivity of α'-(BEDT-TTF)$_2$IBr$_2$ at 1 bar is shown in Fig. 3.17. The resistivity is about 0.5 - cm at room temperature and indicates a phase transition around 200 K as reported in ref. [36], where E_a=0.20±0.04 eV above 210 K and 0.22±0.04 eV below 190 K, respectively. The pressure dependence of the resistivity is shown in Fig. 3.18. The resistivity is reduced down to ∼0.07 - cm at 10 kbar as the pressure increases. The temperature dependence of the resistivities under pressure were measured at 8.4 kbar and 12 kbar as shown in Fig. 3.17. The phase transition temperature of ∼200 K at ambient pressure is lowered down to ∼110 K at 8.4 kbar, and moreover we see the region with a low activation energy of ∼0.024 eV above ∼200 K at 12 kbar.

3.3.4 Thermoelectric power

The temperature dependence of the thermoelectric power is shown in Fig. 3.19. In contrast with the β'-(BEDT-TTF)$_2$ICl$_2$ and (BEDT-TTF)$_2$GaCl$_4$, the thermoelectric power has a small positive value of about 25 μV/K at room temperature, and in addition, it shows a change in its sign from positive to negative around 270 K indicating the change of the domi-

nant carriers from holes to electrons. There is a kink at ∼220 K which corresponds with the resistivity anomaly. Below the kink, the thermoelectric power has an increasing trend.

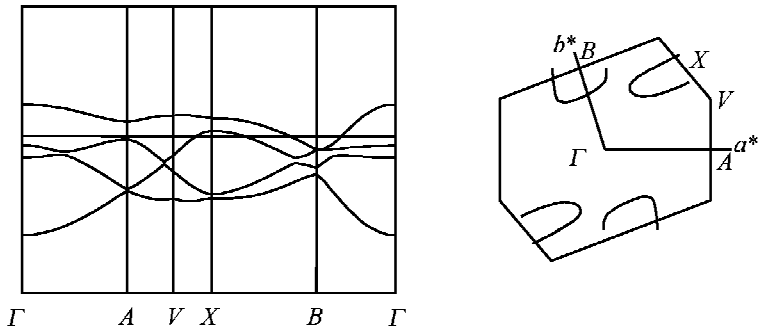

Figure 3.15: Band structure and Fermi surface for α'-(BEDT-TTF)$_2$IBr$_2$. The band structure indicates a 3/4-filled state having electron and hole carriers. The band width is about 0.6 eV.

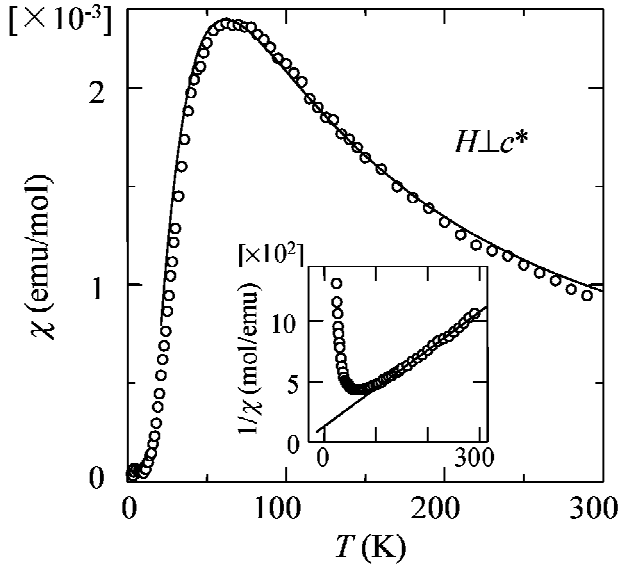

Figure 3.16: Temperature dependence of the susceptibility for α'-(BEDT-TTF)$_2$IBr$_2$. The solid curve denotes the fitting to the S=1/2 one-dimensional alternating chain Heisenberg antiferromagnet model with J=–56 K and J'=–23 K. The inset shows the reciprocal susceptibility plot with a fitting to the Curie-Weiss law above 150 K.

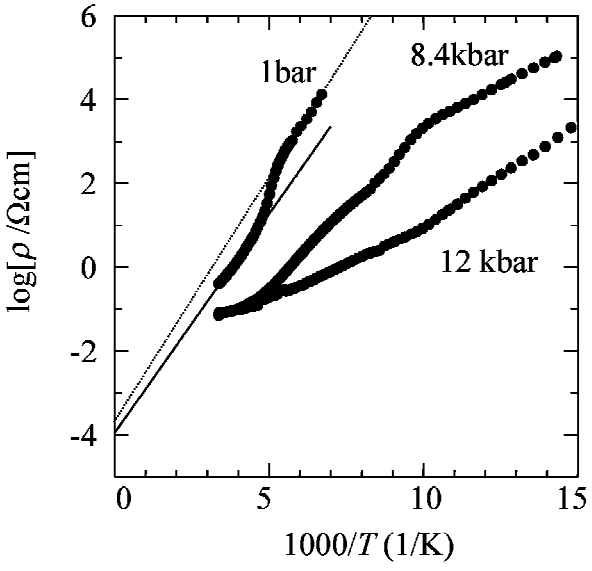

Figure 3.17: Temperature dependence of the resistivities for α'-(BEDT-TTF)$_2$IBr$_2$ under 1 bar, 9 kbar, and 12 kbar. The solid and dotted lines are Arrhenius fittings above 210 K with the activation energy of $E_a \approx 0.20$ eV and below 190 K with $E_a \approx 0.22$ eV, respectively.

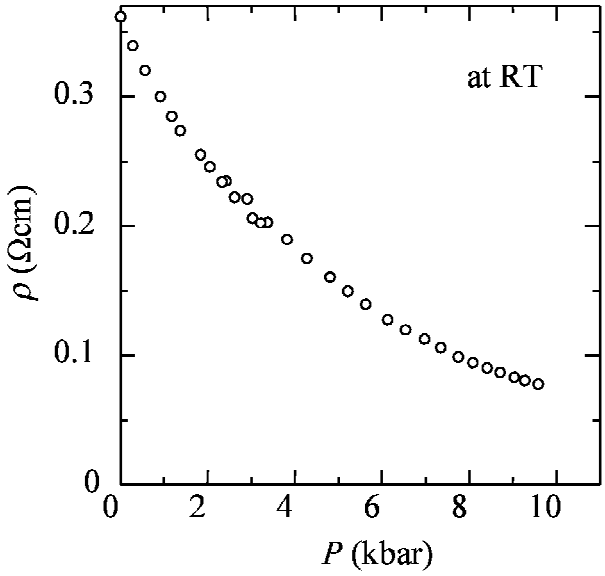

Figure 3.18: Pressure dependence of the resistivity for α'-(BEDT-TTF)$_2$IBr$_2$ at room temperature.

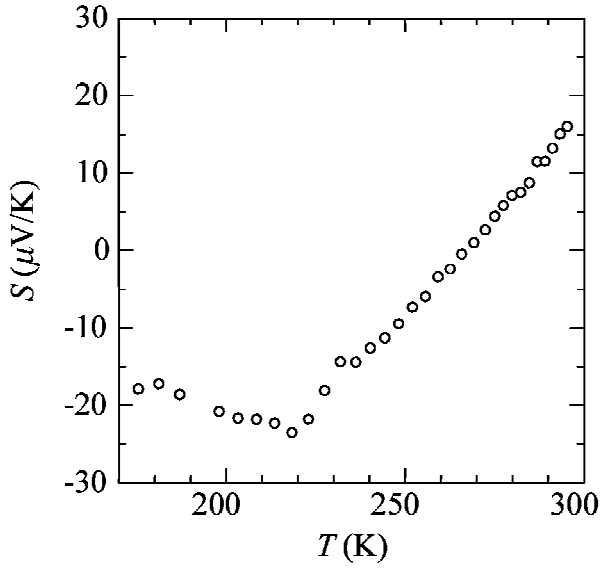

Figure 3.19: Temperature dependence of the thermoelectric power for α'-(BEDT-TTF)$_2$IBr$_2$. A kink around 220 K corresponds to the transition observed in the resistivity.

3.4 (EDO-TTFBr$_2$)$_2$AsF$_6$

3.4.1 Crystal structure and band calculation

The analysis of X-ray diffraction data with 2554 reflections results in the final R factor R=0.035. The crystal structure, where the composition was given to be (EDO-TTFBr$_2$)$_2$-AsF$_6$, was found to be triclinic $P\bar{1}(Z=2)$. The crystallographic data and the atomic coordinates with thermal parameters are summarized in Tables 3.1 and 3.2, respectively. The crystal structure is shown in Fig. 3.20. A head-to-tail arrangement of asymmetric donor molecules is formed in the direction of face-to-face molecular contacts along the c-axis, where the shortest inter-molecular S-S atomic contact 3.661 Å is almost the same with the corresponding van der Waals distance 3.60 Å. In the side-by-side direction along the a-axis as shown in Figs. 3.20(b) and (c), there are inter-molecular S-S and S-O contacts 3.775 Å and 3.640 Å, respectively, which are longer than the van der Waals distances (3.60 Å and 3.32 Å for S-S and S-O contacts, respectively). Thus, the crystal structure is characterized with a quasi two-dimensional donor structure consisting of the two-dimensional arrangement of one-dimensional chains along the c-axis, where the presence of anion sheets in the galleries makes the two-dimensional layers separated from each other.

The transfer integral network in the donor sheet in the ac-plane is shown in Fig. 3.21. The transfer integrals t_{c1} and t_{c2} along the face-to-face direction are more than 5 times larger than those in the side-by-side directions, suggesting a one-dimensional feature in the electronic structure. In the one-dimensional chain, there is an alternation in the strengths of the transfer integrals which is described in terms of dimerization in other words. The band structure is shown in Fig. 3.21(b), where the Fermi level is located around the midpoint of the upper band according to the 2:1 donor-to-anion ratio, and the presence of a one-dimensional Fermi surface along the c^*-axis is consistent with the crystal structure.

3.4.2 Susceptibility

Figure 3.22 shows the temperature dependence of the susceptibility under a magnetic field of 10 kOe. The susceptibility, whose room temperature value is about $5.5\pm0.5\times10^{-4}$ emu/mol, is gradually reduced as the temperature is lowered down to about 35 K, at which an anomaly appears. It should be noted that the anomaly is obviously observed in the susceptibility which has been obtained by subtracting a Curie-type impurity contribution from the experimental result. We carried out the anisotropy measurement of the susceptibility for the field parallel and perpendicular to the c-axis, which gave almost the same behavior even below 35 K. The crystal arrangement with distinction between the a- and b-axes could not be carried out because of the sharp needle-type crystal shape. This makes difficult the anisotropy measurement between the a- and b-axes. The magnetization curves at 2 K did not show any spin flop transition up to 55 kOe both in the field parallel and perpendicular to the c-axis,

whereas a magnetic impurity has a largely contribution in the magnetization curve.

3.4.3 ESR

The ESR line shape is a Lorentzian-type with the peak-to-peak line width of about 20 Oe at room temperature. The angular dependence of the line width around a^*-axis is shown in Fig. 3.23. The line width with an ordinary trigonometric functional dependence has a minimum in the field parallel to the c-axis. The temperature dependence of the line width is shown in Fig. 3.24(a). It becomes narrow as the temperature is lowered down to 45 K, followed by an upturn below 45 K which diverges at 37 K. The ESR signal intensity obeys the temperature dependence of the susceptibility in the high temperature range down to 45 K. It gets small below about 40 K and vanishes below 37 K with the g-value shift as shown in Fig. 3.24(b).

3.4.4 Resistivity

The temperature dependence of the resistivity shown in Fig. 3.25 is semiconductive with a room temperature resistivity of about 0.06 - cm and an activation energy of 0.13 ± 0.01 eV. The pressure dependence of the resistivity at room temperature is shown in Fig. 3.26. The resistivity decreases monotonously as the pressure increases. The temperature dependence of the resistivity under pressure is also semiconductive even at 9 kbar with an activation energy E_a of 0.094 ± 0.01 eV as shown in Fig. 3.25.

3.4.5 Thermoelectric power

The thermoelectric power shown in Fig. 3.27 has a $1/T$ temperature dependence with the room temperature value of about $+60$ μV/K. This indicates the dominance of hole-type carriers behaving semiconductively.

Table 3.1: Crystallographic data of (EDO-TTFBr$_2$)$_2$AsF$_6$.

space group	$P\bar{1}$
formula	$(C_8H_4S_4O_2Br_2)_2AsF_6$
crystal system	triclinic
a (Å)	7.099(5)
b (Å)	14.844(4)
c (Å)	7.019(3)
α (°)	93.16(4)
β (°)	106.07(0)
γ (°)	79.81(8)
V (Å^3)	699.9
Z	2
observed reflections	2554
R	0.035

Table 3.2: Atomic parameters of (EDO-TTFBr$_2$)$_2$AsF$_6$.

atom	x	y	z	U_{sq} (Å^2)
S1	0.62046(15)	0.31489(7)	0.7416(2)	0.0351(2)
S2	0.19761(14)	0.40244(7)	0.6432(2)	0.0350(2)
S3	0.74203(14)	0.52008(7)	0.8199(2)	0.0335(2)
S4	0.31504(14)	0.59787(7)	0.7101(2)	0.0363(2)
C1	0.4474(6)	0.4150(3)	0.7135(6)	0.0306(8)
C2	0.4974(5)	0.5001(3)	0.7444(6)	0.0295(7)
C3	0.4411(6)	0.2440(3)	0.6776(6)	0.0363(9)
C4	0.2496(6)	0.2839(3)	0.6340(6)	0.0343(8)
C5	0.6759(6)	0.6389(3)	0.8266(6)	0.0313(8)
C6	0.4828(6)	0.6737(3)	0.7775(6)	0.0317(8)
C7	0.3447(11)	0.1047(4)	0.6859(15)	0.086(2)
C8	0.1529(10)	0.1434(4)	0.5607(12)	0.068(2)
O1	0.5045(5)	0.1540(2)	0.6787(6)	0.0508(8)
O2	0.0927(5)	0.2399(2)	0.5857(5)	0.0450(7)
Br1	0.88162(7)	0.70664(3)	0.90497(7)	0.04198(13)
Br2	0.37195(7)	0.79700(3)	0.77951(7)	0.04556(14)
As	0.0000	0.0000	0.0000	0.0418(2)
F1	0.0539(6)	-0.1129(2)	0.0610(6)	0.0738(10)
F2	-0.0938(8)	0.0265(3)	0.1981(7)	0.104(2)
F3	0.2270(6)	0.0180(3)	0.1349(8)	0.108(2)

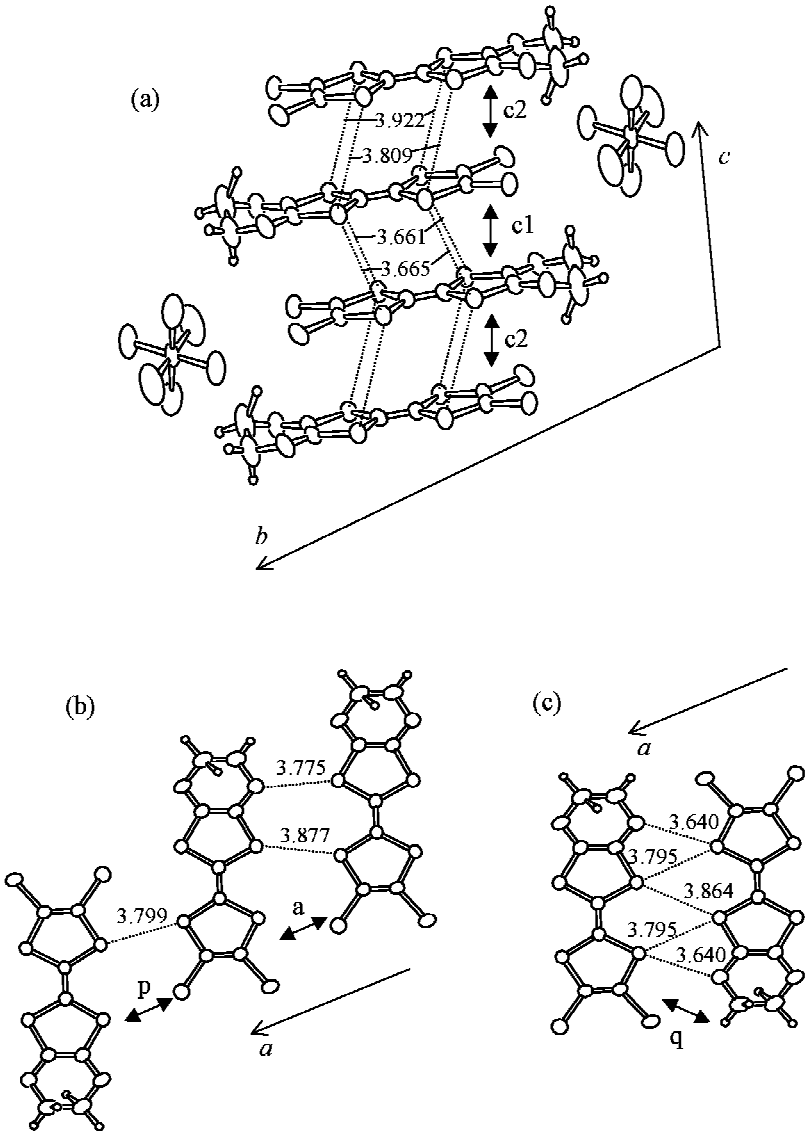

Figure 3.20: Crystal structure of $(EDO\text{-}TTFBr_2)_2AsF_6$. Dotted lines are the nearest inter-molecular S-S distances and double arrows indicate the molecular pairs connected by transfer integrals a, c1, c2, p, and q (see Fig. 3.21). (a) The view of the donor stacking structure projected on the *bc*-plane. (b) and (c) The views along the side-by-side direction. The numbers indicate the inter-molecular atomic distances (Å).

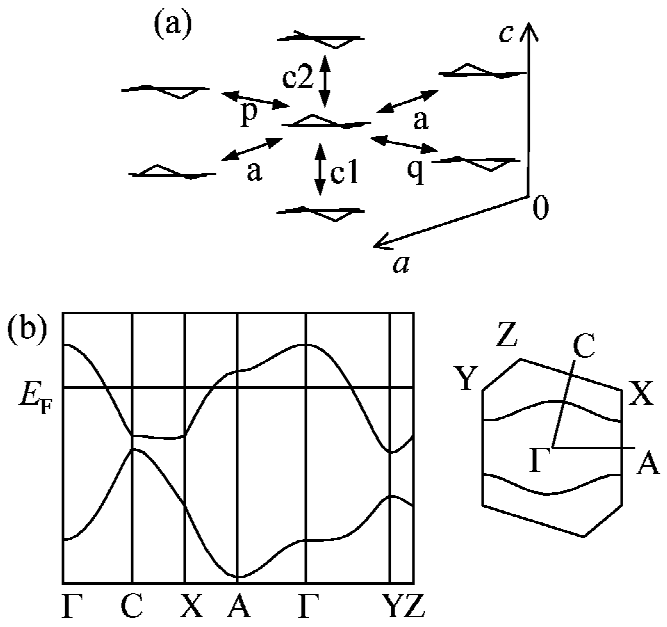

Figure 3.21: (a) Schematic view of the crystal structure of (EDO-TTFBr$_2$)$_2$AsF$_6$ in the *ac*-plane. The inter-molecular transfer integrals are as follows; t_{c1}=27.5, t_{c2}=20.8, t_a=3.85, t_p=1.24, and t_q=–2.44×10^{-2} eV. (b) Band structure and Fermi surface. The upper band width is estimated at about 0.52 eV.

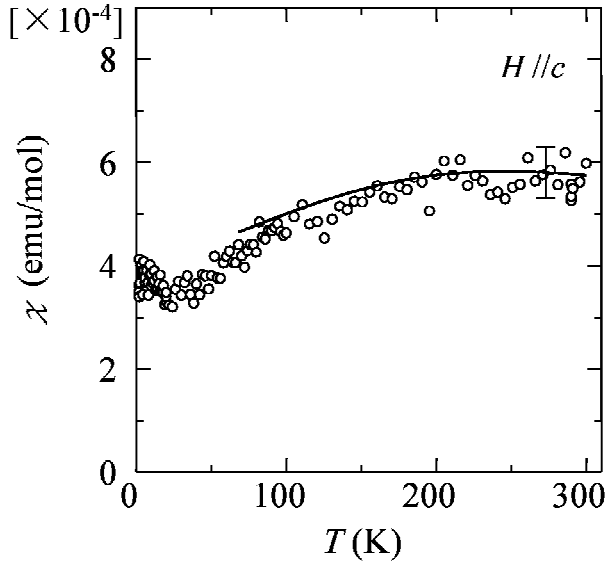

Figure 3.22: Temperature dependence of the susceptibility measured at H=10 kOe for (EDO-TTFBr$_2$)$_2$AsF$_6$ with an error bar of about $\pm 0.5\times10^{-4}$ emu/mol. The solid curve is the fitting result for the S=1/2 one-dimensional Heisenberg antiferromagnet model with J=–190 K.

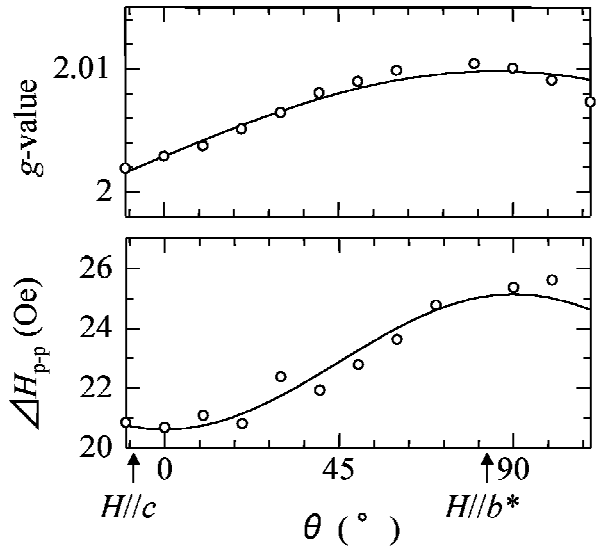

Figure 3.23: Angular dependence of (a) the g-value and (b) the ESR line width around the a*-axis for (EDO-TTFBr$_2$)$_2$AsF$_6$ at room temperature. The crystal axes was refined from the g-value. The solid curves are splines for a cosine function with 2π period.

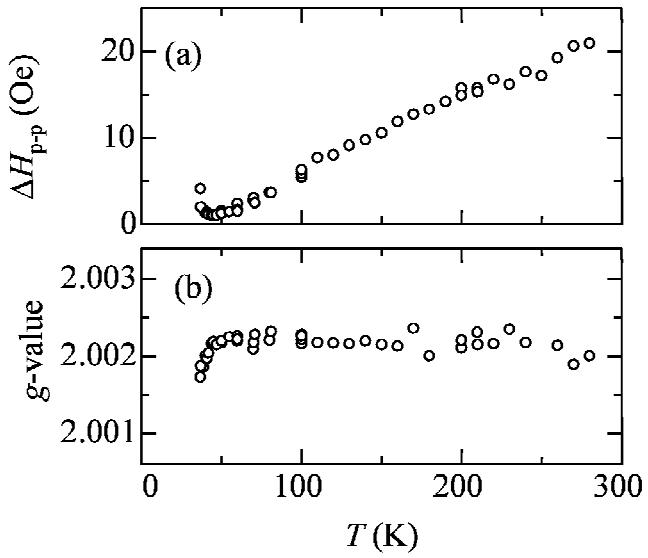

Figure 3.24: Temperature dependence of (a) the ESR line width and (b) the g-value for (EDO-TTFBr$_2$)$_2$AsF$_6$.

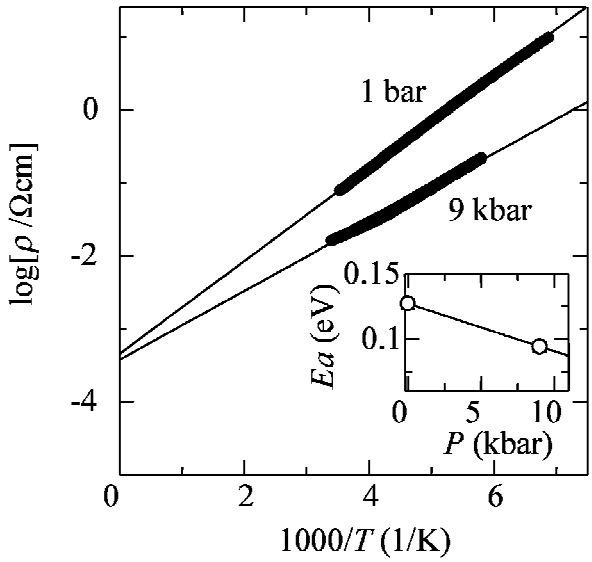

Figure 3.25: Temperature dependence of the resistivity for (EDO-TTFBr$_2$)$_2$AsF$_6$. The solid lines are the Arrhenius fittings with the activation energies of 0.13 eV and 0.09 eV at ambient pressure and 9 kbar, respectively. The inset plots activation energies vs pressure.

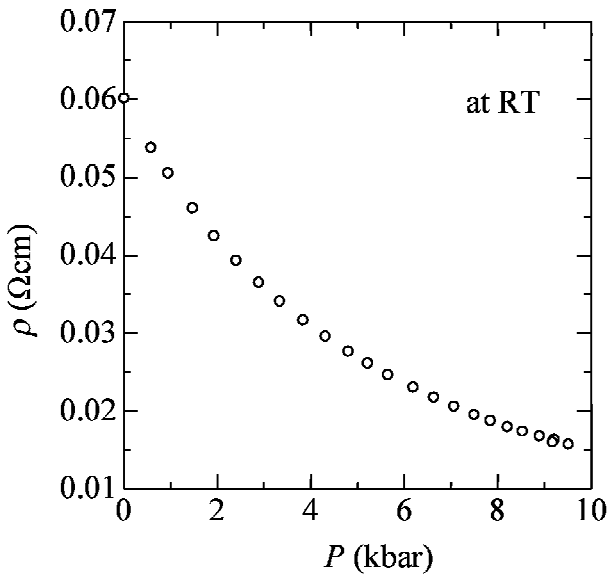

Figure 3.26: Pressure dependence of the resistivity for (EDO-TTFBr$_2$)$_2$AsF$_6$ at room temperature.

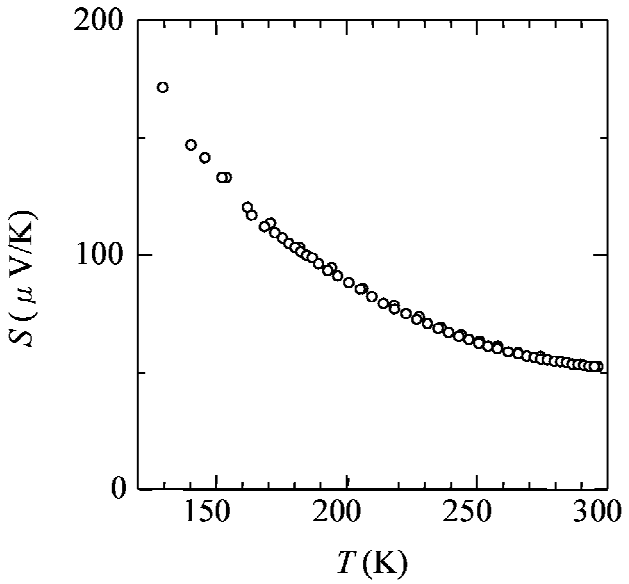

Figure 3.27: Temperature dependence of the thermoelectric power for (EDO-TTFBr$_2$)$_2$AsF$_6$.

3.5 (BMDT-TTF)$_3$ClO$_4$(1,2-dichloroethane)

3.5.1 Susceptibility

The temperature dependence of the susceptibility is shown in Fig. 3.28. The reciprocal susceptibility shown in the inset of Fig. 3.28 obeys the Curie-Weiss law with a Weiss constant of Θ=–50±10 K and a Curie constant of C=0.43±0.02 emu/mol K corresponding to 1.85±0.05 μ_B per formula unit above 150 K. In much lower temperature range, a broad maximum emerges around 40 K suggesting the behavior of short-range ordering. No antiferromagnetic transition is observed both in the temperature dependence of the susceptibility and in the magnetization up to 50 kOe at 2 K.

3.5.2 ESR

The ESR signal shows a Lorentzian-type line shape with the line width of about 8 Oe ($H//c$) at room temperature. The g-values at room temperature are estimated at 2.004, 2.014, and 2.005, in the field parallel to the a-, b-, and c-axes, respectively. The temperature dependences of the line width and g-value are shown in Fig. 3.29. The line width decreases moderately in the high temperature range above 50 K as the temperature is lowered, and then, it shows a steep decrease below ca. 50 K which is followed by an upturn appearing below 10 K.

3.5.3 Resistivity and thermoelectric power

The temperature dependence of the resistivity is shown in Fig. 3.30 (open circle). The resistivity behaves semiconductively with the room temperature resistivity of ∼260 - cm and an activation energy of 0.14±0.04 eV above 250 K, which slightly decreases down to 0.09±0.02 eV below ∼250 K. The pressure dependence of the resistivity at room temperature is shown in Fig. 3.31. It gradually decreases as the pressure is elevated. The temperature dependence at 9.6 kbar was plotted in Fig. 3.30 (closed circles) with an Arrhenius fitting curve of an activation energy of ∼0.20±0.04 eV above 230 K. A gentle kink around 230–250 K at 9.6 kbar indicates the small pressure-dependence.

The thermoelectric power at room temperature is about +20±10 μV/K. The temperature dependence could not be measured due to the high resistance of this salt.

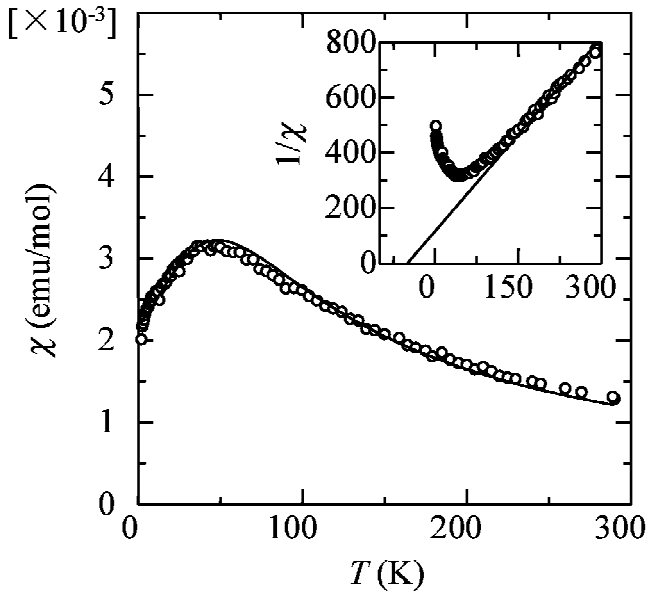

Figure 3.28: Temperature dependence of the susceptibility for (BMDT-TTF)$_3$ClO$_4$(1,2-dichloroethane). The solid curve is the fitting for the one-dimensional Heisenberg antiferromagnet model with J=–37 K. Inset figure shows the reciprocal susceptibility fitted using the Curie-Weiss law with a Weiss constant of Θ=–50±10 K and a Curie constant of C=0.43±0.02 emu/mol K above 150 K.

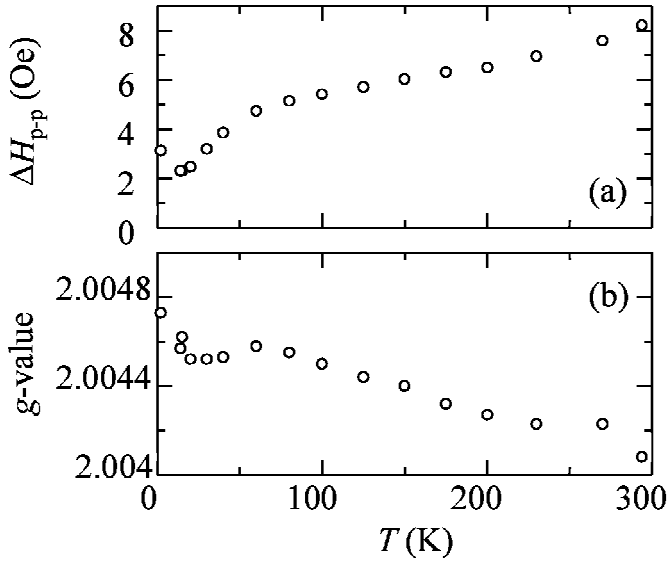

Figure 3.29: Temperature dependence of (a) the ESR line width and (b) g-value in the applied field perpendicular to the b-axis for (BMDT-TTF)$_3$ClO$_4$(1,2-dichloroethane).

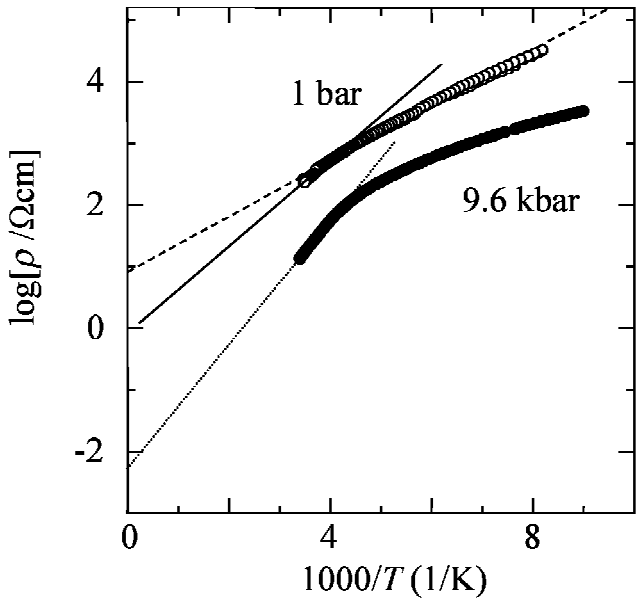

Figure 3.30: Temperature dependence of the resistivity for (BMDT-TTF)$_3$ClO$_4$(1,2-dichloroethane). The Arrhenius fittings for the data at ambient pressure give the activation energies of ∼0.14 eV above 250 K (dashed line) and ∼ 0.09 eV below 250 K (solid line). The activation energy at 9.6 kbar around room temperature is ∼0.20 eV (dotted line).

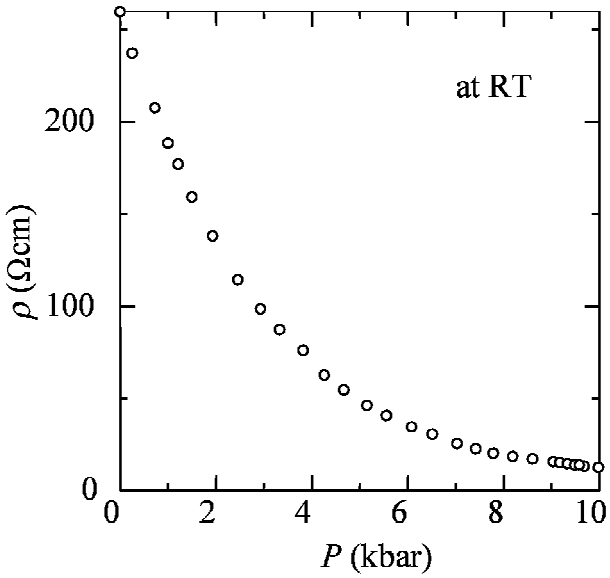

Figure 3.31: Pressure dependence of the resistivity at room temperature for (BMDT-TTF)$_3$-ClO$_4$(1,2-dichloroethane).

3.6 (BMDT-TTF)$_3$AsF$_6$(1,1,2-trichloroethane)

3.6.1 Crystal structure and band calculation

The crystal structure of (BMDT-TTF)$_3$AsF$_6$(1,1,2-trichloroethane) is shown in Fig. 3.32. It was found to be isostructural to that of (BMDT-TTF)$_3$ClO$_4$(1,2-dichloroethane) [42] from the analysis of the crystallographic data summarized in Table 3.3. The final R-value was 0.090 on the basis of 1113 independent reflections with the final atomic coordinates summarized in Table 3.4.

Table 3.5 shows the bond lengths of BMDT-TTF molecules in this salt and the ClO$_4$ salt. There coexist two independent BMDT-TTF molecules A and B having almost the same bond lengths, indicating no appreciable difference between A and B molecules which suggests the presence of negligible charge disproportionation between A and B if any. This is in contrast with the isostructural ClO$_4$ salt that has an appreciable charge disproportionation between A and B molecules. The transfer integrals between donor molecules and the energy band structures at room temperature were calculated on the basis of the tight-binding method with the extended Hückel scheme. The band structure and the Fermi surface are shown in Fig. 3.33. The electronic structure is described in terms of the 5/6-filled band with the coexistence of a one-dimensional Fermi surface along the c-axis and a two-dimensional Fermi surface on the ac-plane.

3.6.2 Susceptibility

The temperature dependence of the susceptibility is shown in Fig. 3.34. The susceptibility has almost the same value ($\sim$1.2$\times$10^{-3} emu/mol at room temperature) with that of (BMDT-TTF)$_3$ClO$_4$(1,2-dichloroethane). The inset of Fig. 3.34 shows the reciprocal susceptibility plot with a Curie-Weiss fitting giving the Weiss constant Θ=–15$\pm$3 K and a Curie constant of C=0.40$\pm$0.02 emu/mol K corresponding to 1.79$\pm$0.05 $\mu_{\rm B}$ above 150 K. Meanwhile, the data show a change in both a Weiss constant and the Curie constant around 150–200 K. To indicate this anomaly more clearly, the $1/\chi T$ vs $1/T$ plot is exhibited in Fig. 3.35. The fitting of the data to the Curie-Weiss law between 50–150 K (solid line) gives a Weiss constant of Θ=–23$\pm$1 K and C=0.42$\pm$0.01 emu/mol K (1.83$\pm$0.02 $\mu_{\rm B}$).

3.6.3 ESR

The ESR signal has a Lorentzian-type line shape with a line width of about 8–10 Oe at room temperature that is almost the same to that for the ClO$_4$ salt. The temperature dependence of the line widths is shown in Fig. 3.36. The line width has a steep decrease with an inflection point around 150 K in the line width vs temperature plot at high temperatures with the lowering of the temperature. Below $\sim$5 K, the line width indicates a fractional upturn. The ESR g-values at room temperature are estimated at 2.003, 2.014, and 2.005, in

the field parallel to the *a*-, *b*-, and *c*-axes, respectively, which have almost no temperature dependence as shown in Fig. 3.37.

3.6.4 Resistivitiy

The temperature dependence of the resistivity at 1 bar and 11.4 kbar is shown in Fig. 3.38. An activation energy is estimated at 0.14±0.02 eV in the high temperature range above the transition with a hysteresis in the wide temperature range between 220 and 290 K. The hysteretic behavior of the AsF_6 salt is largely dependent on samples. The pressure dependence of the resistivity at room temperature is shown in Fig. 3.40. The resistivity decreases steeply as the pressure is elevated in the pressure range up to 7 kbar at which it becomes more than two orders of magnitude smaller than that at ambient pressure. The temperature dependence of the resistivity under pressure up to 11.4 kbar is shown in Fig. 3.39. The temperature dependence is characterized by the following two features. The hysteretic region shifts to lower temperature under higher pressure and then the hysteresis disappears at 11.4 kbar as shown in Fig. 3.39. The temperature range with a small activation energy appears under high pressures. This trend becomes most obvious at 11.4 kbar where the activation energy is estimated at ∼0.007 eV above 200 K. In particular, the resistivity at 11.4 kbar increases to the order of 100 - cm at 160 K from ∼0.5 - cm at 180 K discontinuously, suggesting that the transition is modified to a metal-insulator phase transition around 160 K.

3.6.5 Thermoelectric power

The thermoelectric power is shown in Fig. 3.41. It has a positive value of about 67 μV/K which is independent of temperature above 290 K, whereas it has large sample dependence below this temperature. It gradually decreases to about –100 μV/K from 290 K to 200 K in several samples. Additionally, other samples show almost temperature-independent thermoelectric power in the same temperature region as well as the region above 290 K. The temperature-dependent region on the thermoelectric power corresponds to the phase transition characterized with the wide hysteresis of the resistivity as shown in Fig. 3.39.

Figure 3.42 shows the pressure dependence of the thermoelectric power at room temperature. The room temperature value of ∼67 μV/K decreases down to 60 μV/K as the pressure increases up to ∼7 kbar, and it becomes almost constant above 7 kbar. The trend in the thermoelectric power vs pressure curve has the similar to the resistivity vs pressure plot (Fig. 3.40). The temperature dependence of the thermoelectric power at 9 kbar is shown in Fig. 3.43. The thermoelectric power at 9 kbar gradually decreases as temperature is lowered, in contrast with the temperature-independent behavior at ambient pressure.

Table 3.3: Crystallographic data of (BMDT-TTF)$_3$AsF$_6$(1,1,2-trichloroethane).

Chemical formula	$(C_8H_4S_8)_3AsF_6(C_2H_3Cl_3)$
Crystal system	orthorhombic
Space group	$Pnma$
a/Å	12.65(3)
b/Å	35.35(2)
c/Å	10.310(4)
α/°	90
β/°	90
γ/°	90
V/Å^3	4609(10)
Z	4
observed reflections ($\|F_0\| > 4\sigma(F_0)$)	1113
R	0.090

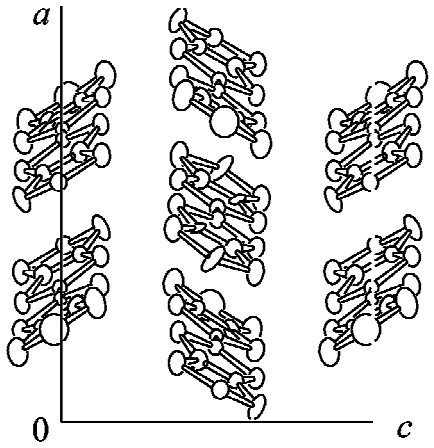

Figure 3.32: Crystal structure of (BMDT-TTF)$_3$AsF$_6$(1,1,2-trichloroethane) along the b-axis.

Table 3.4: Atomic parameters of (BMDT-TTF)$_3$AsF$_6$(1,1,2-trichloroethane).

Atom	x	y	z	U(iso)
S1	0.2849(9)	0.5219(2)	-0.1261(9)	0.033(1)
S2	0.3974(9)	0.5094(3)	0.124(1)	0.035(1)
S3	0.2196(9)	0.4331(3)	-0.130(1)	0.032(1)
S4	0.3289(9)	0.4225(3)	0.122(1)	0.038(1)
S5	0.3603(9)	0.6041(3)	-0.129(1)	0.040(1)
S6	0.4666(9)	0.5922(3)	0.127(1)	0.040(1)
S7	0.166(1)	0.3483(3)	-0.141(1)	0.052(2)
S8	0.285(1)	0.3372(3)	0.108(1)	0.056(2)
C1	0.323(3)	0.4901(9)	-0.003(3)	0.028(4)
C2	0.298(3)	0.4536(9)	-0.002(3)	0.020(4)
C3	0.3496(3)	0.5597(9)	-0.058(4)	0.024(4)
C4	0.397(3)	0.5548(9)	0.058(4)	0.029(4)
C5	0.223(3)	0.3862(9)	-0.066(4)	0.030(4)
C6	0.278(3)	0.381(1)	0.046(3)	0.037(5)
C7	0.423(3)	0.627(1)	0.009(3)	0.041(5)
C8	0.219(4)	0.315(1)	-0.026(4)	0.055(6)
S9	-0.0838(9)	0.4597(3)	-0.123(1)	0.033(1)
S10	0.0214(9)	0.4518(3)	0.129(1)	0.034(1)
S11	-0.141(1)	0.3755(3)	-0.122(1)	0.045(1)
S12	-0.036(1)	0.3679(3)	0.140(1)	0.043(1)
C9	-0.014(3)	0.4822(9)	0.000(3)	0.023(4)
C10	-0.083(3)	0.415(1)	-0.051(4)	0.026(4)
C11	-0.035(3)	0.411(1)	0.061(6)	0.027(4)
C12	-0.114(4)	0.344(1)	0.015(8)	0.051(6)
As	0.4557(9)	0.25	0.742(1)	0.087(2)
F1	0.392(6)	0.25	0.890(7)	0.090(6)
F2	0.520(4)	0.25	0.601(4)	0.18(1)
F3	0.531(4)	0.284(1)	0.795(4)	0.151(7)
F4	0.364(4)	0.282(1)	0.685(4)	0.18(1)
Cl1	0.088(4)	0.292(1)	0.305(4)	0.07(1)
Cl2	0.296(4)	0.25	0.331(4)	0.255(9)
C21	0.078(4)	0.25	0.408(4)	0.06(2)
C22	0.194(4)	0.25	0.462(4)	0.25(4)

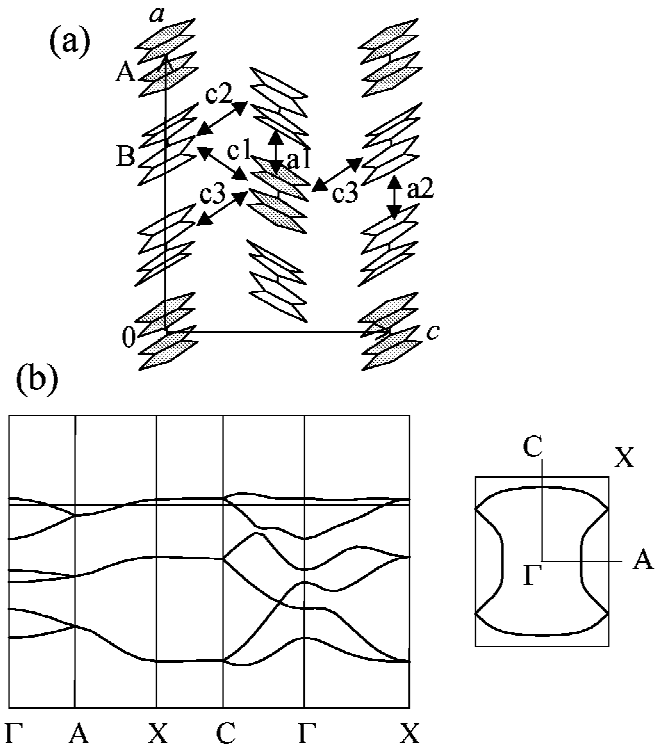

Figure 3.33: (a) Schematic view of the donor arrangement in (BMDT-TTF)$_3$AsF$_6$(1,1,2-trichloroethane) along the b-axis with the transfer integrals: t_{a1}=–5.58, t_{a2}=–6.88, t_{c1}=–10.2, t_{c2}=11.0 and t_{c3}=13.7$\times 10^{-2}$ eV. (b)Band structure and Fermi surface. The band width is estimated at about 0.76 eV.

Table 3.5: Bond lengths of BMDT-TTF molecules (A and B molecules) in (BMDT-TTF)$_3$ClO$_4$(1,2-dichloroethane) and (BMDT-TTF)$_3$AsF$_6$(1,1,2-trichloroethane).

	a (Å)		b(Å)		c(Å)		d(Å)	
	A	B	A	B	A	B	A	B
MT$_3$ClO$_4$DCE[a]	1.41	1.35	1.73	1.76	1.73	1.74	1.36	1.32
MT$_3$AsF$_6$TCE	1.34	1.33	1.75	1.77	1.72	1.74	1.38	1.36

[a]Ref. [43].

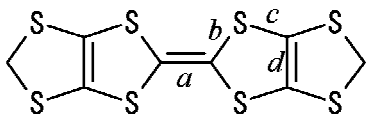

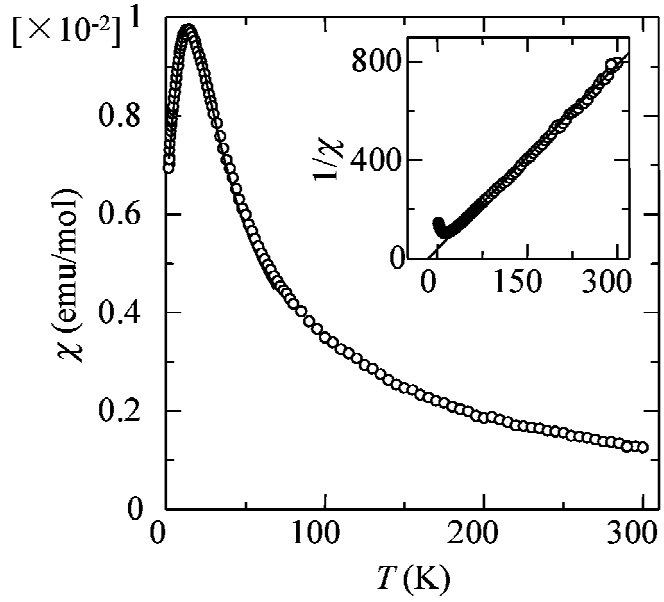

Figure 3.34: Temperature dependence of the susceptibility for (BMDT-TTF)$_3$AsF$_6$(1,1,2-trichloroethane). The solid curve is the fitting result for the one-dimensional Heisenberg antiferromagnet model with J=–11 K between 2 and 60 K. The inset is the reciprocal susceptibility with a Curie-Weiss fitting giving Θ=–15 K above 150 K.

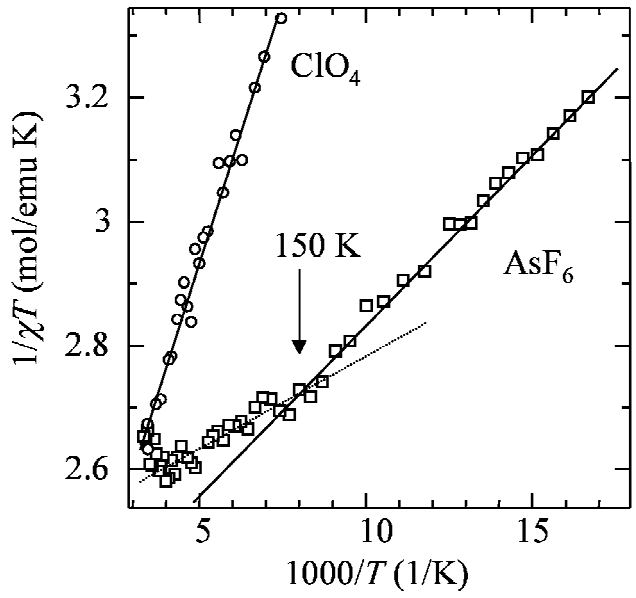

Figure 3.35: The $1/\chi T$ vs $1/T$ plot for (BMDT-TTF)$_3$AsF$_6$(1,1,2-trichloroethane) (square) and (BMDT-TTF)$_3$ClO$_4$(1,2-dichloroethane) (circle). The solid and dotted lines are the Curie-Weiss fittings (see text).

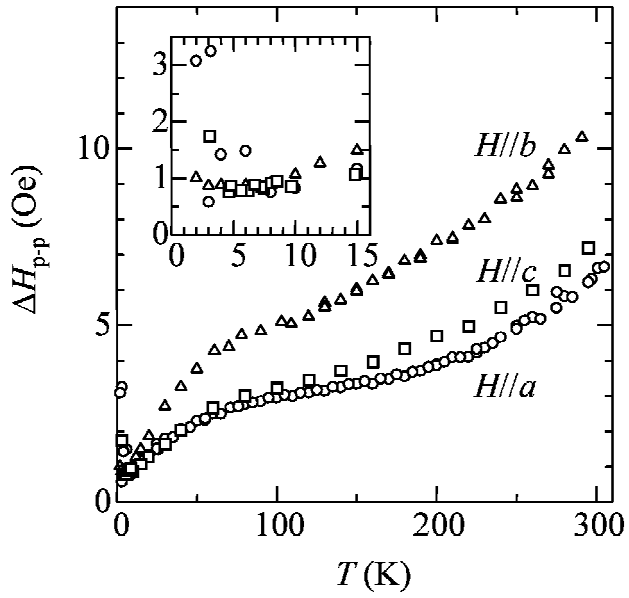

Figure 3.36: Temperature dependence of the ESR line widths for (BMDT-TTF)$_3$AsF$_6$(1,1,2-trichloroethane). The inset shows the details at low temperatures.

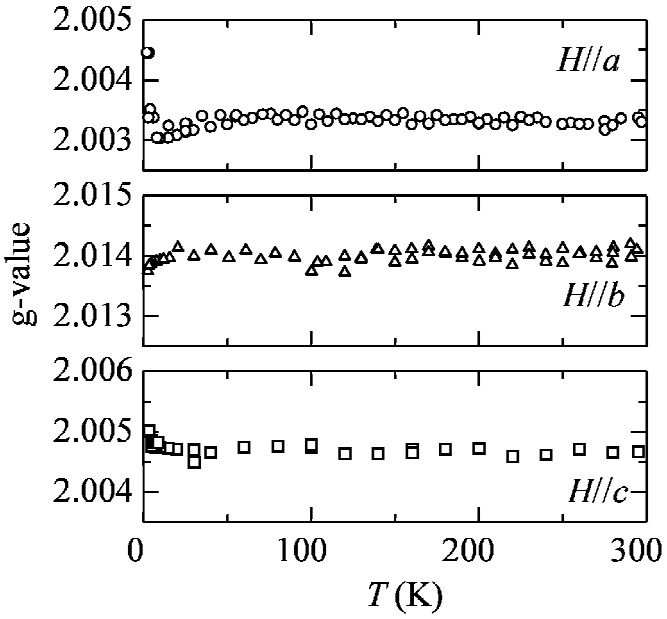

Figure 3.37: Temperature dependence of the g-values for (BMDT-TTF)$_3$AsF$_6$(1,1,2-trichloroethane) in the field parallel to the three independent crystallographic axes.

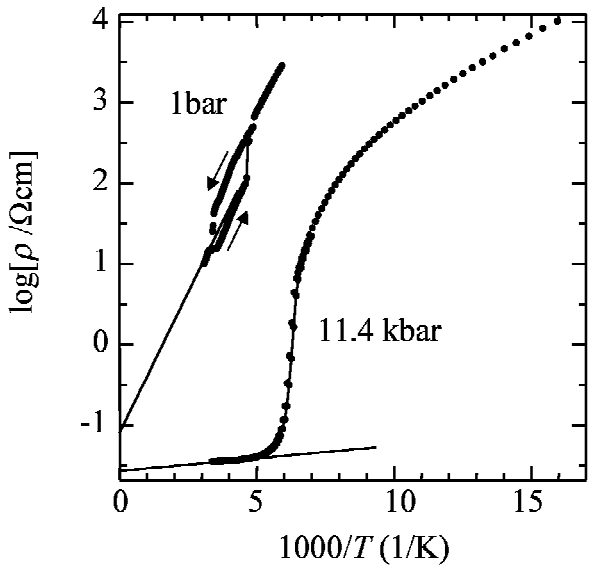

Figure 3.38: Temperature dependence of the resistivity for (BMDT-TTF)$_3$AsF$_6$(1,1,2-trichloroethane). The activation energies in the high temperature range are estimated at $\sim$0.14 eV and 0.007 eV at ambient pressure and 11.4 kbar, respectively. The arrows indicate heating and cooling runs.

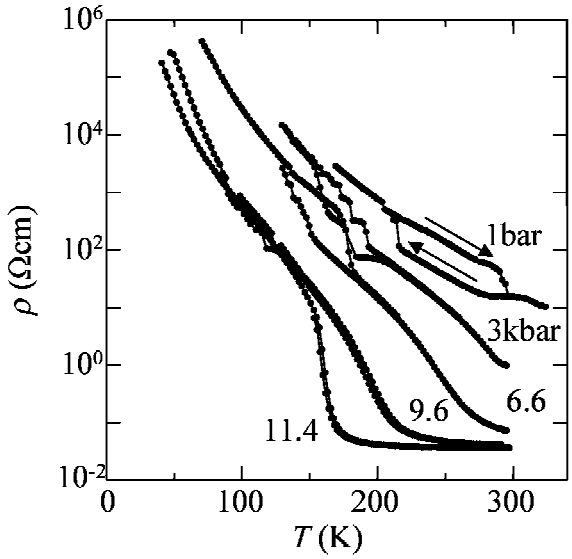

Figure 3.39: Temperature dependence of the resistivity for (BMDT-TTF)$_3$AsF$_6$(1,1,2-trichloroethane) under several pressures. The arrows indicate heating and cooling runs. The data at ambient pressure shows a wide range hysteresis between the heating and cooling runs in the temperature 220–290 K. The hysteresis decreases as the pressure increases. Under 11.4 kbar, the activation energy above 200 K gets negligibly small $E_a \approx 0.007$ eV (see Fig. 3.38).

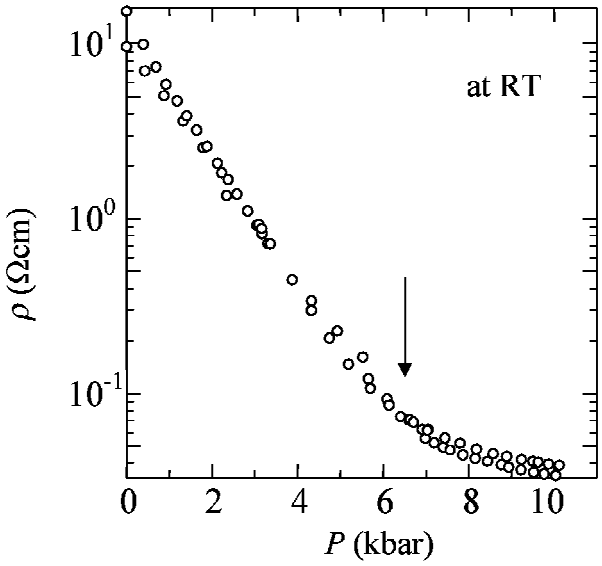

Figure 3.40: Pressure dependence of the resistivity for (BMDT-TTF)$_3$AsF$_6$(1,1,2-trichloroethane) at room temperature. The resistivity rapidly decreases below the pressure of about 7 kbar, afterward the decreasing tendency becomes weaken. There is an anomaly around 7 kbar as indicated by an arrow.

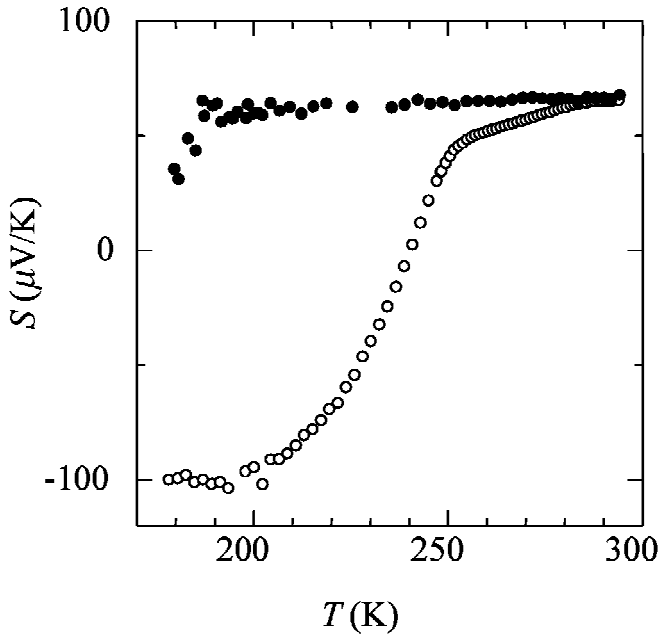

Figure 3.41: Temperature dependence of the thermoelectric power for (BMDT-TTF)$_3$AsF$_6$-(1,1,2-trichloroethane) with sample dependence (open circle and closed circle).

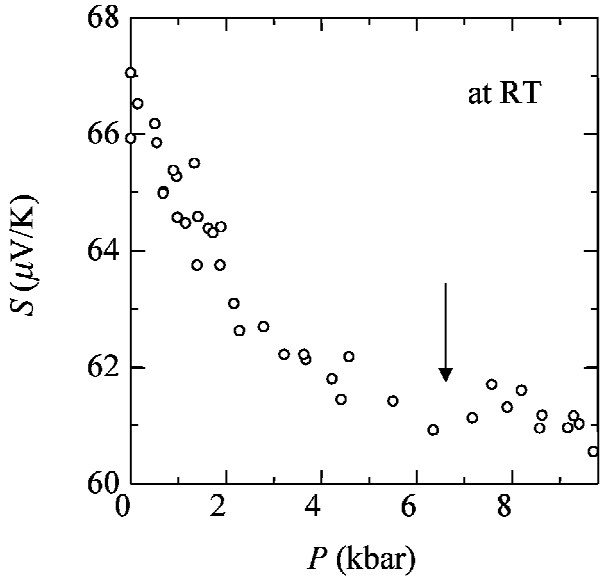

Figure 3.42: Pressure dependence of the thermoelectric power for (BMDT-TTF)$_3$AsF$_6$(1,1,2-trichloroethane). The arrow indicates the pressure at which the resistivity has an anomaly.

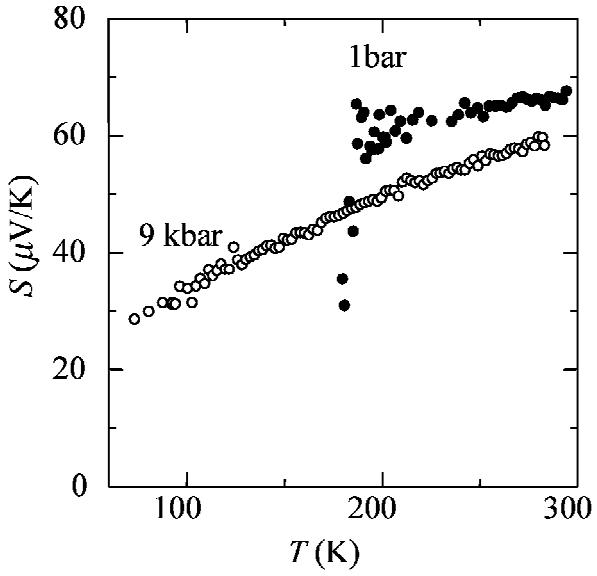

Figure 3.43: Temperature dependence of the thermoelectric power for (BMDT-TTF)$_3$AsF$_6$-(1,1,2-trichloroethane) under ambient pressure and 9 kbar.

Chapter 4

Discussion of magnetic properties

We discuss the magnetic structures of the charge transfer salts in the Mott insulator regime investigated in this work on the basis of the dimer/trimer unit. This systematic treatment gives the magnetic structures expected from the crystal structures in good agreement with the data of the susceptibilities. The discussion on the ESR line widths which reflect the low-dimensional magnetic properties adds complementary information on the feature of the electron localization/delocalization. Moreover, we discuss the relation between the strength of the dimerization/trimerization and the magnetic interaction.

4.1 Quasi two-dimensional antiferromagnetic (AF) structure of β'-(BEDT-TTF)$_2$X (X=ICl_2, $AuCl_2$)

For the consideration of the magnetic structure, we reexamine the structural feature of BEDT-TTF molecules in β'-(BEDT-TTF)$_2$X (X=ICl_2, $AuCl_2$) using a schematic structure depicted in Fig. 4.1(a) where the triclinic structures are simplified to indicate the paths of the transfer integrals clearly. Two BEDT-TTF molecules are strongly dimerized with face-to-face contacts along the b-axis. The charge neutrality rule in addition to the 2:1 composition ratio requires the presence of a hole per donor dimer, so that each dimer is considered to possess an S=1/2 spin. The spins on the dimers interact with each other through the inter-dimer exchange interactions which are related to the corresponding inter-dimer transfer integrals. Taking into account that the exchange interaction J is described in terms of the transfer integral t and the on-site Coulomb interaction U as $J \approx -t^2/U$ as mentioned in § 1.1.2, the estimation of the ratio of the interaction along the b-axis to that along the c-axis is given by $J_b/J_c = (|t_{\rm b2}|)^2/(|t_{\rm c}| + |t_{\rm c}| + |t_{\rm p}|)^2 \approx 1.0$ and 0.81 for the ICl_2 and $AuCl_2$ salts, respectively. Consequently, the magnetic structure is featured by a quasi two-dimensional square-lattice network in the bc-plane as shown in Fig. 4.1(b) taking account of the small value of the second nearest neighbor interaction corresponding to $t_{\rm q}$. The small anisotropy of the resistivity in the bc-plane on which donor molecules form a two-dimensional layer demonstrates quasi two-dimensionality in the electronic structure for the β'-type salt, while the band structure [21,33]

is effectively half-filled with a one-dimensional Fermi surface because of the influence of the strong dimerization. The magnetic moment per dimer unit is estimated at 1.83±0.05 μ_B from the fitting to the Curie-Weiss law for both salts, indicating the existence of an S=1/2 localized spin per dimer unit. (The expected magnetic moment for S=1/2 with g=2.0023 is given to be 1.73 μ_B. The overestimation of the magnetic moment by ∼0.1 μ_B can be explained to be caused by the inaccuracy in the subtraction of the diamagnetic core susceptibility from the observed susceptibility. We will comment on the overestimation in the later section.)

The strength of the intra-layer exchange interaction can be estimated on the basis of the two-dimensional square-lattice Heisenberg antiferromagnet model [5] if we assume that the difference between J_b and J_c is neglected. The fitting of the susceptibility vs temperature plot to the model gives $J(=J_b \approx J_c)$∼–59 K for both ICl_2 and $AuCl_2$ salts as shown in Figs. 3.2(a) and 3.3(a). The estimation of the intra-layer interaction is possible also using the value of the perpendicular susceptibility at 0 K, $\chi_\perp(0)$. According to the spin wave theory [9] (see § 1.3.6), $\chi_\perp(0)$ is expressed as

$$\chi_\perp(0) \approx \chi_\perp^0[1 - \Delta S/S - e(0)/2zS], \tag{4.1}$$

for a two-dimensional square-lattice system when $H_A \ll H_E$ where H_A is the magnetic anisotropy field and H_E is the exchange field. $\chi_\perp^0$ is the temperature-independent perpendicular susceptibility based on the molecular field theory, $\chi_\perp^0 = Ng^2\mu_B^2/4zJ$. The estimation [53] based on the Eq. (4.1) gives a value of the intra-layer exchange interaction $J \approx -50$ K for both salts using the values of $\Delta S/S$=0.394, $e(0)$=0.632, z=4, and the experimental values of $\chi_\perp(0) \approx 0.9 \times 10^{-3}$ emu/mol from Figs. 3.2(b) and 3.3(b), in good quantitative agreement with J=–59 K estimated from the high temperature region.

Next, we discuss the spin flop transition field H_{sf} which is expressed as $H_{sf} \approx \sqrt{2H_AH_E}$ on the basis of the molecular field approximation sufficiently below T_N (see § 1.2.6). We obtain the ratio $H_A/H_E \approx 2.0 \times 10^{-5}$ and then $H_A \approx 3$ mK using the observed values of H_{sf}=11 kOe and $H_E = 2zJS/g\mu_B \approx 1.75$ MOe where we employ J=–59 K and g=2.006 estimated from ESR for both salts. This value of H_A is in good agreement with that obtained in the antiferromagnetic resonance measurements (H_A=7–14 mK) [38] which originates mainly from the dipole-dipole interaction. The difference in the Néel temperatures between the two salts (22 K for the ICl_2 salt and 28 K for the $AuCl_2$ salts is considered to be caused by the difference in the inter-layer exchange interaction J'. The Green function method [8] is available for the estimation of the inter-layer exchange interaction in an S=1/2 quasi two-dimensional square-lattice system as mentioned in § 1.3.5. Equation (1.38) gives $J'/J \approx 1 \times 10^{-4}$ for the ICl_2 salt and 1×10^{-3} for the $AuCl_2$ salt, respectively, using the value of the intra-layer exchange interaction J=–59 K and the observed values of the Néel temperatures. The origin of the large difference in the inter-layer exchange interactions for the two salts is reasonably understood from the difference in the layer stacking structure between the large ICl_2^- and small $AuCl_2^-$

Table 4.1: Cell constants of β'-(BEDT-TTF)$_2$X (X=ICl_2, $AuCl_2$) after Refs. [21,33]. $\Delta l/l$ is the relative difference in the cell constant of the $AuCl_2$ salt from that of the ICl_2 salt.

	a(inter-layer)	b(intra-layer)	c(intra-layer)
ICl_2 salt (Å)	12.937	9.780	6.636
$AuCl_2$ salt (Å)	12.766	9.763	6.640
$\Delta l/l(l = a, b, c)$ (%)	1.32	0.17	–0.06

anions. There is almost no difference in the cell constants for the b- and c-axes between the two salts as shown in Table 4.1, which is consistent with the same value of the intra-layer exchange interaction J (≈ -59 K) between the two salts. In the meantime, the difference in the cell constants for the a-axis corresponding to the inter-layer distances is one order of magnitude larger than that in the b- or c-axis. Hence, the difference in T_N between the two salts is suggested to be caused by the difference in the inter-layer distances, implying that the inter-layer interaction (J') originates from exchange interactions since only a small change in the lattice constant ranging $\sim$ 1 % varies the strength of the interaction by one order of magnitude.

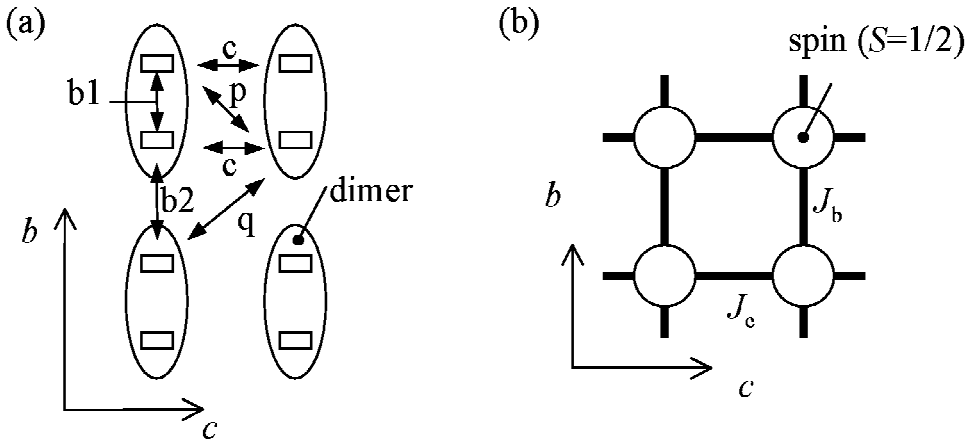

Figure 4.1: Schematic structure of β'-(BEDT-TTF)$_2$X (X=ICl_2, $AuCl_2$). (a) A rectangle represents a BEDT-TTF molecule viewed along the molecular long axis and an ellipsoid circling two molecules represents a dimer unit, where the transfer integrals are given as follows: t_{b1}=27.2 (26.4), t_{b2}=10.0 (10.0), t_p=6.6 (6.5), t_q=–1.6 (–2.0), and t_c=1.6 (2.3)$\times 10^{-2}$ eV for the ICl_2 ($AuCl_2$) salt. (b) Magnetic structure predicted from Fig. 4.1(a). A circle represents a magnetic unit consisting of a donor dimer with an S=1/2 spin and a line linking the circles represents an exchange interaction J.

4.2 Two-leg ladder antiferromagnet of (BEDT-TTF)$_2$GaCl$_4$

The crystal structure of (BEDT-TTF)$_2$GaCl$_4$ [39] shown in Fig. 4.2(a) contains two kinds of dimer units consisting of molecules A-B and C-D coupled through the intra-dimer transfer integrals $t_{\rm intra} = t_{\rm b3}$ and $t_{\rm b1}$, respectively. Strong dimerization, which is evidenced by the considerably large intra- to inter-dimer transfer integral ratio $t_{\rm b3}/t_{\rm p3}$=5.3, $t_{\rm b1}/t_{\rm p1}$=2.8, produces an effectively half-filled band structure similar to that of β'-(BEDT-TTF)$_2$X (X=ICl$_2$, AuCl$_2$). The magnetic moment of 1.79 $\mu_{\rm B}$ per formula unit, thus, indicates that one localized electron is allotted to a dimer unit. From the crystal structure of (BEDT-TTF)$_2$GaCl$_4$, the magnetic structure can be predicted along the same way as the β'-salts as exhibited in Fig. 4.2(a). The dimers form two kinds of one-dimensional chains along the c-axis through $J_{\rm c}$ (consisting of the inter-dimer transfer integrals $t_{\rm c4}$, $t_{\rm c1}$ and $t_{\rm p1}$) and $J'_{\rm c}$ ($t_{\rm c2}$, $t_{\rm c3}$ and $t_{\rm p3}$) where the ratio of the strengths is estimated at $J'_{\rm c}/J_{\rm c} \approx 0.65$. There are four kinds of inter-chain interactions, $J_{\rm p}$ ($t_{\rm p4}$), $J'_{\rm p}$ ($t_{\rm p2}$), $J_{\rm b}$ ($t_{\rm b4}$), and $J'_{\rm b}$ ($t_{\rm b2}$), whose strengths are estimated at $J_{\rm p} \approx 0.13J_{\rm c}$, $J_{\rm b} \approx 0.07J_{\rm c}$, $J'_{\rm p} \approx 0.02J_{\rm c}$, and $J'_{\rm b} \approx 0.08J_{\rm c}$. Thus, (BEDT-TTF)$_2$-GaCl$_4$ forms a quasi one-dimensional structure with alternating inter-chain interactions as shown in Fig. 4.2(b). Here, if we neglect the second nearest and further inter-chain interactions, the magnetic lattice is approximated to a two-leg-ladder structure similar to λ-(BETS)$_2$GaX$_z$Y$_{4-z}$ (X, Y = F, Cl, Br) [54]. To estimate the exchange interaction, first, we employ the one-dimensional Heisenberg antiferromagnet model [3] with neglecting all the inter-chain interactions. The fitting with this model for the temperature dependence of the susceptibility gives the intra-chain exchange interaction J=–70 K (solid curve in Fig. 3.11) above the temperature at which a susceptibility hump appears, while the fitting curve deviates from the experimental result below 60 K approaching zero as $T \to 0$ K. Although the previous report [39] suggests the presence of a three-dimensional antiferromagnetic ordering based on the finite susceptibility extrapolated to 0 K ($\sim 4\times10^{-4}$ emu/mol), it is doubtful due to the serious influence of magnetic impurities at low temperatures. The present result clearly reveals that the magnetic ground state is the spin-singlet one, suggesting the importance of the alternation in the strengths of the inter-chain exchange interactions since a spin gap is opened in one-dimensional chains connected by alternating inter-chain interaction whose extreme is characterized as a two-leg-ladder system. Therefore, not only the β'-salts also (BEDT-TTF)$_2$GaCl$_4$ can be described as a strong dimerization system, where the absence of three-dimensional long-range order in (BEDT-TTF)$_2$GaCl$_4$ is considered to be associated with the specific exchange interaction network of a spin-ladder system in contrast with the three-dimensional antiferromagnetic ordering of the β'-salts.

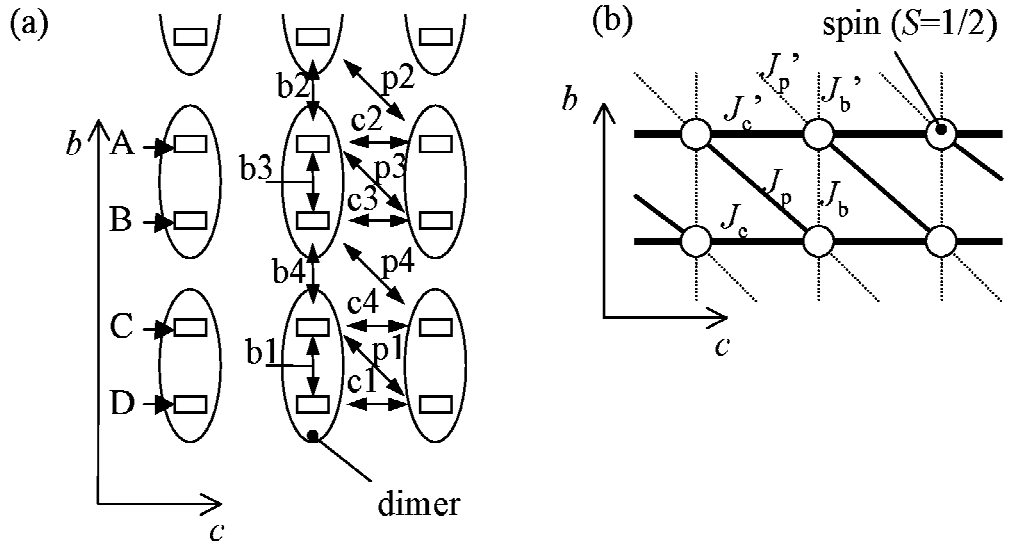

Figure 4.2: Schematic structure of $(BEDT\text{-}TTF)_2GaCl_4$. (a) A rectangle represents a BEDT-TTF molecule (A, B, C, and D) viewed along the molecular long axis and an ellipsoid circling two molecules represents a dimer unit, where the transfer integrals are given as follows: t_{b1}=22.4, t_{b2}=3.69, t_{b3}=26.9, t_{b4}=3.55, t_{c1}=–0.80, t_{c2}=2.86, t_{c3}=2.63, t_{c4}=–4.20, t_{p1}=8.02, t_{p2}=1.96, t_{p3}=5.04, and t_{p4}=4.71×10^{-2} eV. (b) Magnetic structure predicted from Fig. 4.2(a). A circle represents a magnetic unit consisting of a dimer with an S=1/2 spin and a line linking the circles represents an exchange interaction J, where the strengths of the interactions are on the order of bold solid line>thin solid line>dotted line.

4.3 Quasi one-dimensional alternating chain AF structure of α'-(BEDT-TTF)$_2$IBr$_2$

In contrast with β'-(BEDT-TTF)$_2$X (X=ICl$_2$, AuCl$_2$) and (BEDT-TTF)$_2$GaCl$_4$, the degree of dimerization is very weak in α'-(BEDT-TTF)$_2$IBr$_2$ [41] which consists of two independent molecules A and B, since the largest transfer integral ($t_{\rm b2}$) is only 17 % larger than the second largest one ($t_{\rm b1}$) as shown in Fig. 4.3(a). Consequently, the intra-dimer transfer integral is not large enough to open a gap between the upper and lower bands. In other words, the 3/4-filled band structure does not form an effectively half-filled band different from that of β'-(BEDT-TTF)$_2$ICl$_2$, and thus this compound is not a simple Mott insulator. This means that electrons are not well localized in the dimers, that is, electrons are delocalized to some extent as evidenced by the low resistivity ranging $\sim$0.5 - cm at room temperature. The fractional magnetic moment, which is evidenced by the considerably small magnetic moment of 1.60$\pm$0.05 $\mu_{\rm B}$ per formula unit compared with that expected for S=1/2, is favorable to the feature of the delocalized electronic structure. Here, we treat the experimental results on the basis of the localized electron model in order to see the statistical dynamics behavior of the magnetic system, although the employment of itinerant electron model seems to be more appropriate. The dimer units are networked as shown in Fig. 4.3(a) mainly through $t_{\rm b1}$, $t_{\rm b3}$, $t_{\rm b4}$, and $t_{\rm a1}$, where the strongest inter-dimer interaction $J_{\rm b}$ consists of $t_{\rm b1}$ and $t_{\rm a3}$, and the second strongest one $J'_{\rm b}$ consists of $t_{\rm b4}$ and $t_{\rm a1}$, where the estimation gives $J'_{\rm b}/J_{\rm b} \approx 0.77$. The inter-chain interaction $J_\perp$ is estimated at $J_\perp \approx 0.16 J_{\rm b}$ where we take only $t_{\rm b3}$ as the main contribution to $J_\perp$. Therefore, a quasi one-dimensional alternating chain structure is formed along the b-axis as shown in Fig. 4.3(b). The broad peak of the susceptibility shown in Fig. 3.16 is explained by the one-dimensional chain model with the alternating exchange interactions [6] J and J' where the fitting of the data gives J=–53 K and J'=–26 K (J'/J=0.5). The estimated ratio of J'/J is in roughly quantitative agreement with that calculated from the transfer integrals. The absence of three-dimensional long-range ordering in α'-(BEDT-TTF)$_2$IBr$_2$ can be explained to be associated with the alternation in the strengths of the intra-chain exchange interactions along the b-axis which brings about the dimerization of the spins sitting on adjacent two dimer units.

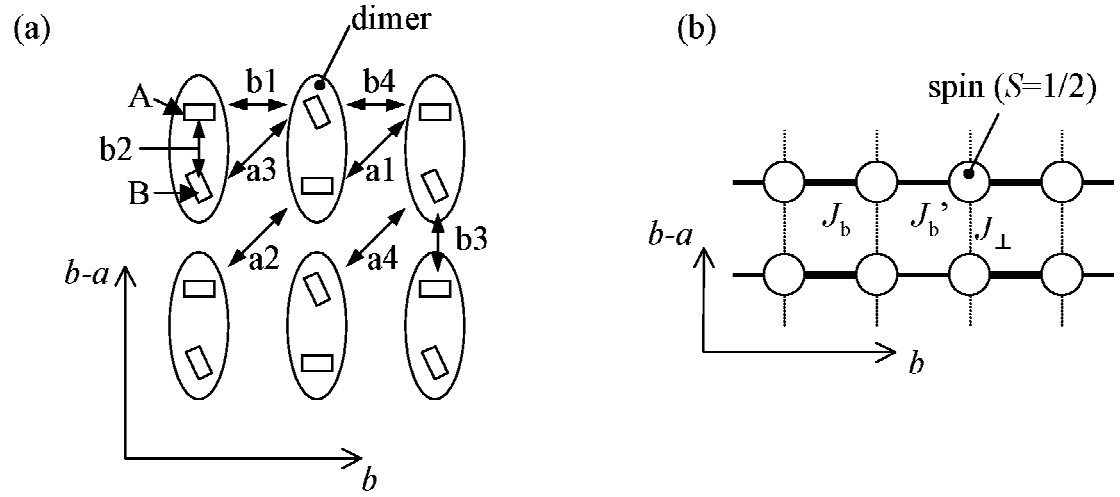

Figure 4.3: Schematic structure of α'-(BEDT-TTF)$_2$IBr$_2$. (a) A rectangle represents a BEDT-TTF molecule (A and B) viewed along the molecular long axis and an ellipsoid circling two molecules represents a dimer unit, where the transfer integrals are given as follows: t_{a1}=4.02, t_{a2}=0.78, t_{a3}=2.30, t_{a4}=1.11, t_{b1}=–7.72, t_{b2}=9.04, t_{b3}=7.16, and t_{b4}=–5.79$\times 10^{-2}$ eV. (b) Magnetic structure predicted from Fig. 4.3(a). A circle represents a magnetic unit consisting of a dimer with an S=1/2 spin and a line linking the circles represents an exchange interaction J, where the strengths of the interactions are on the order of bold solid line>thin solid line>dotted line.

4.4 Quasi one-dimensional AF structure of (EDO-TTFBr$_2$)$_2$-AsF$_6$

Figure 4.4(a) shows the schematic structure of the donor molecule arrangement. The transfer integrals t_{c1} and t_{c2} form the one-dimensional stacking structure along the c-axis. The intra-dimer transfer integral t_{c1} is considerably large compared with that of β'-(BEDT-TTF)$_2$ICl$_2$, whereas the ratio between the intra-dimer and the largest inter-dimer transfer integral t_{c2} is t_{c1}/t_{c2}=1.3. Therefore, the dimerization is considered to have an intermediate strength between the strong dimerization of β'-(BEDT-TTF)$_2$ICl$_2$ and the weak dimerization of α'-(BEDT-TTF)$_2$IBr$_2$. The other transfer integrals, t_a, t_p, and t_q, that are characterized with the side-by-side inter-molecular atomic contacts, are an order of magnitude weaker than the intra-chain transfer integrals. Thus the magnetic structure based on the dimer unit is expected to be a quasi one-dimensional structure as shown in Fig. 4.4(b).

The susceptibility, which has a value of about 5.5×10^{-4} emu/mol at room temperature, gradually decreases as the temperature is lowered from room temperature. This behavior can not be fitted to the Curie-Weiss law. Thus we fit the temperature dependence of the susceptibility above ~100 K to the one-dimensional Heisenberg antiferromagnet model as depicted with the solid curve of Fig. 3.22. The result of the fitting gives an intra-chain exchange interaction of J=–190±25 K with an magnetic moment of 1.74 μ_B which corresponds to an S=1/2 spin with g=2.006 per formula unit. The fitting indicates a good agreement with the experimental data, therefore, the experimental finding suggests the existence of an S=1/2 spin per dimer unit, where the antiferromagnetic exchange interaction ranging about 200 K works between localized spins. The strong exchange interaction is explained by the large value of the dominant inter-dimer transfer integral t_{c2} (= 208 meV) which connects two dimer units one-dimensionally along the c-axis.

The temperature dependence of the ESR intensity is qualitatively consistent with the static susceptibility at high temperatures, however the ESR signal disappears below 37 K accompanied by a divergent upturn of the line width. Additionally the g-value is shifted down steeply just above 37 K, and thus the ESR experimental results are considered to imply the onset of an antiferromagnetic ordering at T_N=37 K. On the other hand, the susceptibility shows no anisotropy between the applied field parallel and perpendicular to the c-axis. That is to say, the susceptibility behaves as if the field is applied parallel to the spin hard-axis regardless of the actual field direction. Moreover, no spin flop behavior is observed in the magnetization curve up to 55 kOe below T_N although most of the TTF-based π-electron antiferromagnets having even been investigated have spin flop transitions below 55 kOe. At the present time, we consider two alternative explanations for the absence of anisotropy in the susceptibility. First one is an experimental reason that the large contribution of the Curie

term of the magnetic impurity conceals the spin easy-axis[1]. Second reason is the intrinsic one, where the small anisotropy field contributes to the absence of both the spin flop transition and of the disappearance of the spin easy-axis. For the purpose of the verification of the small anisotropy in the magnetic susceptibility, we try to explain the angular dependence of the ESR line width whose origin might be related to the anisotropy of the magnetic susceptibility. The second moment of the magnetic dipole-dipole interaction based on a point-dipole model where the dipole moments are arranged in the three-dimensional lattice points. The numerically calculated result is shown in Fig. 4.5. If the anisotropy is governed by the dipole-dipole interaction, the angular dependence of the ESR line width will be qualitatively described by the second moment of the dipole-dipole interaction. Compared with Fig. 3.23, however, the line width obtained by the second moment is much larger than the experimental value of $\sim$ 20 Oe, and the angular dependence is quite different from each other. This inconsistency demonstrates that the contribution of the anisotropic exchange interaction competing with the dipole-dipole interaction makes the anisotropy be offset, and thus the easy-axis can not be detected.

Although we do not determine the origin of the disappearing easy-axis, the finite susceptibility will be attributed to the perpendicular susceptibility in the antiferromagnetic ordering state below 37 K. The value extrapolated to 0 K is estimated at $\sim 4 \pm 1 \times 10^{-4}$ emu/mol. For low-dimensional systems of a quantum spin S=1/2, the perpendicular susceptibility at the absolute zero temperature reflects the spin reduction effect from the expected value of $\langle S \rangle$=1/2, as mentioned in § 1.3.6. In this case with $H_{\rm A} \ll H_{\rm E}$, a relation described in Eq. (1.44) gives the value of the inter-chain exchange interaction $J \approx -150 \pm 50$ K, using the values of $\Delta S/S$=0.350 [9], $e(0)$=0.69, z=2, and the experimental values of $\chi_{\perp}(0) \approx 4 \pm 1 \times 10^{-4}$ emu/mol. The obtained value of J is in good quantitative agreement with $J \approx -190$ K estimated from the higher temperature region.

[1] A considerably small spin flop-like behavior has been observed around 30 kOe in a magnetization curve at 2 K in the field perpendicular to the c-axis, while the reexamination is needed to conclude.

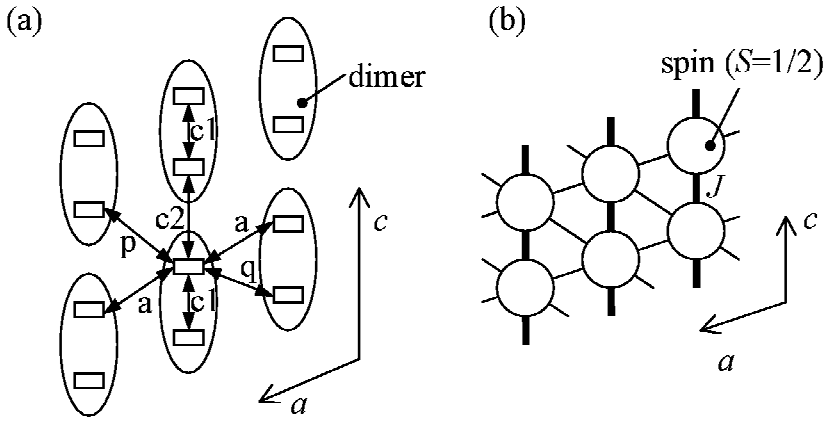

Figure 4.4: Schematic structure of $(EDO\text{-}TTFBr_2)_2AsF_6$. (a) A rectangle represents a BEDT-TTF molecule viewed along the molecular long axis and an ellipsoid circling two molecules represents a dimer unit, where the transfer integrals are given as follows: t_{c1}=27.5, t_{c2}=20.8, t_a=3.85, t_p=1.24, and t_q=-2.44×10^{-2} eV. (b) Magnetic structure predicted from Fig. 4.4(a). A circle represents a magnetic unit consisting of a dimer with an S=1/2 spin and a line linking the circles represents an exchange interaction J, where the strengths of the interactions are on the order of bold solid line>thin solid line.

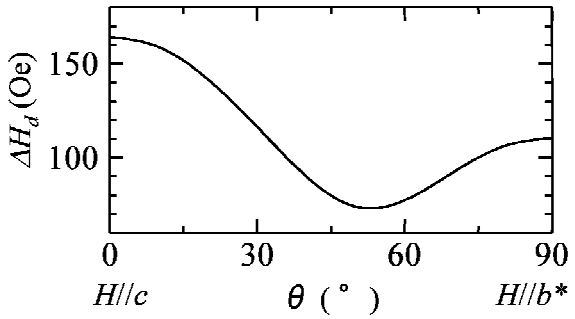

Figure 4.5: Angular dependence of the dipolar ESR line width calculated based on the point dipole model for $(EDO\text{-}TTFBr_2)_2AsF_6$.

4.5 Quasi one-dimensional AF structure with frustration effect in the 3:1 Salts

The schematic structure is shown in Fig. 4.6(a) for (BMDT-TTF)$_3$ClO$_4$(1,2-dichloroethane) [42, 43] and (BMDT-TTF)$_3$AsF$_6$(1,1,2-trichloroethane) [53] which contains two independent BMDT-TTF molecules A and B on the *ac*-plane. The largest transfer integral t_{c3}, which is only 22 % and 25 % larger than the second largest one t_{c2}, for the ClO$_4$ and AsF$_6$ salts, respectively, gives weakly trimerized units comprising one A molecule and two B molecules. The intra-trimer interaction comparable to the inter-trimer interaction seems to bring inappropriateness in the treatment with a trimer-based system, however we try to explain the magnetic structure based on the trimer unit. The weakness of the trimerization seems not to give an effectively half-filled band, suggesting a deviation from a simple Mott insulator system, similar to α'-(BEDT-TTF)$_2$IBr$_2$ having small fractional magnetic moments. On the contrary, the experimental finding that the 3:1 salts have the magnetic moment of about 1.8 μ_B per formula unit indicates the localization of an electron within a trimer. A clue to achieve a consistency between the opposite trends consists in a specific charge distribution in the donor network. The crystal structure analysis [42, 43] proves the presence of charge disproportionation between A^+ and B^0 donor molecules in the ClO$_4$ salt. This means that the inter-site Coulomb interaction works to make electrons apart from each other to achieve the energy stabilization, as discussed in the previous report [43]. Therefore, the contribution of the inter-site Coulomb interaction allows us to treat the ClO$_4$ salt as a localized spin system. In the meantime, the AsF$_6$ salt has no charge disproportionation between the two independent donors A and B, suggesting the delocalization of charges among donors in a trimer unit which is favorable to the experimental finding in the ESR spectra as discussed in the later section.

The observed value $\sim$1.8 μ_B of the magnetic moment per trimer seems to be inconsistent with such delocalized electronic feature. However, there is a suggestive feature related to an electron delocalization-to-localization change in the susceptibility. The AsF$_6$ salt undergoes successive phase transitions around 150K and $\sim$200–290 K with a large hysteresis from a high-temperature conductive state to a low-temperature less conductive state, where the application of pressure makes the high temperature phase metallic. The behavior of the susceptibility shown in Fig. 3.35 reflects the transition as evidenced by the presence of a kink in the Curie-Weiss plot. As shown in Fig. 3.35, the magnetic moment above the phase transition at $T_c \approx 150$ K is about 2 % smaller than that below T_c, the latter of which has the same value to the magnetic moment of the ClO$_4$ salt. The reduced magnetic moment above T_c is considered to be associated with the delocalized feature of the electrons. Taking into account the importance of the inter-site Coulomb interaction in the ClO$_4$ salt, the AsF$_6$ salt, which has the same crystal structure, is expected to have the similar role of the inter-

site Coulomb interaction, especially, in the low temperature phase, which eventually makes electrons localized within trimers similar to the ClO_4 salt.

We discuss the magnetic structure on the basis of the localized spin model, in which the crystal structure at room temperature is taken into account. Considering a trimer as a magnetic unit, the trimers interact with each other along the c-axis through J_c (consisting of t_{c1} and t_{a1}) and then along the a-axis through J_a (t_{c2} and t_{a2}) where $J_a/J_c \approx (|t_{a2}|+|t_{c2}|)^2/(|t_{c1}|+|t_{a1}|+|t_{c1}|)^2 \approx 0.36$ and 0.47 for the ClO_4 and AsF_6 salts, respectively. Accordingly, the structural feature based on the trimer unit is described as the J_c-dominated one-dimensional chain structure with inter-chain interactions J_a as shown in Fig. 4.6(b) where the participation of J_a adds a frustration feature to the exchange interaction network. In the ClO_4 salt, the fitting of the susceptibility to the S=1/2 one-dimensional Heisenberg antiferromagnet model [3] gives the exchange interaction J=–37 K over the whole temperature range measured, as shown in Fig. 3.28, with neglecting the contribution of J_a. The absence of an antiferromagnetic transition observed for the ClO_4 salt is caused by the frustration introduced by the strong inter-chain exchange interactions. For the AsF_6 salt, the similar estimate of the exchange interaction gives $J \approx -11$ K in the temperature range between 2–60 K. Thus, the experimental results indicate a large difference in the exchange interactions between the two salts. The phase transition at $T_c \approx 150$ K, which makes the value of the magnetic moment increase to that expected for an S=1/2 per trimer below T_c, is considered to result in the localization of the electrons, reducing the inter-trimer transfer integrals and eventually the strengths of the exchange interactions, although the crystal structure analysis in the low temperature range is required for a final conclusion.

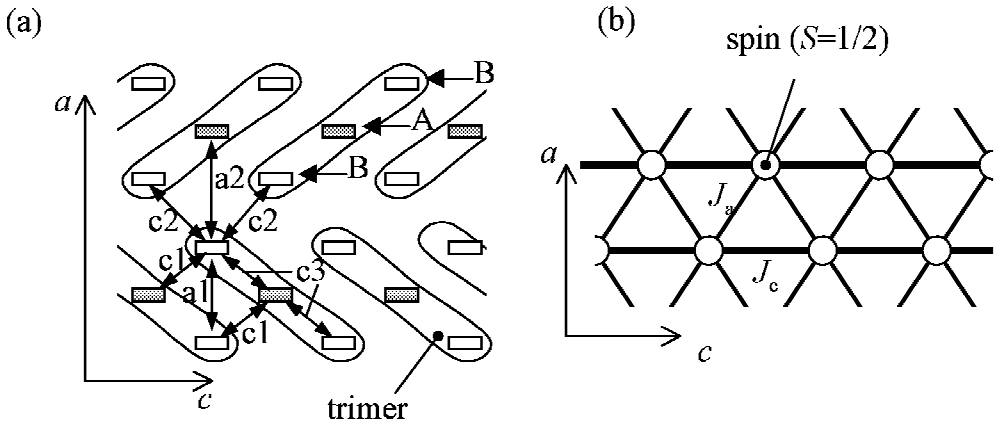

Figure 4.6: Schematic structure of (BMDT-TTF)$_3$ClO$_4$(1,2-dichloroethane) and (BMDT-TTF)$_3$AsF$_6$(1,1,2-trichloroethane). (a) A rectangle represents a BMDT-TTF molecule (A and B) viewed along the molecular long axis and an ellipsoid circling three molecules represents a trimer unit, where the transfer integrals are given as follows: t_{a1}=–6.22 (–5.58), t_{a2}=–5.52 (–6.88), t_{c1}=–11.2 (–10.2), t_{c2}=11.6 (11.0), and t_{c3}=14.1 (13.7)$\times 10^{-2}$ eV for the ClO_4 and AsF_6 salts, respectively. (b) Magnetic structure predicted from Fig. 4.6(a). A circle represents a magnetic unit consisting of a trimer with an S=1/2 spin and a line linking the circles represents an exchange interaction J, where the strengths of the interactions are on the order of bold solid line>thin solid line.

4.6 ESR line width and the electron localization

The ESR line width is a good indicator for characterizing the magnetic structure and the electron transport process. The spin-spin relaxation, which is one of the origin of the ESR line width, is governed by the dipole-dipole interaction where the line width associated with this process is subjected to the exchange-narrowing mechanism in an exchange-interaction-networked localized spin system. Meanwhile, the contribution of the spin-lattice relaxation becomes dominant in the line width of the delocalized electron system, which is related to the relaxation time of carriers in the conduction process, since the rapid motion of the carriers makes the width of the spin-spin relaxation completely disappear due to the motional narrowing process. Actually, in most of metallic charge transfer salts having ever been investigated [26,30,55], the line width is predominated by the spin-lattice relaxation process of carriers while complexes in the localized regime have an important contribution of the spin-spin relaxation to the line width as will be shown in this section. Here, we investigate the feature of the ESR line width in relation to the strength of dimerization/trimerization of donors, which is considered to be responsible for the electron localization.

First we discuss the correlation between the line width and the degree of electron delocalization in the 2:1 salts. β'-(BEDT-TTF)$_2$ICl$_2$ and (BEDT-TTF)$_2$GaCl$_4$ [39], that are typical strong dimerization systems, have narrow ESR line widths of $\sim$10 Oe at room temperature. The well localized electronic structures of these salts are characterized to be Mott insulators as evidenced by the poor electrical conductivity ($\sigma \approx$0.05–0.1 S/cm) and the less temperature dependent large thermoelectric powers ranging 100–400 μV/K at room temperature. Figure 4.7 shows the correlation between the line width and the χT product [37,39], based on the spin-diffusion theory of the spin-spin relaxation mechanism in the low-dimensional magnets where the combination of the dipole-dipole and exchange interactions makes the line width be proportional to χT at high temperatures above the temperature at which the thermal energy becomes comparable to the exchange interaction. The temperature dependence of the line widths for β'-(BEDT-TTF)$_2$ICl$_2$ and (BEDT-TTF)$_2$GaCl$_4$ have almost the same behavior to that of the χT products, which means that the dipole-dipole interaction and the exchange interaction related to the χT product plays the major role in the behavior of the line width. Thus, this ESR behavior of the salts having strong dimerization suggests self-consistency between the localized spin feature in the magnetic structure and their spin dynamics. On the other hand, α'-(BEDT-TTF)$_2$IBr$_2$ having less dimerized structural feature [41] is a great contrast to β'-(BEDT-TTF)$_2$ICl$_2$ and (BEDT-TTF)$_2$GaCl$_4$. The delocalized electronic feature in α'-(BEDT-TTF)$_2$IBr$_2$ is obvious from the low resistivity $\sim$0.5 - cm and the small thermoelectric power $\sim$+25 μV/K. Its remarkably broad line width $\sim$60 Oe is in the similar range to that of typical metallic BEDT-TTF complexes [26, 30, 55], and the temperature dependence of the line width [37] shown in Fig. 4.7(c) reveals a considerable difference from that of the χT product. Actually, a large deviation appears at lower temperatures though

the χT product apparently seems to be similar to that of the line width above ~150 K except the broadness of the line width. As a consequence it is suggested that the line width of α'-(BEDT-TTF)$_2$IBr$_2$ is strongly influenced by the spin-lattice relaxation process. These features in α'-(BEDT-TTF)$_2$IBr$_2$ with weak dimerization are considered to be generated by the delocalization of the electrons, giving the contribution of the spin-lattice relaxation to the line width similar to metallic compounds.

The same comparison between the ESR line width and the χT product for (EDO-TTFBr$_2$)$_2$AsF$_6$ is shown in Fig. 4.7(d). Taking account of the the remarkably high conductivity even in the semiconducting state ($\sigma \approx 20$ S/cm at room temperature), the excellent correlation between the line width and χT in Fig. 4.7 is apparently exceptional and puzzling. However, if we pinpoint the dimensionality in the electronic structure of (EDO-TTFBr$_2$)$_2$-AsF$_6$, the exceptional feature in the correlation can be explained on the basis of the above discussion. The transfer integrals obtained for (EDO-TTFBr$_2$)$_2$AsF$_6$ gives an estimate of the intra-to-inter-chain transfer integral ratio of 5.4, which is the largest among the salt investigated here. From the ratio, (EDO-TTFBr$_2$)$_2$AsF$_6$ is considered to have a almost pure to the one-dimensional electronic feature. According to the spin-lattice relaxation theory [56], no spin-lattice relaxation process is allowed in ideal one-dimensional conductors. Eventually, the excellent correlation is achieved because of the negligible contribution of the spin-lattice relaxation process.

The ESR line width in the 3:1 salts is suggestive from the viewpoint of electron localization/delocalization. Figure 4.8 shows the temperature dependence of the line width for the 3:1 salts in comparison with the χT product. There is a large difference in the behavior of the temperature dependence of the ESR line width between the ClO_4 and AsF_6 salts, whereas the absolute values of ~10 Oe are in the same range to those of the localized spin systems of the 2:1 salts. The line width in the ClO_4 salt is subjected to the spin-spin relaxation process as suggested by the similarity in the temperature dependence between the line width and χT, which is a good indication that the spin system has a well localized feature. The behavior of the AsF_6 salt is not explained simply by the feature of the localized spin system, especially the behavior in the high temperature phase above $T_c \approx 150$ K. Namely, the temperature dependence above T_c seems to have an additional contribution although the line width has the similar temperature dependence to that of χT below T_c. Taking account of the delocalized feature of the electrons in the trimer for the AsF_6 salt, which is deduced from the room temperature crystal structure, the additional contribution is considered to reflect the spin-lattice relaxation process of the mobile π-electrons. This is consistent with the change in the value of the magnetic moment at T_c.

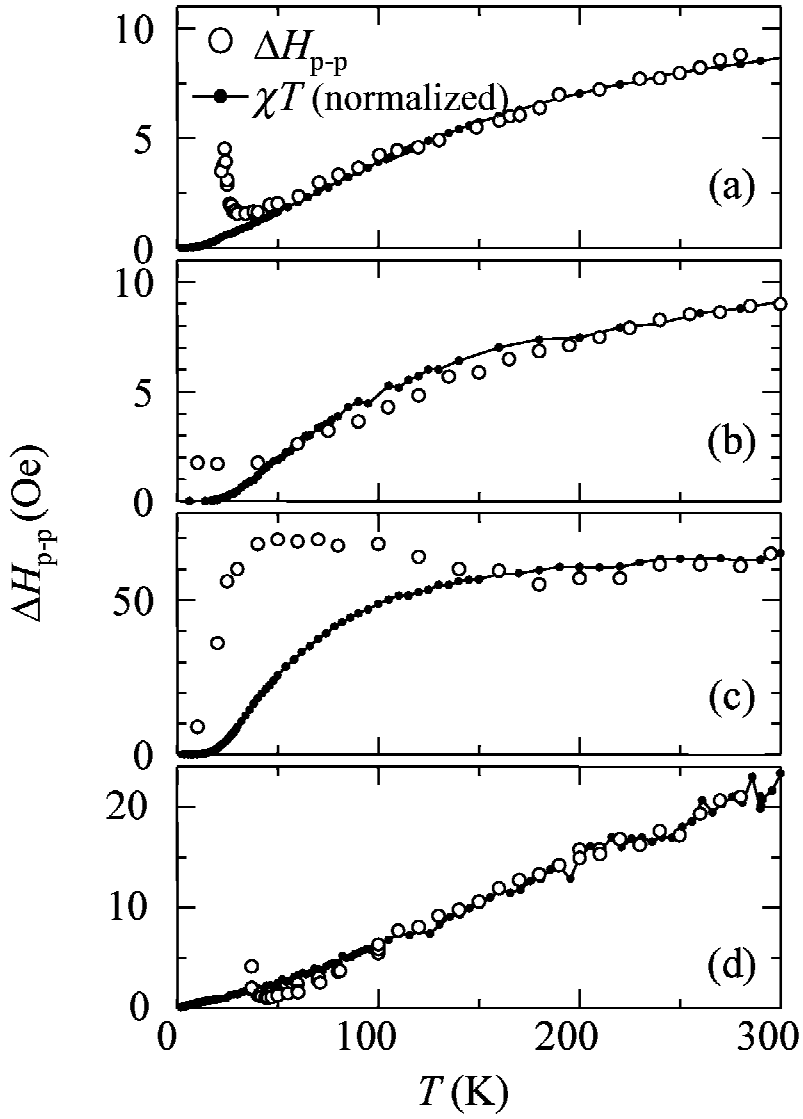

Figure 4.7: Correlation between ESR line width (open circle) and the normalized χT plot (closed circle) for (a) β'-(BEDT-TTF)$_2$ICl$_2$, (b) (BEDT-TTF)$_2$GaCl$_4$, (c) α'-(BEDT-TTF)$_2$-IBr$_2$, and (d) (EDO-TTFBr$_2$)$_2$AsF$_6$, which are normalized to each room temperature values of $\Delta H_{\text{p-p}}$. The ESR data for (BEDT-TTF)$_2$GaCl$_4$ and α'-(BEDT-TTF)$_2$IBr$_2$ are quoted after Refs. [37, 39], respectively.

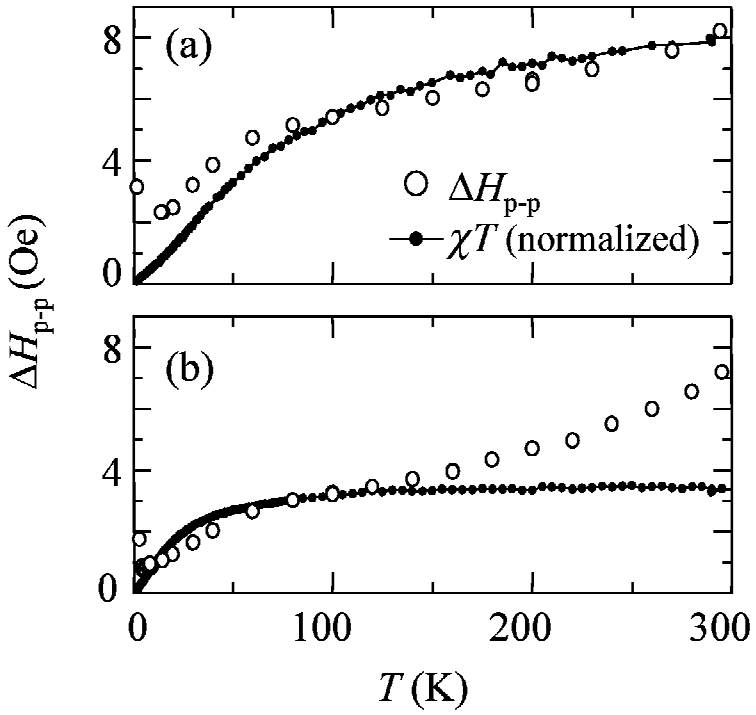

Figure 4.8: Correlation between ESR line width and the normalized χT plot for (a) (BMDT-TTF)$_3$ClO$_4$(1,2-dichloroethane) and (b) (BMDT-TTF)$_3$AsF$_6$(1,1,2-trichloroethane). The χT product are normalized to the value at room temperature and 100 K for the ClO$_4$ and AsF$_6$ salt, respectively.

4.7 Strength of dimerization/trimerization and magnetic interaction

In the previous sections, we discussed six kinds of the magnetic structures and the feature of the ESR line width on the basis of a dimer/trimer unit to which an S=1/2 spin is allotted. From the structural aspect, β'-(BEDT-TTF)$_2$X (X=ICl$_2$, AuCl$_2$) and (BEDT-TTF)$_2$GaCl$_4$ are characterized well in terms of strong dimerization in contrast with the other three salts where the dimer/trimer model is not so appropriate. Nevertheless, the dimer/trimer-based magnetic structures well explain the experimental results for all the salts investigated, which indicates the validity of the employed model, especially from the viewpoint of statistical mechanics of localized spin systems. To see more details in the difference between the salts with strong and weak dimerization/trimerization, we discuss the relationship between the exchange interactions and the transfer integrals. Table 4.2 summarized the exchange interactions, the Weiss constants and the representative transfer integrals for all the salts investigated. Here, $J_{\rm exp}$ and $\Theta_{\rm exp}$ are the exchange interactions estimated from the low-dimensional magnet models and the Weiss constants estimated experimentally, respectively. $\Theta_{\rm MF}$ is calculated from $\Theta_{\rm MF}$=(1/2)$\sum J_{\rm exp}$ on the basis of the molecular field theory with S=1/2 where the summation is carried out over all the nearest neighbor spins as shown in Fig. 4.2. The obtained values of $\Theta_{\rm MF}$ are in good agreement with the experimental data, $\Theta_{\rm exp}$, suggesting the appropriateness of the data treatments at high temperatures. $t_{\rm intra}$ is the intra-dimer/trimer transfer integrals. Here, we introduce $t_{\rm eff}$ as a parameter representing an effective transfer integral between adjacent two spins in the expression of the exchange interaction between the dimer/trimer units given by $J \approx -t_{\rm eff}^2/U_{\rm eff}$. $U_{\rm eff}$ in the dimer-based systems is obtained from the following equation as discussed in § 1.1.3,

$$U_{\rm eff} = 2|t_{\rm intra}| + \left[U_0 - \sqrt{U_0^2 + 16t_{\rm intra}^2}\right]/2, \tag{4.2}$$

which is approximated to $U_{\rm eff} \gg 2|t_{\rm intra}|$ in charge transfer salts with strongly dimerized donor structure. The expression of $U_{\rm eff}$ for the trimer system, which is given similar to Eq. 4.2, leads to $U_{\rm eff} \approx \sqrt{2}|t_{\rm intra}|$ for strong trimerization. Thus, we obtain $t_{\rm eff} \approx \sqrt{2|J_{\rm exp}| \cdot |t_{\rm intra}|/\xi}$ as an estimation of the effective $t_{\rm inter}$ working between adjacent spins, as summarized in Table 4.2, where ξ=1 and $\sqrt{2}$ for dimerized and trimerized systems, respectively. It is worth noting that the above treatment with $t_{\rm eff}$ is valid only for the case where a dimerized/trimerized unit is well defined; that is, the intra-dimer/trimer transfer integral is required to be considerably larger than the inter-dimer/trimer transfer integral. From this aspect, the estimated values $t_{\rm eff}$ well reflect the strength of dimerization/trimerization as revealed in Table 4.2. Namely, there is a good correlation between the experimentally obtained Weiss temperatures and the values of $t_{\rm eff}$ in β'-(BEDT-TTF)$_2$X (X=ICl$_2$, AuCl$_2$) and (BEDT-TTF)$_2$GaCl$_4$ having strong dimerization. On the contrary, α'-(BEDT-TTF)$_2$IBr$_2$ have a smaller $t_{\rm eff}$ than that expected

Table 4.2: Exchange interactions, Weiss constants, and transfer integrals. $J_{\rm exp}$: the exchange interactions obtained from the low-dimensional models(see text), $\Theta_{\rm exp}$: the experimental Weiss constants, $\Theta_{\rm MF}$: the calculated Weiss constants from $J_{\rm exp}$ in the molecular field theory, $t_{\rm intra}$: the intra-dimer(trimer) integrals estimated from the overlap integrals, $t_{\rm eff}$: the inter-dimer(trimer) transfer integrals estimated from $J_{\rm exp}$, p: the effective Bohr magnetons per dimer/trimer unit. (BEDT-TTF)$_2$GaCl$_4$ has two kinds of the $t_{\rm intra}$ and $t_{\rm eff}$ for two independent dimer units.

	$J_{\rm exp}$ (K)	$\Theta_{\rm exp}$ (K)	$\Theta_{\rm MF}$ (K)	$t_{\rm intra}$ (eV)	$t_{\rm eff}$ (eV)	p
β'-(BEDT-TTF)$_2$ICl$_2$	–59	–140±20	–118	0.273	0.052	1.83±0.05
(BEDT-TTF)$_2$GaCl$_4$	–70	–110±20	–70	0.269	0.057	1.79±0.05
				0.224	0.052	
α'-(BEDT-TTF)$_2$IBr$_2$	–53	–40±10	–40	0.090	0.028	1.60±0.05
(EDO-TTFBr$_2$)$_2$AsF$_6$	–190	-	–190	0.275	0.095	1.74±0.1
MT$_3$ClO$_4$DCE	–37	–50±10	–37	0.141	0.021	1.85±0.05
MT$_3$AsF$_6$TCE ($T > 150$ K)	-	–15±3	-	0.137	-	1.79±0.05
MT$_3$AsF$_6$TCE ($T < 150$ K)	–11	–23±1	–11	-	-	1.83±0.03

in the case of strong dimerization. (EDO-TTFBr$_2$)$_2$AsF$_6$ has an intermediate strength of the dimerization compared with the other 2:1 salts in this work, whose large value of $t_{\rm eff}$ will come from the strong exchange interaction. Consequently, the diagnosis on the basis of the treatment with transfer integrals $t_{\rm eff}$ gives additional information on the deviation from the purely localized spin model treated by statistical dynamics for the weakly dimerized systems.

The most important feature of the magnetic properties for the salts investigated in this work is reflected by the values of the magnetic moments as summarized in Table 4.2. The magnetic moments of the salts except the α'-(BEDT-TTF)$_2$IBr$_2$ and (EDO-TTFBr$_2$)$_2$AsF$_6$ have larger values than the expected value of 1.73 $\mu_{\rm B}$ for S=1/2 by about 0.1 $\mu_{\rm B}$. This might be associated with the systematic errors coming from the core diamagnetic contributions we employ for the corrections of the core diamagnetism. Assuming that the 0.1 $\mu_{\rm B}$ excess can be subtracted commonly from the observed values of the magnetic moments as an artificially added contribution, the magnetic moment for the α'-(BEDT-TTF)$_2$IBr$_2$ and (EDO-TTFBr$_2$)$_2$AsF$_6$ is considered to have a smaller magnetic moment $\sim$1.5 $\mu_{\rm B}$ and 1.6 $\mu_{\rm B}$ than that expected for S=1/2 due to the electron delocalization. The reduction of the magnetic moment in the high temperature conductive phase on (BMDT-TTF)$_3$AsF$_6$(1,1,2-trichloroethane) ($T >$150 K) is suggestive as well from the point of the electron delocalization.

Chapter 5

Discussion of transport properties

Generally, the temperature dependence of the resistivity for a semiconductor is described as

$$\rho(T) = \rho_0 \exp(\frac{E_a}{k_B T}), \tag{5.1}$$

where E_a is an activation energy and ρ_0 is a temperature-independent prefactor. In the charge transfer salts investigated here, the strongly dimerized salts, such as β'-(BEDT-TTF)$_2$ICl$_2$, show ordinary semiconductive behavior as described in Eq. (5.1), while a weakly dimerized salt, α'-(BEDT-TTF)$_2$IBr$_2$, is not simple in its temperature and/or pressure dependent behavior. Therefore, starting from Eq. (5.1), we discuss the temperature and pressure dependence of the resistivities complementarily for the 2:1 salts on the basis of the strength of the dimerization. In the thermoelectric powers, we consider a model for a strongly correlated electron system with a half-filled electronic state. This model gives a reasonable explanation for the thermoelectric powers in the Mott insulator regime for the strongly dimerized salts, whereas it does not explain the behavior of α'-(BEDT-TTF)$_2$IBr$_2$. Thus, the focus of this discussion is the difference in the transport properties and the electronic structures associated with the strength of the dimerization.

For the 3:1 salts, (BMDT-TTF)$_3$ClO$_4$(1,2-dichloroethane) and (BMDT-TTF)$_3$AsF$_6$(1,1,2-trichloroethane), the transport properties are quite complicated. We discuss mainly the phase transitions indicated in the resistivities for both salts.

5.1 The 2:1 salts

5.1.1 Resistivity

In order to cross-check the data of the pressure and temperature dependence of the resistivity, we simply extend Eq. (5.1) to the expression involving temperature and pressure,

$$\rho(T, P) = \rho_0(P) \exp(\frac{E_a(P)}{k_B T}). \tag{5.2}$$

The results of the resistivity in the high temperature range are summarized in Table 5.1 after the analysis of the resistivities with Eq. (5.2). For the 2:1 salts, two common trends between β'-(BEDT-TTF)$_2$ICl$_2$ and (EDO-TTFBr$_2$)$_2$AsF$_6$ emerge; a small reduction in the activation energies ranging about 30% even under 10 kbar and the pressure-insensitive behavior of the prefactor $\rho_0(P)$, although there is a large error of $\sim$50 % depending on the temperature regions employed for the fitting. In contrast, α'-(BEDT-TTF)$_2$IBr$_2$ shows a large pressure-induced decrease of the activation energy which becomes one order of magnitude smaller at 12 kbar in comparison with that at ambient pressure. Additionally, the value of $\rho_0(P)$ becomes largely different from each other between ambient pressure and 12 kbar.

Contrary, the pressure dependence of the resistivities at room temperature indicates a simple behavior for all the salts as shown in Fig. 5.1. An interesting trend is that the $\log\rho$ vs P plots have linearity with almost the same slope for all the salts. This behavior of $\log\rho$ is considered to be approximately expressed with a linear function of P, that is,

$$\rho(300\mathrm{K}, P) = \rho(300\mathrm{K}, 1\ \mathrm{bar})\exp(-\epsilon P), \tag{5.3}$$

where a fitting parameter ϵ is summarized in Table 5.2. ϵ has almost the same value of about 0.13 (1/kbar) for the 2:1 salts, irrespective of the differences in the crystal and electronic structures.

To clarify the difference between the strong and weak dimer salts, we here put the three kinds of information obtained in order. First the pressure dependence of $\rho(T, P)$ at room temperature does not differ from each other regardless of the strength of the dimerization as described in Eq. (5.3). Second, in the prefactor $\rho_0(P)$, there is no pressure dependence for the strongly dimerized salts, while it increases as the pressure is elevated for the weakly dimerized salt, α'-(BEDT-TTF)$_2$IBr$_2$. Third, the decreasing trend of the activation energy E_a induced by the pressure for the weakly dimerized salt is about one order of magnitude larger than that of the strongly dimerized salts.

We next discuss the activation energy. The pressure dependence of the activation energies around room temperatrue is shown in Fig. 5.2. Neglecting the pressure-dependence of $\rho_0(P)$ below $\sim$ 10 kbar for β'-(BEDT-TTF)$_2$ICl$_2$ and (EDO-TTFBr$_2$)$_2$AsF$_6$, we obtain the following expression of $E_a(P)$ from Eqs. (5.3) and (5.2),

$$E_a(P) \approx \left[-(\epsilon k_\mathrm{B})P + k_\mathrm{B}\ln\frac{\rho(300\ \mathrm{K},\ 1\ \mathrm{bar})}{\rho_0}\right] \times 300\ \mathrm{K}, \tag{5.4}$$

in the temperature range around room temperature, which gives

$$E_a(P) \approx -3\times10^{-3}P + 0.1\ \mathrm{eV}\ \ (P:\mathrm{kbar}), \tag{5.5}$$

at $T\approx$300 K for β'-(BEDT-TTF)$_2$ICl$_2$. The slope of this equation is obtained from the pressure dependence of the resistivity depicted as the solid line without any fitting parameters in

Fig. 5.2(a). This is in good agreement with the experimental data obtained from the temperature dependence of the resistivity. The same treatment is applied to (EDO-TTFBr$_2$)$_2$AsF$_6$, where the corresponding relation is

$$E_a(P) \approx -4 \times 10^{-3} P + 0.12 \text{ eV}, \tag{5.6}$$

which is consistent with the plotted data in Fig. 5.2(b). Thus, the activation energies of the two salts are considered to be well expressed by Eq. (5.2). We apply the similar treatment to α'-(BEDT-TTF)$_2$IBr$_2$, resulting in the relation: $E_a \approx -4 \times 10^{-3} P + 0.22$ eV, which is shown in Fig. 5.2(c). However, this relation for α'-(BEDT-TTF)$_2$IBr$_2$ exhibits disagreement with the data obtained from the temperature dependence of the resistivity under pressure.

The origin of the activation energy, that is to say, the energy gap of the Mott insulator, has been explained for the half-filled electronic state in § 1.6.4, as given by

$$E_g = U_{\text{eff}} - W, \tag{5.7}$$

where the band width W is considered to be associated with the inter-dimer transfer integral t_{inter}. By means of an approximation, $U_{\text{eff}} \approx 2t_{\text{intra}}$ in the strongly dimerized system (see § 1.1.3),

$$E_g \approx 2t_{\text{intra}} - W. \tag{5.8}$$

This relation gives a general explanation of the pressure dependence of the resistivities for the strongly dimerized system. When the pressure is elevated, the inter-dimer molecular contacts are considered to be more strengthened than the intra-dimer contact, in other words, t_{inter} is a more steeply increasing function of pressure than t_{intra} since the transfer integrals are associated with the overlap integrals between the donor molecules. Therefore, the pressure dependence of the resistivities for strongly dimerized salts is considered to be governed by the decrease of t_{inter} corresponding to the band width, which gives a large effect on the activation energy.

Thus we next treat quantitatively the energy gap on the basis of Eq. (5.8). The band width is here obtained from the band structure based on the tight-binding calculation with an extended Hückel method. The accuracy of the band width obtained from this method is not self-evident, since the calculation within the one-electron approximation leads to a apparent Fermi surface even for the charge transfer salts in the Mott insulating state. However, the band width is considered to be associated with the strength of the inter-dimer interactions, and thus the existence of the Coulomb interaction will not modulate so seriously the band width nevertheless the electronic state can be changed from metal to insulator. Therefore we approximately use the band widths from this calculation. The obtained band widths and the energy gaps based on Eq. (5.8) are summarized in Table 5.3. The value of E_g for β'-(BEDT-TTF)$_2$ICl$_2$ shows remarkably good agreement with the experimental data from

the resistivity ($2E_a$). The values of (BEDT-TTF)$_2$GaCl$_4$ also indicate the same trend of agreement. Thus we insist the justification of the treatment with Eq. (5.8) for the strongly dimerized system where the band is sufficiently split into the upper and lower bands resulting in an effective half-filled electronic state. On the other hand, for the system without a sufficient band splitting, such as α'-(BEDT-TTF)$_2$IBr$_2$ and (EDO-TTFBr$_2$)$_2$AsF$_6$, Eq. (5.8) does not describe the system, showing a discrepancy between the experiments and the calculation (for α'-(BEDT-TTF)$_2$IBr$_2$ the application of Eq. (5.8) is failed because there is no split in the band structure).

Finally, we briefly discuss the problem on ρ_0 ($=\rho_0(P)$). The pressure dependence of ρ_0 for α'-(BEDT-TTF)$_2$IBr$_2$ is obviously revealed in Fig. 3.17, while that of β'-(BEDT-TTF)$_2$ICl$_2$ is almost independent of pressure. In ordinary intrinsic semiconductors, the acoustic-phonon assisted carrier scattering process gives the detailed expression of ρ_0 as described by

$$\rho_0 = \frac{1}{2}\left(\frac{k_{\rm B}T}{2\pi\hbar}\right)^{-\frac{3}{2}} (m_e m_h)^{-\frac{3}{4}} (\mu_e + \mu_h)^{-1}, \tag{5.9}$$

where μ_e, μ_h and m_e, m_h are the mobilities and effective masses of the electrons and holes, respectively. The $T^{-3/2}$-dependence of ρ_0 indicated in Eq. (5.9) is neglected in our analysis, where ρ_0 is obtained from the extrapolation of the room temperature values in the $\ln\rho$ vs $1/T$ plot as $T \to \infty$. Thus the obtained ρ_0 is considered to reflect the value around room temperature consisting of the information of the mobilities and effective masses of the carriers.

In β'-(BEDT-TTF)$_2$ICl$_2$ having strongly dimerization, ρ_0 does not depend on the pressure, while E_a is lowered as the pressure is elevated. Thus, the pressure effect to the electronic state of β'-(BEDT-TTF)$_2$ICl$_2$ gives the decrease of the energy gap while the change of the characteristic properties of the carriers (mobilities and masses) is negligibly small. On the other hand, α'-(BEDT-TTF)$_2$IBr$_2$ indicates the obvious increase of ρ_0 and decrease of E_a as the pressure is elevated. Therefore enormous changes both of the energy gap and the mobilities and/or masses are caused by the pressure in the electronic states of the weakly dimerized systems.

Table 5.1: Activation energies and the prefactor in the temperature dependence of the resistivities at ambient pressure and high pressures for the 2:1 salts.

	P	E_a (eV)	ρ_0 (- cm)
β'-(BEDT-TTF)$_2$ICl$_2$	1 bar	0.10±0.01	4.0×10^{-1}
β'-(BEDT-TTF)$_2$ICl$_2$	7.5 kbar	0.08±0.01	3.8×10^{-1}
β'-(BEDT-TTF)$_2$ICl$_2$	12 kbar	0.07±0.01	4.1×10^{-1}
(BEDT-TTF)$_2$GaCl$_4$	1 bar	0.19±0.01	8.0×10^{-3}
α'-(BEDT-TTF)$_2$IBr$_2$	1 bar	0.20±0.04	1.0×10^{-4}
α'-(BEDT-TTF)$_2$IBr$_2$	8 kbar	0.022±0.03	3.1×10^{-2}
α'-(BEDT-TTF)$_2$IBr$_2$	12 kbar	0.024±0.01	3.0×10^{-2}
(EDO-TTFBr$_2$)$_2$AsF$_6$	1 bar	0.13±0.01	5.0×10^{-4}
(EDO-TTFBr$_2$)$_2$AsF$_6$	9 kbar	0.09±0.01	4.0×10^{-4}

Table 5.2: Fitting parameters of Eq. (5.3) in the pressure dependence of the resistivity for the 2:1 salts.

	ϵ(1/kbar)	ρ_0(300K, 1bar)(- cm)
β'-(BEDT-TTF)$_2$ICl$_2$	0.13	20
(BEDT-TTF)$_2$GaCl$_4$	0.12	10
α'-(BEDT-TTF)$_2$IBr$_2$	0.14	0.3
(EDO-TTFBr$_2$)$_2$AsF$_6$	0.14	0.05

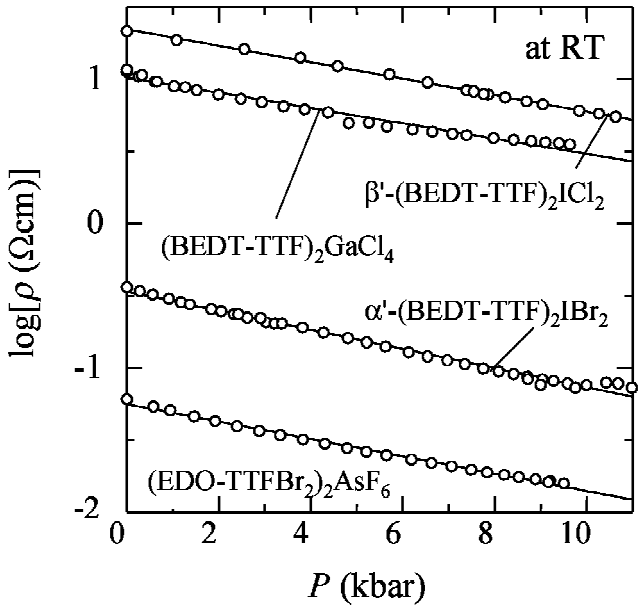

Figure 5.1: Pressure dependence of the resistivity for β'-(BEDT-TTF)$_2$ICl$_2$, (BEDT-TTF)$_2$-GaCl$_4$, α'-(BEDT-TTF)$_2$IBr$_2$, and (EDO-TTFBr$_2$)$_2$AsF$_6$ at room temperature.

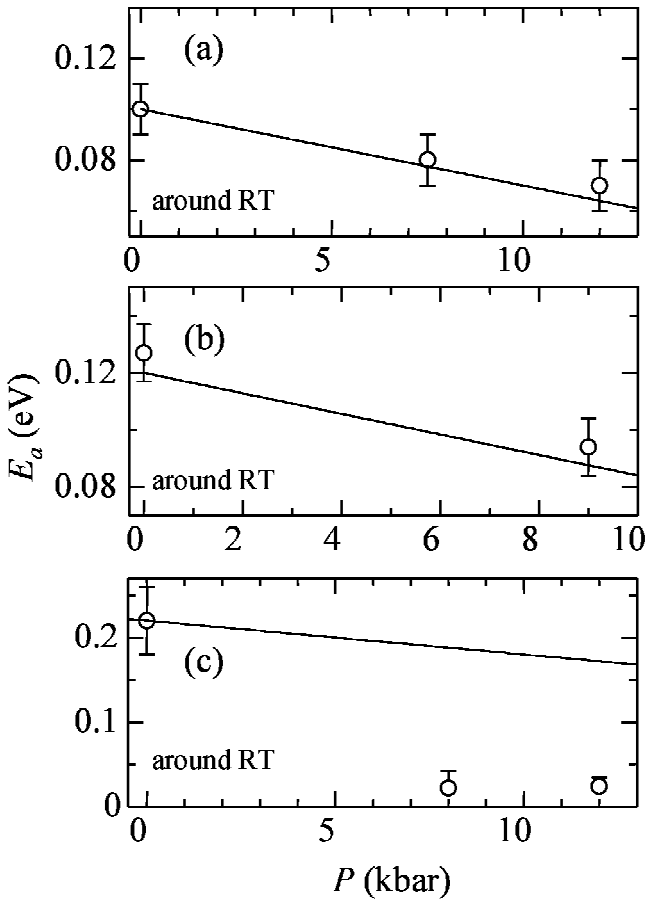

Figure 5.2: Pressure dependence of the activation energy for (a) β'-(BEDT-TTF)$_2$ICl$_2$, (b) (EDO-TTFBr$_2$)$_2$AsF$_6$, and (c) α'-(BEDT-TTF)$_2$IBr$_2$. The plotted data (open circle with error bar) come from the temperature dependence of the resistivities, while the slopes of solid lines, which correspond to Eqs. (5.5) and (5.6), are derived from the pressure dependence of the resistivities without any fitting parameters.

Table 5.3: The values of the energy gap estimated from the temperature dependence of the resistivities ($2E_a$) and the calculation based on Eq. (5.4) (E_g) for the 2:1 salts. The band widths are estimated from the the band structures calculated using the tight-binding approximation. The treatment with Eq. (5.8) cannot be employed for α'-(BEDT-TTF)$_2$IBr$_2$ that has not an effective half-filled state.

	$2E_a$ (eV)	W (eV)	E_g(eV)
β'-(BEDT-TTF)$_2$ICl$_2$	0.20	0.28	0.26
(BEDT-TTF)$_2$GaCl$_4$	0.39	0.30	0.24, 0.18
α'-(BEDT-TTF)$_2$IBr$_2$	0.40	0.60	-
(EDO-TTFBr$_2$)$_2$AsF$_6$	0.26	0.52	0.02

5.1.2 Thermoelectric power

The temperature dependence of the thermoelectric powers is summarized in Fig. 5.3 for the 2:1 salts. The values of the thermoelectric power indicate the similar trend to the resistivity, reflecting the difference in the strength of the dimerization. The thermoelectric powers of strongly dimerized salts have a quite large value at room temperature and monotonically increase as temperature is lowered, while those of weakly dimerized salt, α'-(BEDT-TTF)$_2$IBr$_2$, is much small and decreases changing the sign at 270 K.

The temperature dependence of the positive thermoelectric power for the strongly dimerized salts is almost proportional to the inverse temperature. Therefore, this trend is considered to imply the thermal activation process for the hole-dominant thermoelectric power as mentioned in Eq. (1.54). The Mott insulators, however, are intrinsic semiconductors having the same number of electron- and hole-carriers, and thus the absence of the contribution by the electron-carriers can not be understood easily. Meanwhile, there is a simple model in a strongly correlated systems as noted in § 1.5.1,

$$S = -\frac{k_{\mathrm{B}}}{|e|} \ln \frac{2(1-\varrho)}{\varrho}, \tag{5.10}$$

where ϱ is the number of electrons per site. This electron-hopping-type model in strongly correlated systems is considered to be suitable to apply to our experimental results in the room temperature region, especially for the well localized system such as β'-(BEDT-TTF)$_2$-ICl$_2$, since this model is obtained in the limit of $T \to \infty$ based on a Hubbard model without the contribution of the transfer integrals. We here remind that the expected value of ϱ for the strongly dimerized systems is equal to unity because of the effective half-filled electronic state. However, there is a fatal problem for the application in our systems, since Eq. (5.10) cannot be applied essentially to the half-filled system having the value of ϱ=1 which leads to divergence of the thermoelectric power in Eq. (5.10).

Therefore, taking into account the thermal activation behavior of the thermoelectric power, we modify Eq. (5.10) for the system of a half-filled electronic state in which thermal excitation are allowed. For this modification, we consider the electron configurations in the excited state above a gap of U. If n electrons are excited, there appear n empty sites and n double occupied sites, resulting in $(N_A - 2n)$ singly occupied sites, where N_A is the total number of the sites. In this excited state, the thermoelectric power is obtained by calculating the entropy of the system as given by

$$S = -\frac{k_{\mathrm{B}}}{e} \ln \frac{p}{1-p}, \tag{5.11}$$

where $p = \exp(-U/2k_{\mathrm{B}}T)$.

Equation (5.11) is a function of temperature including the on-site Coulomb interaction U, that is to say, the parameter U governs not only the absolute value but also the temperature-

dependent behavior of the thermoelectric power. The detailed derivation to Eq. (5.11) is discussed in § 5.1.3.

We apply this relation to the experimental data at room temperature. The fitting results for the temperature dependence of the thermoelectric power using only one parameter U is the solid curves shown in Fig. 5.3. In the three salts, the β'-(BEDT-TTF)$_2$ICl$_2$, (BEDT-TTF)$_2$GaCl$_4$, and (EDO-TTFBr$_2$)$_2$AsF$_6$, the fittings with U=0.22, 0.075, and 0.055 eV, respectively, indicate good agreement with the experimental data. The parameters U used for these fittings ($\sim$0.1–0.2 eV), which are considered to correspond with the energy gaps, are in the same order to the energy gaps estimated from the band calculation, or the resistivity measurements (Table 5.3). The calculated result of the thermoelectric power for β'-(BEDT-TTF)$_2$ICl$_2$ is in excellent agreement with the experimental data, and moreover, the obtained value of parameter U=0.22 eV is well consistent with the energy gap obtained from the resistivity and the calculation. It is worth noting that the strength of the dimerization of this salt is considered to be the strongest one among all the salts investigated in this work. There is good agreement also in the temperature dependence of the thermoelectric power for (BEDT-TTF)$_2$GaCl$_4$, whereas there is a deviation of about 0.1 eV between U and E_g. The dimerization of this salt is strong, while it is smaller than that of β'-(BEDT-TTF)$_2$ICl$_2$. (EDO-TTFBr$_2$)$_2$AsF$_6$ is placed in the marginal region to which the present treatment is applicable. Namely, the activation energy of the resistivity is considerably larger than that from the band calculation or the thermoelectric power. In α'-(BEDT-TTF)$_2$IBr$_2$ having weakly dimerization, however, this model fails to explain the experimental result. The thermoelectric power decreases and changes the positive sign to the negative value below 270 K in contrast with the other salts.

Figure 5.3 clearly indicates the deviating behavior of the model from the experimental data as the dimerization is weakened from β'-(BEDT-TTF)$_2$ICl$_2$ to α'-(BEDT-TTF)$_2$IBr$_2$. This model adopts a rough treatment containing only the on-cite Coulomb repulsion without any contribution of the transfer integrals. Therefore the deviating trend upon the reduction in the strength of dimerization is considered to be attributed to the simplicity of this model, nevertheless this model explains the temperature dependence fo the thermoelectric power qualitatively except α'-(BEDT-TTF)$_2$IBr$_2$. The large difference in α'-(BEDT-TTF)$_2$IBr$_2$ is considered to come from the difference of the band fillings, where the band structure is not a half-filled state as discussed in the resistivity under pressure.

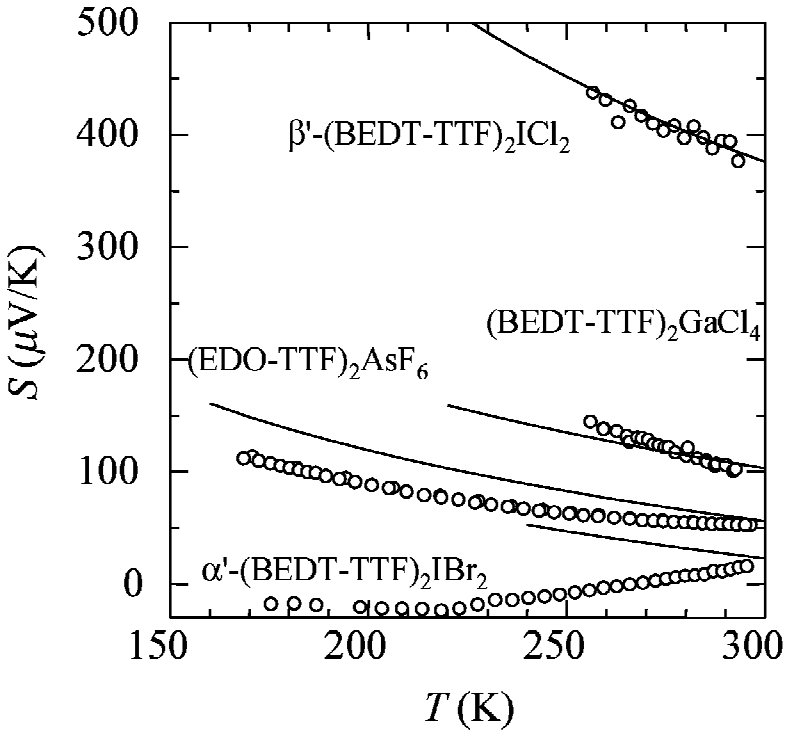

Figure 5.3: Temperature dependence of the thermoelectric power for the 2:1 salts with fitting (solid lines) to Eq. (5.11) where the fitting parameters of the on-site Coulomb energy are given to be 0.224, 0.075, 0.043, and 0.055 eV for β'-(BEDT-TTF)$_2$ICl$_2$, (BEDT-TTF)$_2$GaCl$_4$, α'-(BEDT-TTF)$_2$IBr$_2$, and (EDO-TTFBr$_2$)$_2$AsF$_6$, respectively.

5.1.3 Thermoelectric power of a half-filled electronic state

In this section, we derive the analytical expression of the thermoelectric power in the half-filled highly correlated state shown in Fig. 5.4, where the ground state having the N_A sites is expressed in terms of N localized electrons per site (N=N_A in the ground state).

Here, the system is governed by the thermal excitation based on the Boltzmann statistics. One electron excitation gives an increase of the energy of the state by the on-site Coulomb interaction U. Thus, the Hubbard Hamiltonian is described as

$$\hat{H} = U \sum_i c_{i\uparrow}^\dagger c_{i\uparrow} c_{i\downarrow}^\dagger c_{i\downarrow}, \tag{5.12}$$

where $c_{i\uparrow}^\dagger c_{i\uparrow}$ and $c_{i\downarrow}^\dagger c_{i\downarrow}$ are the number operators in the i-site with the up and down spins, respectively. When n electrons are excited with the excited energy given by nU, three kinds of states of the sites coexist: n sites occupied by an electron, n sites occupied by two electrons, and $(N_A - 2n)$ empty sites without electrons. The degeneracy is described as

$$g = \sum_n e^{-\frac{nU}{k_\mathrm{B}T}} \frac{N_A!}{n!\ n!\ N!} 2^N, \tag{5.13}$$

where the factor 2^N is the degree of the freedom for S=1/2 spins. We apply the maximum term approximation to this system as a canonical ensemble (and thus, N_A=$2n+N$). Now we choose the value of n giving the maximum contribution for g, which makes the free energy of this system to be minimum, giving also the minimum of $\ln g$. Therefore, with applying the Stirling's formula ($\ln x! \approx x \ln x - x$), we obtain the following relation;

$$\frac{2n}{N_A - 2n} \approx \frac{2n}{N_A} = \exp\left(-\frac{U}{2k_\mathrm{B}T}\right) \ (\equiv p), \tag{5.14}$$

where the approximation $2n \ll N_A$ is applied. Next, we treat the n-electron-excited state on the basis of the ground canonical distribution for the number of electrons associating with the single occupied sites, N. Here, the number of the double occupied sites, n, has to be fixed. Therefore, the degeneracy of the state is

$$g = e^{-\frac{nU}{k_\mathrm{B}T}} \frac{N_A!}{(N_A - n - N)!\ n!\ N!}\ 2^N, \tag{5.15}$$

Through the treatment by the Stirling's formula, the derivative of $\ln g$ with respect of N is given as

$$\frac{d \ln g}{dN} = \ln \frac{N_A - n - N}{N} + \ln 2. \tag{5.16}$$

Using Eq. (5.14), the thermoelectric power is obtained as

$$S = -\frac{k_\mathrm{B}}{e} \ln \frac{p}{1-p}. \tag{5.17}$$

This equation indicates that the thermoelectric power for the half-filled state is related only by only the Coulomb interaction U. The plot of the thermoelectric power vs temperature is shown in Fig. 5.5.

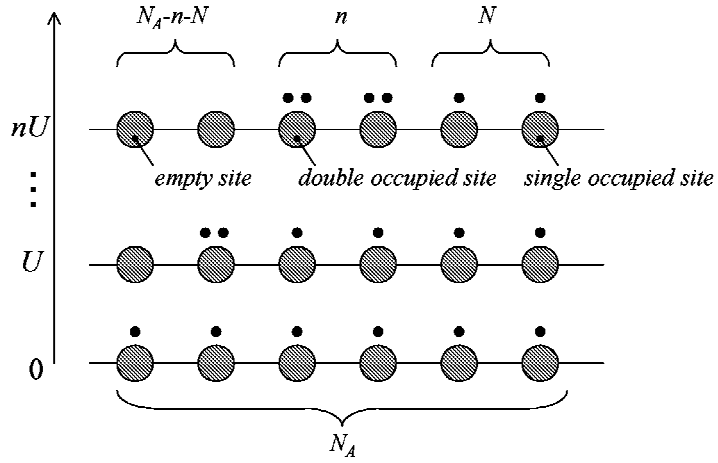

Figure 5.4: The model of a half-filled electronic structure. The ground state has an electron per site. One-electron excitation gives an increase in the energy of the state by the on-site Coulomb interaction U. When n electrons are excited where the excited energy is nU, three kinds of states coexist: sites occupied by an electron, sites occupied by two electrons, and empty sites without electrons.

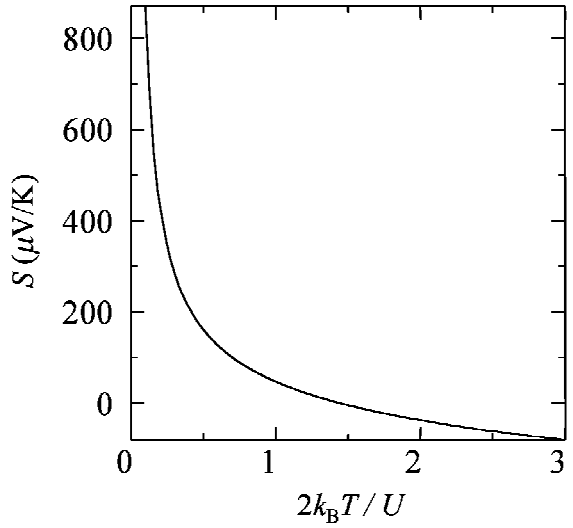

Figure 5.5: Thermoelectric power vs temperature plot based on Eq. (5.17). This figure shows that the large number of excited electrons give a small value of the thermoelectric power.

5.2 Transport properties of the 3:1 salts

The isostructural 3:1 salts, (BMDT-TTF)$_3$ClO$_4$(1,2-dichloroethane) and (BMDT-TTF)$_3$-AsF$_6$(1,1,2-trichloroethane), have phase transitions as shown in the temperature dependence of the resistivity (Figs. 3.30 and 3.39). However, there is a large difference in the phase transitions between two salts, reflected also in the magnetic properties as discussed in § 4.5.

We here point out three characteristic differences in the resistivities between two salts. First, the most remarkable difference in the resistivities is the room temperature values; ∼260 - cm and ∼15 - cm for the ClO$_4$ salt and the AsF$_6$ salt, respectively. The large resistivity of the ClO$_4$ salt is considered to reflect the charge disproportionation ($B^0A^{+1}B^0$), which is expected according to the difference in the donor molecular bond lengths in a trimer consisting of an A and two B molecules.

The second difference between two salts is clearly indicated in the pressure dependence of the resistivities at room temperature as shown in Fig. 5.6. The decreasing trend of the resistivity induced by pressure of the AsF$_6$ salt is much larger than that of the ClO$_4$ salt, and in addition, there is an anomaly around 7 kbar in the AsF$_6$ salt at which the slope of the $\log\rho$ vs P plot is changed, while this kind of anomaly is not seen in the ClO$_4$ salt. The plots describe good linearity similar to the 2:1 salts, which is explained by Eq. (5.3) using the parameters summarized in Table 5.4. It is worth noting that the 3:1 salts have larger pressure-induced decreases of the resistivity than those of the 2:1 salts. This trend indicates that the electronic structure is more easily modified by pressure in the 3:1 salts than in the 2:1 salts.

Third, the pressure dependence of the activation energies around room temperature is characteristic as shown in Fig. 5.7, where the plotted data are obtained from the temperature dependence of the resistivities. The activation energy is almost the same value of ∼0.14 eV at ambient pressure for both salts, while the pressure dependence is different from each other. The values of the activation energies are summarized in Table 5.5 with the values of $\rho_0(P)$. The large pressure dependence of $\rho_0(P)$, as also seen in the weak dimer salt, α'-(BEDT-TTF)$_2$IBr$_2$, is considered to reflect the change of the electronic state. We tried to treat the 3:1 salts in the same way with the 2:1 salts, however the presence of phase transitions makes the analysis meaningless for both salts. The solid lines shown in Fig. 5.7 are obtained on the basis of Eq. (5.4) as expressed by the following relations: $E_a \approx -8\times10^{-3}P + 0.14$ eV for the ClO$_4$ salt, and $E_a \approx -2\times10^{-2}P + 0.14$ eV ($P \leq 7$ kbar) and $E_a \propto -3\times10^{-3}P$ ($P \geq 7$ kbar) for the AsF$_6$ salt, respectively.

We interpret these three differences between two salts as evidence for the charge disproportionation of the ClO$_4$ salt, and thus the electronic states between the two salts are distinctly different from each other. Therefore, we next focus the behavior of the ClO$_4$ salt to consider this point.

The ClO$_4$ salt at ambient pressure shows a gentle decrease of the activation energy around

250 K, from 0.14 eV to 0.09 eV below 250 K. This anomaly is not detected in the magnetic susceptibility and ESR spectra. The transition is clearly observed under 9.6 kbar while the broad transition temperature is almost the same at ambient pressure, where an interesting point is an increase of the activation energy induced by the pressure up to ∼0.20 eV above 250 K. The anomalous pressure-induced increase of the activation energy can be explained on the basis of the charge disproportionation in the ClO_4 salt as follows. When the pressure is increased, the inter-trimer molecular distance becomes decreased more easily than the intra-trimer molecular distance. The decrease of the inter-molecular distance is consider to lead to the increase of $t_{\rm inter}$, and in addition the increase of the inter-trimer Coulomb repulsion since the distance between electrons decreases. Usually, the increase of the transfer integral by the pressure is much larger than the increase of the inter-site Coulomb interaction, since the former increases exponentially with the distance (r) while the latter is proportional to $1/r$. Thus, the application of pressure in most of the electronic systems gives a decrease of the activation energy. However, if there is a charge disproportionation in the trimer system, the electron-carriers are considered to be localized on the center of the trimer, that is, on the A molecule surrounded by neutral B molecules in this case. Therefore the interaction between the carriers will be small. The increase of $t_{\rm inter}$, therefore, does not give influence to the system, and thus the inter-trimer Coulomb interaction governs the activation energy.

On the other hand, the pressure effect is drastic for the AsF_6 salt. One of the characteristic behavior is shown in the pressure dependence of the resistivity at room temperature. The decrease of the resistivity induced by the pressure is quite large, and moreover it indicates a change in the slope of the resistivity vs pressure plot at 7 kbar. Here, to consider the origin of the largely decreasing trend of the resistivity, a comparison between the pressure dependence of the activation energy and of the resistivity is useful. The pressure dependence of the activation energy of the AsF_6 salt around room temperature is shown in Fig. 5.7. The activation energy does not have large decrease below 7 kbar, while it decreases steeply above 7 kbar, and the value at 12 kbar is about 0.007 eV, which is more than one order of magnitude smaller than that at ambient pressure (0.14 eV). That is to say, the steep decrease of the resistivity below 7 kbar is in disagreement with the behavior of the activation energy, and thus it is considered to come from the decrease of the ρ_0. The values of ρ_0 is summarized in Table 5.5. The phase transition near the room temperature region gives a large error to an estimation of ρ_0, nevertheless the decreasing trend of ρ_0 below 7 kbar is detectable (Table 5.5).

The anomalous decrease below 7 kbar is also indicated in the thermoelectric power. The pressure dependence of the thermoelectric power for the AsF_6 salt is shown in Fig. 3.42. The room temperature value of the thermoelectric power decreases down to 60 μV/K as the pressure increases up to ∼7 kbar, and it becomes almost constant above 7 kbar. Therefore, the electronic state of the AsF_6 salt is changed by the induced pressure, which is considered

to modify not only the activation energy but also the mobilities and/or masses of the carriers as described in Eq. (5.9).

Another characteristic point is the small activation energy above 7 kbar. The small activation energy indicates quite a small increasing region of the resistivity at 12 kbar as temperature is lowered above ∼200 K. Afterward, the resistivity steeply increases around 180 K which looks just like a metal-to-insulator transition. This trend implies the comparable transfer integrals with the on-site Coulomb interactions under pressure of 12 kbar. The thermoelectric power at 9.6 kbar supports this result, where the temperature dependence appears, while the steep increase around 200 K is not reflected in the thermoelectric power.

As a result, the transport properties in the 3:1 salts are considered to indicate the large difference of the electronic states between the two salts, regardless that are isostructural to each other. We attribute the reason of the difference to the charge disproportionation in the ClO_4 salt, however, we do not reveal the reason why only the ClO_4 salt has the charge disproportionation. To discuss this point, the detailed crystal structure analyses at low temperatures are indispensable.

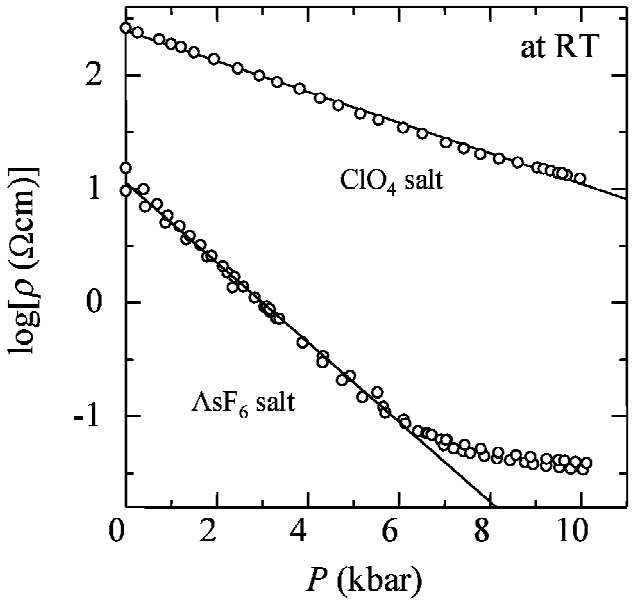

Figure 5.6: Pressure dependence of the resistivity for (BMDT-TTF)$_3$ClO$_4$(1,2-dichloroethane) and (BMDT-TTF)$_3$AsF$_6$(1,1,2-trichloroethane) at room temperature.

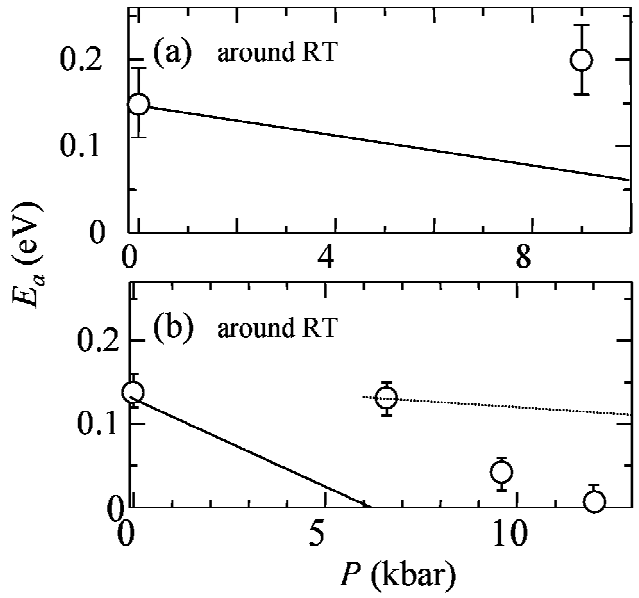

Figure 5.7: Pressure dependence of the activation energy around room temperature for (a) (BMDT-TTF)$_3$ClO$_4$(1,2-dichloroethane) and (b) (BMDT-TTF)$_3$AsF$_6$(1,1,2-trichloroethane), where the dotted line for the AsF$_6$ salt above 7 kbar is the fitting for the data at 7 kbar. Solid lines describe in the same way to Fig. 5.2.

Table 5.4: Fitting parameters of Eq. (5.3) for the 3:1 salts.

	ϵ(1/kbar)	ρ_0(300K, 1bar)(- cm)
MT$_3$ClO$_4$DCE	0.32	260
MT$_3$AsF$_6$TCE ($P < 7$ kbar)	0.83	12
MT$_3$AsF$_6$TCE ($P > 7$ kbar)	0.13	0.1

Table 5.5: Activation energies and the prefactor for the resistivities of the 3:1 salts.

	P	E_a (eV)	ρ_0 (- cm)
MT$_3$ClO$_4$DCE	1 bar	0.14±0.04	8.7×10^{-1}
MT$_3$ClO$_4$DCE	9.6 kbar	0.20±0.04	5.0×10^{-3}
MT$_3$AsF$_6$TCE	1 bar	0.14±0.02	8.0×10^{-2}
MT$_3$AsF$_6$TCE	6.6 kbar	0.13±0.02	1.0×10^{-4}
MT$_3$AsF$_6$TCE	9.6 kbar	0.04±0.02	1.0×10^{-2}
MT$_3$AsF$_6$TCE	12 kbar	0.007±0.004	2.5×10^{-2}

5.3 Classification of charge transfer salts in Mott insulator regime

Before concluding this work, we discuss the common relationship between the physical properties and the electronic states of the investigated charge transfer salts in the Mott insulator regime.

The structural feature of the CT salts investigated is the dimerization/trimerization of the donor molecules. We here discuss the 2:1 salts. As explained in § 1.6.4, a strong dimerization in the 2:1 salts leads to an effective half-filled electronic state, where one electron exists per dimer. The schematic view of this state in a tight-binding limit is shown in Figs. 5.8(a). This situation gives a Mott insulating state featured with the on-cite Coulomb interaction, and thus the electron conduction happens via the state excited by an energy gap $\sim U_{\rm eff}$. β'-(BEDT-TTF)$_2$X (X=ICl_2, $AuCl_2$) and (BEDT-TTF)$_2GaCl_4$ are considered to be well described in this view.

On the other hand, the band structure of the weakly dimerized system gives a 3/4-filled state, where we need to consider three electrons per two molecular sites. This electron-rich state can be treated as the 1/4-filled state of hole-carriers for a convenient treatment, considering the on-site Coulomb interaction between hole-carriers. Here, the condition of the weak dimerization is re-expressed by a small difference between $t_{\rm inter}$ and $t_{\rm intra}$. If we consider $U_{\rm eff}$ for the weak dimer, the second nearest Coulomb repulsion V must be taken into account since V is expected to be comparable to $U_{\rm eff}$ whereas $U_{\rm eff} > V$. Afterward, the ground state is given by an alternating arrangement of the empty site and the site occupied by one-hole carrier as depicted in the lowest energy level of Fig. 5.8(b). The energy states excited by $U_{\rm eff}$ and V from the ground state will be considered, where the state excited by $U_{\rm eff}$ is indispensable for the transport of electrons, since the state excited by V does not flow electrons. Therefore, the energy gap of the conduction is $U_{\rm eff}$ and the effect of V is not observed directly in the energy gap of the transport properties, whereas the coexistence of the comparable V to $U_{\rm eff}$ is considered to feature the electronic states in the weak dimer system and deviates the electronic state from the strongly dimerized picture. Thus in α'-(BEDT-TTF)$_2IBr_2$ the small transfer integrals lead to the electron localized state by means of the $U_{\rm eff}$ and V.

(EDO-TTFBr_2)$_2AsF_6$ is considered to be moderately dimerized, which has strong $t_{\rm intra}$ and $t_{\rm inter}$. The band structure is an effective half-filled state having a small band split. It is expected that the large band width gives the small energy gap based on the strongly dimer model (Eq. (5.8)) of about 0.02 eV, while it is in disagreement with the experimental value of 0.13 eV. This suggests the deviation from the strong dimer model, nevertheless the qualitative behavior of the thermoelectric power is explained by the model.

Finally we indicate a useful mapping for the charge transfer salts in the strongly corre-

lated systems. In this work, we have defined the strength of the dimerization/trimerization by the ratio $t_{\mathrm{intra}}/t_{\mathrm{inter}}$ where the employed t_{inter} is the strongest inter-dimer transfer integral. This definition gives a reasonable consideration both for the magnetic properties and the transport properties. However, here is an exception, κ-type salts having strong dimerization ($t_{\mathrm{intra}}/t_{\mathrm{inter}}$=2.3 for the $Cu(SCN)_2$ salt), which is in almost the same strength of dimerization to the β'-salts ($t_{\mathrm{intra}}/t_{\mathrm{inter}}$=2.7), while its physical properties differ from those of the β'-salts such as the large conductivity (see § 1.8.5). We here consider $2t_{\mathrm{intra}}/W$ as a modified definition of the strength of dimerization, where W is the band width obtained from the band calculation based on the tight-binding method. The prefactor of 2 is added for a convenient treatment in the strongly dimerized systems, because of a correspondence to U_{eff}. This definition is a reasonable extension of that with $t_{\mathrm{intra}}/t_{\mathrm{inter}}$, since W is associated with t_{inter}. The $2t_{\mathrm{intra}}$ vs W plot is shown in Fig. 5.9(b). To estimate $2t_{\mathrm{intra}}/W$ from this plot, we only see the slope of the line between the origin and the plotted data, as given by the dashed line for β'-(BEDT-TTF)$_2$ICl$_2$. Therefore, the slope of the line through the origin represents strength of the dimerization. An interesting point is the boundary given by $2t_{\mathrm{intra}}=W$. The slope of the boundary gives the condition $2t_{\mathrm{intra}}/W=1$, that corresponds to the minimal condition of W for the metallic state in the Hubbard sub-band model (Fig. 5.9(b)). κ-(BEDT-TTF)$_2$Cu(SCN)$_2$ is located just below the boundary, whereas the charge transfer salts investigated here are located above the boundary except the weak dimer/trimer salts, such as α'-(BEDT-TTF)$_2$IBr$_2$, where the donor dimerization picture is failed and the contribution of U_{eff} and V gives the localization of the carriers. Therefore, this figure successfully explains all the charge transfer salts in the Mott insulator regime on the basis of the strength of the dimerization/trimerization.

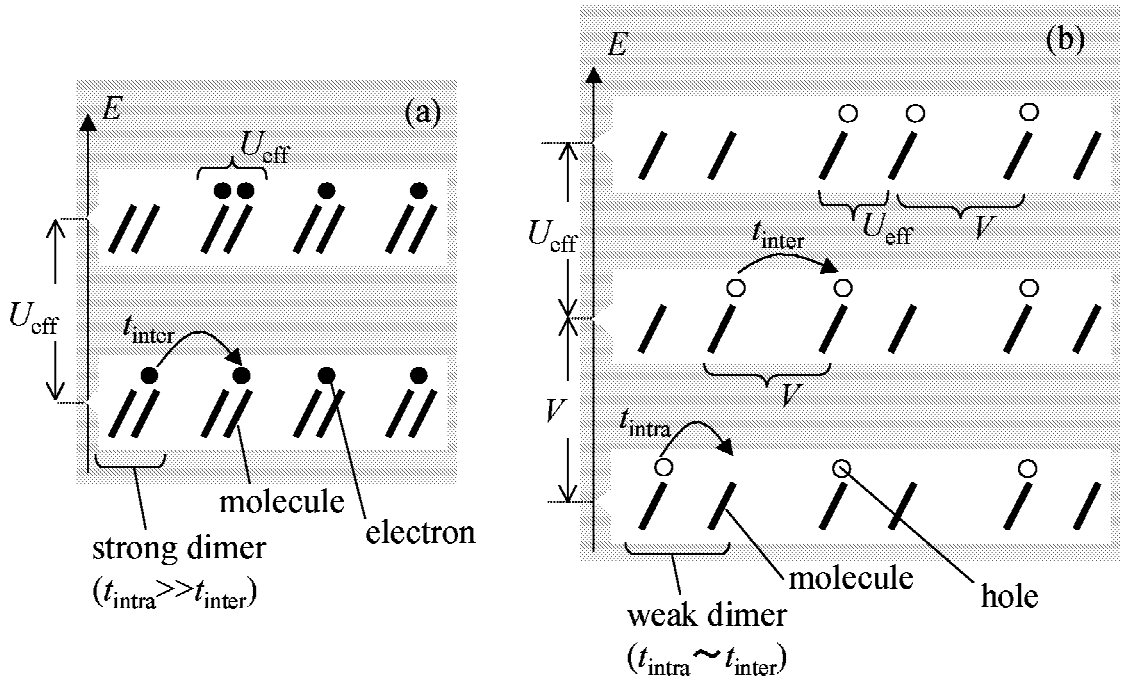

Figure 5.8: Schematic view of electronic state for the 2:1 salts. (a) Strongly dimerized salt with an effective half-filled state. (b) Weakly dimerized salt with a 3/4-filled state. There are two kinds of the excited states with excitation energies of V and U_{eff}, where V is the second nearest Coulomb interaction.

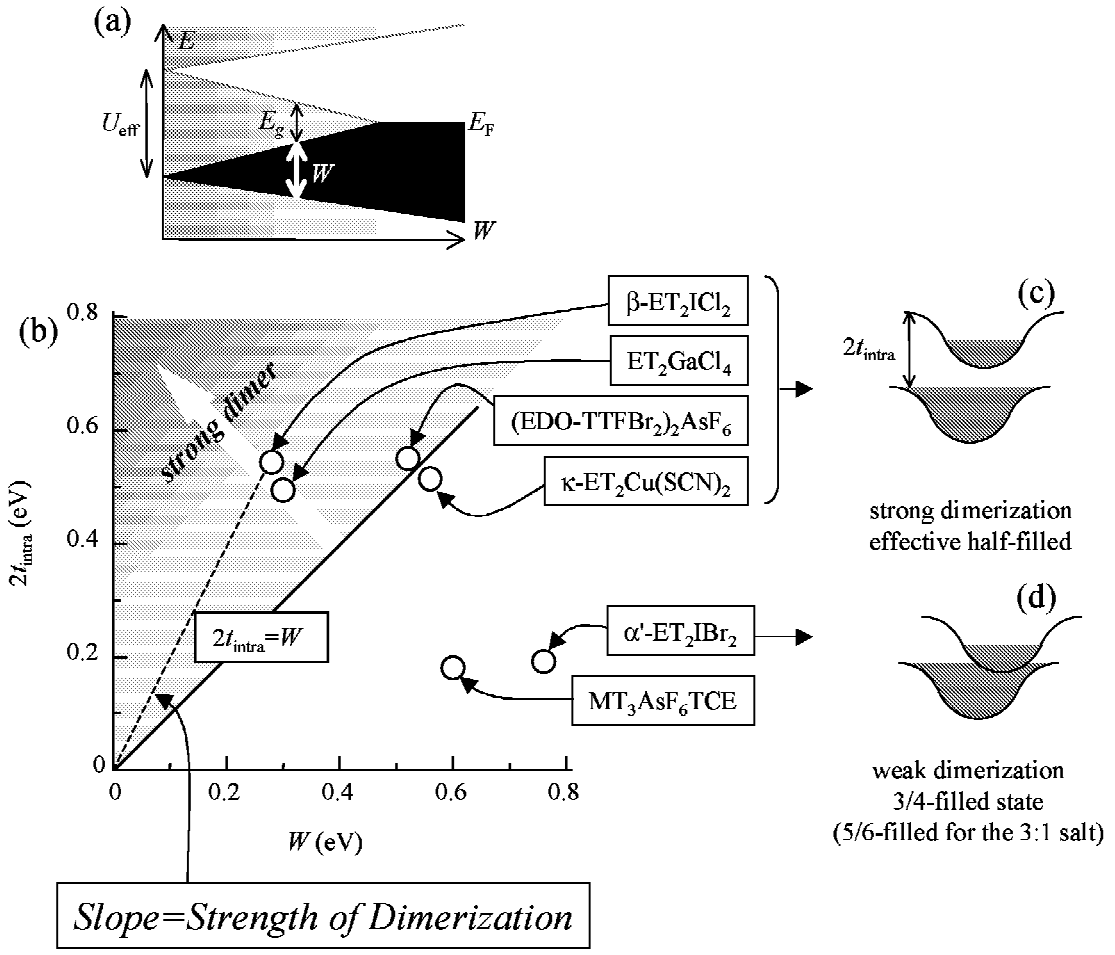

Figure 5.9: Schematic views for the classification of the charge transfer salts in the Mott insulator regime. (a) The Hubbard sub-band (see § 1.6.4). (b) A mapping of the $t_{\rm intra}$ vs the band width. The slope of the lines through the orign corresponds to the strength of the dimerization. We note that the value of the $2t_{\rm intra}$ for (BMDT-TTF)$_3$AsF$_6$(1,1,2-trichloroethane) is substituted by $\sqrt{2}t_{\rm intra}$. (c) and (d) The band structures on the basis of the dimerization.

Chapter 6

Conclusion

We investigated the electrical and magnetic properties of several TTF-based charge transfer salts in strongly correlated systems consisting of dimerized/trimerized-donor units, which are classified into three subgroups; (1) β'-(BEDT-TTF)$_2$X (X=ICl_2, $AuCl_2$), (BEDT-TTF)$_2GaCl_4$, and (EDO-TTFBr$_2$)$_2AsF_6$ as strong-to-intermediate dimer systems, (2) α'-(BEDT-TTF)$_2IBr_2$ as weak dimer systems and (3) (BMDT-TTF)$_3ClO_4$(1,2-dichloroethane) and (BMDT-TTF)$_3AsF_6$(1,1,2-trichloroethane) as weak trimer systems. Group (1) is considered to be the typical Mott insulators, to which the charge transfer salts having clearly dimerized donor structure belong. Groups (2) and (3) are situated in the marginal region of the Mott insulator group, where weak dimerization/trimerization in the crystal structures adds electron delocalization feature to some extent. Groups (1)-(3) cover almost the whole Mott insulator region in Fig. 1.22 except the bounding to the metal region where well-known κ-type BEDT-TTF salts are located.

Eventually, according to this work, except the salts around the metal-insulator boundary, the Mott insulator salts have common features; that is, the magnetic properties can be explained on the basis of the localized spin models regardless of the electron localization/delocalization occurred from the strength of the dimerization/trimerization. On the other hand, The transport properties, both of the resistivity and the thermoelectric power, are largely dependent on the strength of the dimerization/trimerization. The details are summarized as follows.

β'-(BEDT-TTF)$_2$X (X=ICl_2, $AuCl_2$) is magnetically characterized as a quasi two-dimensional square lattice Heisenberg antiferromagnetic system with $J \approx -59$ K for both salts. Three-dimensional antiferromagnetic transitions take place at T_N=22 K and 28 K for the ICl_2 and $AuCl_2$ salts, respectively, in which the small inter-layer interactions $J' \approx 1 \times 10^{-4} J$ and $1 \times 10^{-3} J$ play an important role. The magnetic structure of (BEDT-TTF)$_2GaCl_4$ consists of two kinds of one-dimensional chain structures, where the presence of alternating inter-chain interactions adds a feature of a two-leg-ladder structure. The intra-chain interaction is estimated at $J \approx -70$ K, and the susceptibility decreasing to zero as the temperature approaches

zero is consistent with the feature of the two-leg-ladder system. α'-(BEDT-TTF)$_2$IBr$_2$ having weak dimerization shows the one-dimensional alternating chain structure of $J \approx -53$ and $J' \approx -26$ K, giving a spin-singlet ground state at T=0 K. (EDO-TTFBr$_2$)$_2$AsF$_6$, having intermediate strength of dimerization, is considered to form a quasi one-dimensional Heisenberg antiferromagnet structure with $J \approx -200$ K. The three-dimensional antiferromagnetic transition is observed at 37 K, while the magnetic easy-axis cannot be caught. The crystal structure of (BMDT-TTF)$_3$ClO$_4$(1,2-dichloroethane) forms weak trimerization with charge disproportionation giving one localized spin per trimer, resulting in a quasi one-dimensional structure where the inter-chain interactions generate a frustration feature. The isostructural (BMDT-TTF)$_3$AsF$_6$(1,1,2-trichloroethane) behaves similarly to the (BMDT-TTF)$_3$ClO$_4$(1,2-dichloroethane) from the point of localized spin model in spite of the electron delocalization emerging at high temperatures.

The feature of the ESR line width in relation to the strength of dimerization/trimerization is considered to be responsible for the electron localization. For β'-(BEDT-TTF)$_2$ICl$_2$, (BEDT-TTF)$_2$GaCl$_4$, and (BMDT-TTF)$_3$ClO$_4$(1,2-dichloroethane) having strong electron localization, the ESR line widths can be explained in terms of the spin-spin relaxation similar to the ordinary localized spin systems, whereas the line widths of α'-(BEDT-TTF)$_2$IBr$_2$ and (BMDT-TTF)$_3$AsF$_6$(1,1,2-trichloroethane) are suggestive of strong influence of the spin-lattice relaxation process associated with the electron delocalization. (EDO-TTFBr$_2$)$_2$AsF$_6$ has an exceptional feature of a largely delocalized electrons which is not reflected by the one-dimensionality of the electronic state, and thus the line width is described by the contribution of the spin-spin relaxation, in the same way with the strongly localized electron systems. The most remarkable feature in α'-(BEDT-TTF)$_2$IBr$_2$ and (BMDT-TTF)$_3$AsF$_6$-(1,1,2-trichloroethane) is reflected by the reduced magnetic moments which are considered to feature the delocalization of the electrons on the weak dimer/trimer units.

In the resistivity for the 2:1 salt, the pressure effect clearly indicates the strength of the dimerization. The pressure dependence of the resistivity for the strongly dimerized salts is governed by the decrease of the activation energies, where the change of the features of the carriers, such as mobilities and masses, are considered to be negligible. The activation energies are well explained by the view of strongly dimerized limit, E_g=$2t_{\mathrm{intra}} - W$. On the other hand, in the weakly dimerized salts, α'-(BEDT-TTF)$_2$IBr$_2$, not only the activation energy but the mobilities and/or masses are obviously changed by the pressure. Similar trend is shown also in the 3:1 salts.

For the explanation of thermoelectric power in the 2:1 salts, we considered a model of a strongly correlated electron system with a half-filled electronic state. This simple model well explains the behavior of thermoelectric power for the strongly dimerized salts quantitatively. However, the weak dimerization system having the 3/4-filled band structure is largely different from this model.

The transport properties of the 3:1 salts are governed by the existence of the charge disproportionation of the donor molecules, which leads to the large resistivity and anomalous pressure dependence of the activation energy as indicated in (BMDT-TTF)$_3$ClO$_4$(1,2-dichloroethane). The isostructural salt, (BMDT-TTF)$_3$AsF$_6$(1,1,2-trichloroethane), shows a largely decrease of the resistivity, which is in the similar trend of the weak dimer salt α'-(BEDT-TTF)$_2$IBr$_2$.

Finally, we find out a suitable parameter of $2t_{\mathrm{intra}}/W$ as an indication of the strength of the dimerization/trimerization. This parameter explains the physical properties of the charge transfer salts as strongly correlated systems on the basis of the strength of the dimerization/trimerization.

References

[1] J. B. Torrance, "*Low-Dimensional Conductors and Superconductors*", Edited by D. Jérome and L. G. Caron (NATO ASI Series B: Physics Vol. 155, 1987)

[2] A. Miyazaki, T. Enoki, H. Uekusa, Y. Ohashi, and G. Saito, Phys. Rev., B55, 6847 (1997).

[3] J. C. Bonner and M. E. Fisher, Phys. Rev., 135, A640 (1964).

[4] W. E. Estes, D. P. Gavel, W. E. Hatfield, and D. J. Hadgson, Inorg. Chem., 17, 1415 (1978).

[5] M. E. Lines, J. Phys. Chem. Solids, 31, 101 (1970).

[6] W. Duffy and K. P. Barr, Phys. Rev., 165, 647 (1968).

[7] J. W. Hall, W. E. Marsh, R. R. Weller, and W. E. Hatfield, Inorg. Chem., 20, 1033 (1981).

[8] T. Oguchi, Phys. Rev., 133, A1098 (1964).

[9] F. Keffer, Encyclopedia of physics, ed by H. P. J. Wijn, Springer-Verlag, (1966), Vol. **X VIII**/2, p. 124.

[10] Y. Ajiro, S. Matsukawa, T. Yamada, and T. Haseda, J. Phys. Soc. Jpn., 39, 259 (1975).

[11] P. M. Chaikin, "*Organic Superconductivity*", Edited by V. Z. Kresin and W. A. Little, Plenum Press, New York, 1990.

[12] P. M. Chaikin and G. Beni, Phys. Rev. B, 13, 647 (1976).

[13] J. F. Kwak, G. Beni, and P. M. Chaikin, Phys. Rev. B, 13, 641 (1976).

[14] J. F. Kwak and G. Beni, Phys. Rev. B, 13, 652 (1976).

[15] J. Ferraris, D. O. Cowan, V. J. Walatka, and J. H. Perlstein, J. Am. Chem. Soc., 95 (1973) 948.

[16] S. Kagoshima, H. Nagasawa, T. Sambongi, "*One-Dimensional Conductors*", (Springer, Berlin, Heidelberg 1988) p.52

[17] K. Bechgaard, C. S. Jacobsen, H. J. Pedersen, and N. Thorup, Solid State Commun., 33 (1980) 1119.

[18] H. Urayama, H. Yamochi, G. Saito, K. Nozawa, T. Sugano, M. Kinoshita, S. Sato, K. Oshima, A. Kawamoto, and J. Tanaka, Chem. Lett., 55 (1988).

[19] T. Mori, A. Kobayashi, Y. Sasaki, H. Kobayashi, G. Saito, and H. Inokuchi, Bull. Chem. Soc. Jpn, 57, 627 '1984).

[20] T. Ishiguro, K. Yamaji, G. Saito, "*Organic Super-Conductors*", (Springer, Berlin, Heidelberg 1990) p.51

[21] T. Mori and H. Inokuchi, Solid State Commun., 62, 525 (1987).

[22] S. D. Obertelli, R. H. Friend, D. R. Talham, M. Kurmoo, and P. Day, J. Phys.: Condens. Matt., 1, 5671 (1989).

[23] J. Yamaura, A. Miyazaki, T. Enoki, and G. Saito, Phys. Rev., B55, 3649 (1997).

[24] H. Ito, T. Ishiguro, M. Kubota, and G. Saito, J. Phys. Soc. Jpn., 66, 2987 (1996).

[25] T. Naito, K. Bun, A. Miyamoto, H. Kobayashi, H. Sawa, R. Kato, and A. Kobayashi, Synth. Met., 55-57, 2234 (1993).

[26] S. Klotz, J. S. Schilling, S. Gartner, and D. Schweitzer, Solid State Commun., 67, 981 (1988).

[27] D. R. Talham, M. Kurmoo, P. Day, D. S. Obertelli, I. D. Parker, and R. H. Friend, J. Phys. C: Solid State Phys., 19, L383 (1986).

[28] M. Inoue and M. B. Inoue, J. Chem. Soc., Chem. Commun., 1043 (1985).

[29] M. Kobayashi, T. Enoki, K. Imaeda, H. Inokuchi, and G. Saito, Phys. Rev., B36, 1457 (1987).

[30] A. Miyazaki, I. Ichikawa, T. Enoki, and G. Saito, Bull. Chem. Soc. Jpn., 70, 2647 (1997).

[31] K. Mortensen, Y. Tomkiewicz, and K. Bechgaard, Phys. Rev., B25, 3319 (1982).

[32] P. J. Nigrey, B. Morosin, J. F. Kwak, E. L. Venturini, and R. J. Baughman, Synth. Met., 16, 1 (1986).

[33] H. Kobayashi, R. Kato, A. Kobayashi, G. Saito, M. Tokumoto, H. Anzai, and T. Ishiguro, Chem. Lett., 89 (1986).

[34] T. J. Emge, H. H. Wang, P. C. W. Leung, P. R. Rust, J. D. Cook, P. L. Jackson, K. D. Carlson, J. M. Williams, M.-H. Whangbo, E. L. Venturini, J. E. Schirber, L. J. Azevedo, and J. R. Ferraro, J. Am. Chem. Soc., 108, 695 (1986).

[35] T. J. Emge, H. H. Wang, M. K. Bowman, C. M. Pipan, K. D. Carlson, M. A. Beno, L. N. Hall, B. A. Anderson, J. M. Williams, and M. -H. Whangbo, J. Am. Chem. Soc., 109, 2016 (1987).

[36] M. Tokumoto, H. Anzai, T. Ishiguro, G. Saito, H. Kobayashi, R. Kato, and A. Kobayashi, Synth. Met., 19, 215 (1987).

[37] N. Kinoshita, M. Tokumoto, H. Anzai, and G. Saito, Synth. Met., 19, 203 (1987).

[38] C. Coulon, R. Laversanne, J. Amiell, and P. Delhaes, J. Phys. C: Solid State Phys., 19, L753 (1986).

[39] M. Kurmoo, M. Allan, R. H. Friend, D. Chasseau, G. Bravic, and P. Day, Synth. Met., 41-43, 2127 (1991).

[40] Y. Nogami, S. Kagoshima, T. Sugano, and G. Saito, Synth. Met., 16, 367 (1986).

[41] M. Watanabe, M. Nishikawa, Y. Nogami, K. Oshima, and G. Saito, J. Korean Phys. Soc., 31, 95 (1997).

[42] R. Kato, H. Kobayashi, A. Kobayashi, and Y. Sasaki, Chem. Lett., 1693 (1984).

[43] R. Kato, H. Kobayashi, T. Mori, A. Kobayashi, and Y. Sasaki, Solid State Commun., 55, 387 (1985).

[44] H. Urayama, H. Yamochi, G. Saito, S. Sato, T. Sugano, M. Kinoshita, A. Kawamoto, J. Tanaka, T. Inabe, T. Mori, Y. Maruyama, and H. Inokuchi, Synth. Met., 27, A393 (1988).

[45] H. H. Wang, L. K. Montgomry, A. M. Kini, K. D. Carlson, M. A. Beno, U. Geiser, C. S. Cariss, J. M. Williams, and E. L. Venturini, Physica C 156, 173 (1988).

[46] K. Oshima, T. Mori, H. Inokuchi, H. Urayama, H. Yamochi, and G. Saito, Phys. Rev., B38, 938 (1988).

[47] S. Kagoshima, H. Nagasawa, T. Sambongi, "*One-Dimensional Conductors*", (Springer, Berlin, Heidelberg 1988) p.49

[48] P. Braunstein and R. J. H. Clark, J. Chem. Soc., Dalton, 1845 (1973).

[49] J. M. Williams, H. H. Wang, M. A. Beno, T. J. Emge, L. M. Sowa, P. T. Copps, F. Behroozi, L. N. Hall, K. D. Carlson, and G. W. Crabtree, Inorg. Chem., 23, 3841 (1984).

[50] H. C. Montgomery, J. Appl. Phys.,42, 2971 (1971).

[51] R. P. Shibaeva, R. M. Lobkovskaya, M. A. Simonov, E. B. Yagubskii, and A. A. Ignat'ev, Kristallografiya, 31, 1105 (1986).

[52] T. Enoki, J. Yamaura, and A. Miyazaki, Bull. Chem. Soc. Jpn., 70, 2005 (1997).

[53] N. Yoneyama, A. Miyazaki, and T. Enoki, Synth. Met., to be published.

[54] H. Seo and H. Fukuyama, J. Phys. Soc. Jpn., 66, 3352 (1997).

[55] T. Sugano, G. Saito, and M. Kinoshita, Phys. Rev., B34, 117 (1986).

[56] T. Sugano, G. Saito, and M. Kinoshita, Phys. Rev., B35, 6554 (1987).